Master of Science Thesis

Buffet envelope prediction of transport aircraft during the conceptual design phase

Predict transonic, shock induced buffet onset

J.N.A. van Eijndhoven BSc.

January 30, 2012

Faculty of Aerospace Engineering · Delft University of Technology

Faculty of Aerospace Engineering

Delft University of Technology

Buffet envelope prediction of transport aircraft during the conceptual design phase
Predict transonic, shock induced buffet onset

Master of Science Thesis

For obtaining the degree of Master of Science in Aerospace Engineering at Delft University of Technology

J.N.A. van Eijndhoven BSc.

January 30, 2012

Faculty of Aerospace Engineering · Delft University of Technology

Delft University of Technology

Delft University Of Technology
Department Of
Design, Integration and Operations of Aircraft and Rotorcraft

The undersigned hereby certify that they have read and recommend to the Faculty of Aerospace Engineering for acceptance a thesis entitled **"Buffet envelope prediction of transport aircraft during the conceptual design phase"** by **J.N.A. van Eijndhoven BSc.** in partial fulfillment of the requirements for the degree of **Master of Science**.

Dated: January 30, 2012

Head of department: ______________________
Prof.dr.ir.drs. H. Bijl

Supervisor: ______________________
Dr.ir. R. Vos

Reader: ______________________
A. Elham MSc.

Summary

The conceptual design phase still has a very large spectrum of different design solutions open, and therefore the need for convergence in the design process is high. There is a need for relatively simple design tools which should indicate the influence of a (small) change in design parameters on the resulting design and performance. Although for time constraints these methods need to be relatively simple and low on computational time, they are not allowed to have too large of an error bandwidth in order to be accurate enough to justify design decisions.

During conceptual design a problem arises when predicting the buffet onset boundary. Due to the pressure on payload-range and cruise altitude capability, improvement on the buffet onset boundary is often of great importance. It is one of the primary constraints in establishing the low and transonic speed performance capabilities of transport aircraft. Buffeting, a high-frequency instability caused by airflow separation or shock wave oscillation, can be seen as a random forced vibration. Depending on the angle of attack and freestream velocity, the separations in the flow can result in an aerodynamic excitation. The separated boundary layer at the trailing edge can create a wake of turbulent flow, and if this wake hits for example the horizontal tail surface, buffet can affect the tail unit of the aircraft structure. Since buffet can limit the design lift coefficient, it may limit the maximum lift-to-drag ratio and operational ceiling of the airplane. This implies the performance calculations made by the designer can be inaccurate with respect to the actual performance of the aircraft if buffet is not accurately accounted for, since both the Breguet range equation and endurance equation are a function of this lift and drag characteristic. In short, the main motivation for this thesis research is to create a more advanced but fast transonic buffet onset prediction tool to permit greater design freedom during the conceptual design phase. This implies the tool should be faster than conventional tools, it should be reliable and able to deal with unconventional configurations. In addition, it should be built in a modular way so it is easy to use, alter and replace parts of the tool.

In this thesis the traditional methods for predicting buffet are discussed, as well as the need for new prediction methods. It also provides an overview of the physical causes of buffet and the aerodynamics involved. A number of new buffet prediction methods are discussed, and a trade-off is presented in order to develop a new approach to transonic buffet prediction, which is further investigated in this thesis. The new tool developed combines a vortex lattice program to determine the highest loaded wing section in spanwise direction (at which buffet is expected to originate), with two different 2-dimensional flow solvers to determine local Mach number and pressure distribution over the resulting highest loaded section airfoil. The two different 2-dimensional codes used are a transonic small disturbance code TSFOIL and a 2-dimensional Euler code MSES. Together with two different separation criteria from literature, dependent on the limiting local Mach number and critical pressure rise for separation, this produces four different combinations to compute the buffet onset boundary. To reduce computation time, not all $M_\infty - \alpha$ combinations possible are investigated during the 2-dimensional flow approximation, but a bisection method is used to find buffet onset combinations of $M_\infty - \alpha$.

Translating the resulting 2-dimensional buffet onset boundary in terms of $M_\infty - \alpha$ for the airfoil under investigation to the 3-dimensional $M_\infty - \alpha$ values for the wing is done using simple geometric relations for the Mach number of the local and freestream flow, as well as for the angle of attack of the airfoil and the wing-fuselage. The final step in the buffet prediction tool, the translation of the 3-dimensional $M_\infty - \alpha$ buffet onset results to $M_\infty - C_L$ results is done either using AVL or Matrix-V. Both AVL and Matrix-V are used to investigate the difference of wing lift coefficient prediction using a simple vortex lattice code with respect to a more complex and time consuming 3-dimensional code.

The buffet prediction tool was demonstrated using the Fokker 100 wing-fuselage combination test case. The two different 2-dimensional simulation programs and two separation criteria available were combined to be able to decide the best way of predicting transonic buffet onset with respect to number of buffet points, accuracy, bandwidth, and computational time. It can be concluded a modular transonic buffet onset prediction tool is successfully developed with help of a Vortex-Lattice method, 2-dimensional Euler code and Matrix-V code. It is approximately 90% faster with respect to the use of only a Matrix-V code and it is reliable in the region left of the coffin corner at high C_L low M_∞ combinations. The expected error in the regime which can be correctly predicted by this tool is in the order of $\Delta C_L = 0.05$ which is in the same order as the error bandwidth presented in a semi-empirical method of Isikveren [1]. Whether it is also reliable in the high transonic regime, has to be investigated during further research. This is because the results presented in this thesis have a number of outliers at high M_∞ low C_L combinations. Apparently the incorrect results start exactly when the 2-dimensional airfoil is set under a negative angle of attack. The main cause of this problem is most probably the fact the linear relation between the freestream Mach number and angle of attack which describes a straight bisection line, as can be seen in Chapter 3, $\alpha = C_1 \cdot M_\infty + C_2$, has a positive slope C_1. When at negative angles of attack separation is detected, the Mach number decreases due to the lower interval chosen by the bisection method, which automatically makes α even more negative. This is undesirable, since in that case α should increase ($\alpha \to 0$). Or even better, $\alpha \to \alpha_0$.

It can be concluded buffet is likely to originate at the wing section at which the local lift coefficient is maximal, neglecting the effect of aft loading. Aft loading causes an in-

crease in lift, but no increase on the magnitude of the suction peak over the upper surface of the airfoil, so the ΔC_P remains the same. This way, the highest loaded section does not necessarily have to be the section with the highest suction peak. The wing sweep is of significant influence on the buffet onset boundary, as is the wing twist and incidence angle. The wing dihedral is neglected because the cosine of the wing dihedral angle is ≈ 1 for small dihedral angles. Modeling the fuselage in addition to the wing to account for the wing-fuselage interaction (flow being pushed outboard) during the first AVL run did not prove to be of any influence. This effect is not visible in the local lift coefficient distribution using AVL. The spanwise position of the highest loaded section remained unchanged for a run with, and without fuselage.

The separation criterion to be used is the critical pressure rise separation criterion, which produces better result compared to the limiting local Mach number separation criterion. It is recommended to specify 20 points on the buffet onset curve, and use the 2-dimensional Euler code MSES as 2-dimensional solver. By using 20 data points on the buffet onset curve, it will be possible during post-processing to determine the outliers in the dataset and still end up with enough points to plot a decent buffet onset boundary using a polynomial or least squares solution to be fitted in the remaining set of data points. One of the criteria which could be used is Chauvenet's criterion. It is advisable to use the intermediate results of the buffet onset prediction method developed, being the $M_\infty - \alpha$ buffet onset data, and discard the last AVL step at which the wing lift coefficient is determined. Instead, one should use Matrix-V to predict the wing lift coefficients. This ensures a more accurate estimation of the wing lift coefficient, at the cost of about an hour more computation time in the 20 data point case. Using Matrix-V instead of AVL, the reduction in computational time between the developed tool with respect to the use of only a 3-dimensional code such as Matrix-V is still expected to be about 90%. When for example Matrix-V would be used to compute the entire buffet onset boundary, at 5 minutes per data point, 20 points (each using 10 bisection iterations) this would result in a computation time of $5 \cdot 10 \cdot 20 = 1000$ minutes, being 60000 seconds. A 20 point MSES run, including a final Matrix-V run to improve the accuracy of the wing lift coefficient calculation, would take $1750 + 3300 = 5050$ seconds.

The difference in terms of wing lift coefficient calculation between AVL and Matrix-V is plotted on the data from the Fokker report [2] and with respect to the MSES run with critical pressure rise separation criterion in figure 1. It shows the Matrix-V result shift the computed buffet onset boundary downwards towards the literature line. It is clearly visible AVL over predicts the wing lift coefficient. To quantify the error made in the wing lift coefficient determination, the ΔC_L is determined between the (interpolated) literature data and the Matrix-V run as shown in figure 1. The Matrix-V run over, and under predicts the wing lift coefficient in the region $0.65 < M_\infty < 0.75$ with an intersection at approximately $M_\infty = 0.72$. The error bandwidth is shown in table 1. If a conclusion is drawn on the buffet onset lift coefficient C_L at the cruise Mach number of the Fokker 100 demonstration case only, one could conclude at $M_{cruise} = 0.75$ the buffet onset lift coefficient will be around $C_L = 0.68$, which will result, in an operational point of view, in a $C_L = \frac{0.68}{1.3} = 0.52$ with an error of $\Delta = C_{L_{Lit}} - C_{L_{MatV}} = 0.68 - 0.71 = 0.03$. If compared to the empirical method by Isikveren [1], which concludes a margin of error of $\Delta \approx 0.026$ is possible, this is of the same order of magnitude. The advantage of using a numerical method is the use of reference data (or seed aircraft) is not needed, and random (unconventional) wing geometries can be investigated as well.

With respect to further use of this tool, it is essential to solve in incapability of the program with respect to negative angles of attack. Furthermore, it is most interesting to see how this transonic buffet prediction tool behaves when less conventional wing geometries are tested. For example a flying wing, blended wing body, or Prandtl plane. Possibly the first AVL step has to be altered a little to cope with these geometries, but when the highest loaded section is determined, the program could run as normal. The results then could be an indicator of the transonic buffet characteristics of these unconventional, conceptual wing formations. Furthermore one has to see the computational times associated with this tool in the right perspective. A run time in the order of multiple minutes or even an hour might seem like a long time to compute a buffet onset boundary, but if the total time used by a multi model generator or other design environment is in the order of days, weeks or even months, this might not be an issue. In addition, the buffet onset prediction module could be ran parallel with other tools to make it more efficient.

Table 1: ΔC_L for literature and Matrix-V results, Fokker 100 wing, $\Lambda_{0.5c}$ at $Re \approx 1.5 \cdot 10^7$

M_∞	$C_{L_{Lit}}[-]$	$C_{L_{MatV}}[-]$	$\Delta C_L[-]$
0.75	0.68	0.71	-0.03
0.73	0.72	0.81	-0.09
0.70	0.87	0.85	0.02
0.68	0.86	0.84	0.02
0.65	0.86	0.83	0.03

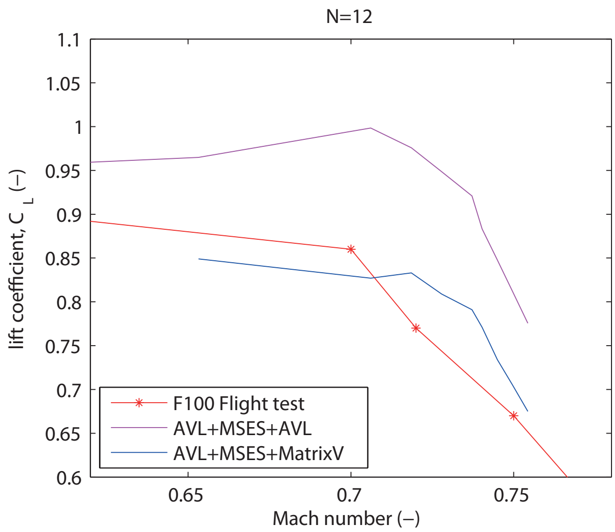

Figure 1: Buffet onset of Fokker 100 wing-fuselage combination, F100 flight test versus MSES and AVL or Matrix-V, 12 buffet points, ΔC_P separation criterion

Acknowledgements

I wish to thank dr.ir. Roelof Vos for his professional, motivating and to the point supervising of my thesis research. It was of great help in finding the right approach to work on predicting this complex aerodynamic phenomenon. He also managed to put this thesis work in the right perspective with respect to the multi model generating environment this tool will eventually become part of, and pointed out the need for a modular approach in developing this tool. I want to thank Ali Elham MSc. for the support with the MSES program and Matrix-V simulations, ing. Michiel Haanschoten for the help in re-programming part of the Linux MSES code in Fortran to help solving some of the drawbacks of MSES under windows.

Further thanks goes to Bert Franssen BSc. for the help with input and output handling of AVL geometries and results in Matlab, dr.ir. Mark Voskuijl and Ir. Evert Jesse for information on the wing geometry and twist distribution of the Fokker 100 wing. Last but not least, I want to thank Anne-Linde van Gameren for her help in the graphical design of the figures in this thesis.

Delft, The Netherlands J.N.A. van Eijndhoven BSc.
January 30, 2012

Contents

List of Figures

List of Tables

Nomenclature

Latin Symbols

a	Speed of sound	$\frac{\mathrm{m}}{\mathrm{s}^2}$
AR	aspect ratio	$-$
b	wing span	m
C	Sutherland's constant	K
c	Chord length	m
C_1	slope of bisection method line	$\frac{\mathrm{deg}}{\mathrm{M}}$
C_2	start angle of attack of bisection method	deg
C_μ	dissipation weight factor scaling coefficient	$-$
C_D	aircraft drag coefficient	$-$
C_f	skin friction coefficient	$-$
C_L	aircraft lift coefficient	$-$
c_L	local lift coefficient	$-$
C_p	pressure coefficient	$-$
c_p	isobaric speciffic heat coecient	$\frac{\mathrm{J}}{\mathrm{KgK}}$
c_v	specic heat at constant volume	$\frac{\mathrm{J}}{\mathrm{KgK}}$
D	drag	$-$
D	substantial derivative operator	$-$
d_f	fuselage diameter	m
e	internal energy	$\frac{\mathrm{J}}{\mathrm{Kg}}$
f	body force per unit mass	$\frac{\mathrm{N}}{\mathrm{Kg}}$
f	frequency	Hz

g	gravitational acceleration vector	$\frac{\mathrm{m}}{\mathrm{s}^2}$
H	boundary layer shape factor	–
H	total enthalpy per unit mass	$\frac{\mathrm{J}}{\mathrm{Kg}}$
h	enthalpy per unit mass	$\frac{\mathrm{J}}{\mathrm{Kg}}$
i, j	indices	–
k	heat transfer coefficient	$\frac{\mathrm{J}}{\mathrm{msK}}$
L	lift	N
l	characteristic length	m
M	mach number	–
N	Number of buffet points	–
n	number of itterations	–
p	pressure	$\frac{\mathrm{N}}{\mathrm{m}^2}$
Q	heat per unit volume	$\frac{\mathrm{J}}{\mathrm{m}^3}$
q	heat transfer per unit area	$\frac{\mathrm{J}}{\mathrm{sm}^2}$
R	Range	m
R	gas constant	$\frac{\mathrm{J}}{\mathrm{KgK}}$
Re	Reynolds number	–
S	Wing planform area	m^2
s	entrophy	$\frac{\mathrm{J}}{\mathrm{KgK}}$
T	temperature	K
t	time	sec
U	velocity distribution	$\frac{\mathrm{m}}{\mathrm{s}}$
u, v, w	cartesian velocity components	$\frac{\mathrm{m}}{\mathrm{s}}$
V	velocity vector	$\frac{\mathrm{m}}{\mathrm{s}}$
W	weight	N
x, y, z	cartesian coordinates	m
y^+	wall coordinates	m

Greek Symbols

α	angle of attack	deg
β	constant in Sutherland's formula	–
Δ	gradient	–
δ^*	boundary layer displacement thickness	m
η	wing section airfoil	–
γ	ratio of specific heats	–
κ	von Karman constant	–

Λ	Wing sweep angle	deg
λ	taper ratio	$-$
μ	dynamic viscosity	$\frac{\mathrm{kg}}{\mathrm{sm}}$
ν	kinematic viscosity	$\frac{\mathrm{m}^2}{\mathrm{s}}$
Φ	viscous dissipation function	$-$
ρ	density	$\frac{\mathrm{kg}}{\mathrm{m}^3}$
τ	shear stress	$\frac{\mathrm{N}}{\mathrm{m}^2}$
θ	boundary layer momentum thickness	m
ζ	fluid vorticity	$\frac{\mathrm{m}}{\mathrm{s}}$

Subscripts

$0.25c$	quarter chord
$0.5c$	half chord
0	wall or reference point (sea level)
airfoil	2-dimensional case
AVL	AVL run
crit	critical
cruise	cruise condition
lam	laminar
Lit	literature values
local	local
MatV	Matrix-V run
max	maximal
min	minimal
number	number of buffet points
qchd	quater chord
ref	reference value
root	root chord
tip	tip chord
turb	turbulent
visc	viscous
wf	wing-fuselage 3-dimensional case
e	parallel to the flow vector
n	natural
s	shock
s	streamwise direction

$_t$	friction
$_w$	wall

Superscripts

*	limiting

Abbreviations

ADSE	Aircraft development and systems engineering company
AVL	Athena Vortex Lattice
CFD	Computational Fluid Dynamics
DNS	Direct Numerical Simulation
LHS	Left Hand Side
MSES	Multi-element airfoil design and analysis software
NACA	National Advisory Committee for Aeronautics
PDE	Partial Differential Equation
RANS	Reynolds Averaged Navier Stokes
RHS	Right Hand Side
RMS	Root Mean Square
TSFOIL	Transonic Small disturbance program
TS	Transonic

Chapter 1

Introduction

1.1 Motivation

The conceptual design phase is one of the most dynamic parts of the design process of an aircraft. It includes setting up the requirements for the design, preliminary specifications, lifting and control surfaces sizing, performing a weight and balance estimation, stability checks, selecting and designing the different airfoils to be used and designing the planform geometry. It is the phase of the design which still has a very large spectrum of different design solutions open, and the need for convergence is high.

Characteristic for the conceptual design phase is the need for relatively simple prediction tools. The tools and prediction methods used in this design phase should indicate the influence of a (small) change in design parameters on the resulting design and performance. One could say this sensitivity of the primary design parameters is of great importance to the designers. Important to keep in mind is that although these methods need to be relatively simple and low on computational time, they are not allowed to have too large of an error bandwidth in order to be accurate enough to justify design decisions.

When analysing the performance of a certain aircraft wing geometry in the conceptual design phase, a problem arises when trying to predict the buffet onset boundary at low subsonic speeds near the stall speed, and in the transonic regime past the critical Mach number. The way traditional conceptual design methods predict this separation phenomenon and resulting vibration of the airframe is by fitting the known buffet onset boundary of an actual aircraft that closely matches the parameters of the conceptual design at hand. One could call this an empirical method of predicting the transonic buffet characteristics of a designed wing geometry with the help of a database with known buffet boundaries [1]. Apart from the inability to perform sensitivity studies, a second problem with this approach is finding a good match between previously designed aircraft and the new design, that matches the complete design flight envelope. In other words, no unconventional designs can be assessed using this prediction method, and no sensitivity of some key design parameters can be investigated. The need for a correct and precise buffet prediction becomes clear looking at the lift-to-drag ratio for certain wing and aircraft designs. The lift-to-drag ratio, or $\frac{L}{D}$, is the amount of lift generated divided by the drag associated with the design. A higher or more favourable lift-to-drag ratio is typically one of the major goals in aircraft design, as delivering a certain lift with lower associated drag leads directly to better fuel economy and climb performance. Since buffet can limit the lift coefficient at which a certain wing or aircraft can fly, it may limit the maximum lift-to-drag ratio, which means the performance calculations made by the designer can be inaccurate with respect to the actual performance of the aircraft. Therefore, the design lift coefficient will always be influenced by the buffet onset lift coefficient at the design Mach number. The certification regulations require the lift coefficient in operational cruise conditions to be limited such that a load factor of $n = 1.3$ can be reached without encountering buffet [14, 5]. In short, the main motivation for this thesis research is to create a more advanced but fast buffet envelope prediction tool to permit greater design freedom during the conceptual design phase.

1.2 Research Goal

The main goal of this thesis research is to create a transonic buffet prediction tool, to predict the buffet onset diagram of transport aircraft, to be used during the conceptual design phase. This implies the tool should be faster than conventional tools, it should be reliable and able to deal with unconventional configurations. In addition, it should be built in a modular way so it is easy to use, alter and replace parts of the tool.

To develop such a tool and achieve this research goal, first it has to be established what buffet actually is and what the physical causes are. Where on the wing does it originate? Which geometric and aerodynamic parameters are important? Are there different types of shock waves, boundary layer effects, and the interaction between these two to be accounted for? Which aircraft wing geometry parameters like for example wing sweep angle, wing aspect ratio, wing span, wing planform area en thickness-to-chord ratio, play a role in the buffet onset? Which numerical schemes are capable of predicting buffet? And which methods are currently used? Could existing methods be combined to achieve a greater accuracy in predicting buffet with respect to the (semi) empirical methods already used, without the extra computation time, and can these methods handle unconventional wing geometries?

Further questions to be answered are which numerical or empirical model is best be used to estimate buffet onset, how expensive is it from a computational time point of view, is it capable of investigating unconventional wing designs and what is the error margin to be expected in predicting the buffet onset wing lift coefficient over a specific range of freestream Mach numbers with respect to methods currently used in predicting buffet onset.

In this thesis work, only the wing and airfoil are considered, and the influence of thrust system, nacelles and other parts of the aircraft are neglected. Also, the assumption is made no leading edge or trailing devices such as vortex generators or high lift devices are present, as they can add momentum to the boundary layer. Since solving buffet problems, and account for buffet occurring anywhere else than at the wing (by means of interference) is part of the preliminary design phase, this simplification is justified.

1.3 Thesis Outline

This thesis will address the physical causes of transonic buffet In Chapter 2, as well as the methods used for buffet prediction. With this information, several approaches to create a new buffet onset prediction tool are created, and in the last section of Chapter 2, Section 2.2.4 a trade-off is made between the proposed methods. Chapter 3 focusses on the implementation of the new buffet prediction tool, and gives an overview of the various inputs and outputs required, steps taken and external programs used, in translating a wing geometry into a $M_\infty - C_L$ buffet onset diagram. Chapter 4 presents the results of a test case with the Fokker 100, and in Chapter 5 a conclusion is drawn on the accuracy, reliability and speed of the new buffet onset prediction tool. At the end of Chapter 5, recommendations are made on further development and use of this tool.

Chapter 2

Background

First of all, the focus will be on the question what buffet actually is. What are the physical causes, where does it originate? How is it predicted, postponed or cured? When is a vibration defined as the beginning of buffet? What are the operational regulations regarding buffet, and how does it affect the performance envelope?

2.1 Transonic Buffet

In general, the buffet envelope is one of the primary constraints in establishing the low and transonic speed performance capabilities of transport aircraft. Buffeting is a high-frequency instability, caused by airflow separation or shock wave oscillation which originates at a certain span wise section of the wing. It can be seen as a random forced vibration and, depending on for example the angle of attack of the aircraft and wing or tail geometry, the separated flow can result in an aerodynamic excitation. In that case, the separated boundary layer at the trailing edge can create a wake of turbulent flow, and when this wake hits the horizontal tail surface, buffet can affect the tail unit of the aircraft structure due to air flow downstream of the wing trailing edge. This immediately arises a new question on how buffet onset is defined, and what the physical meaning of the so called buffet margin is. To put things in a bigger perspective it is also interesting to know how buffet affects the operational performance and regulations of aircraft.

As mentioned above, the separated boundary layer induces a turbulent wake which might lead to forced vibrations experienced as buffet. The buffet margin, for a given set of flight conditions, is the amount of g-forces which can be imposed for a given level of buffet. The vibration induced by buffet can have a strong influence on the aerodynamic performance of the aircraft. Especially when it concerns the Eigen frequencies of the structure, it can also lead to structural damage or severe failure. Although this thesis work will focus on the buffet phenomena and prediction of it, not on the reaction of the structure on this aerodynamic phenomenon or vibrations in a different frequency domain like flutter, the latter will be addressed briefly.

Buffet is a term that is broadly used for high frequency vibrations in the aircraft structure. Important to note is that buffet is an effect, and not a physical cause. Interesting to know is what causes the boundary layer to separate. This viscous phenomenon, in which the role of shock wave boundary layer interaction plays an important role, will be discussed further on in this chapter. Besides this boundary layer shock wave interaction, this chapter addresses the total physical mechanism of transonic buffet will. What is actually happening when buffet occurs? What happens to the local airspeed, Mach number, shock wave strength and position, back pressure (does it rise or fall, and by how much?). Is there a critical pressure jump for which separation occurs? What is the role of the boundary layer and local Reynolds number? How is buffet detected in for example wind tunnel testing, and how is all this modeled in a simulation? All these questions form an essential starting point in understanding the buffet phenomenon, and being able to develop a prediction method for the conceptual design phase of transport aircraft.

There are different types of buffet, which al start with flow separation. Examples of several types of buffeting are:

- Wing flow separation exciting the wing structure
- Separated wing flow hitting another airplane component such as the horizontal tail
- Separated flow from e.g. spoilers hitting the horizontal tail
- Air intake flow breakdown, called inlet buzz
- Flow interference between external stores

In general, there are three different possibilities for flow separation to occur, that can lead to buffet. These three types of separation are:

1. Separation at the foot of the shockwave
2. Separation at the leading edge of the main wing
3. separation at the trailing edge of the main wing

Figure 2.1a and 2.1b show a digital 3-dimensional wake and flow pattern of vortices caused by separation at the leading edge. For example, wings with low sweep angles are generally characterized by leading edge or trailing edge separations, which form bubbles on the wing, that can cause the buffet onset. At transonic speeds, which is the focus of this thesis work, strong shock waves can induce buffet. This type of buffet is referred to as shock induced buffet.

Next to this, also the distinction between high speed and low speed buffet can be made. This thesis work will focus on the high speed, transonic, buffet onset. The characteristics of this high speed transonic buffet as discussed above will be explained in greater detail in the upcoming sections of this chapter.

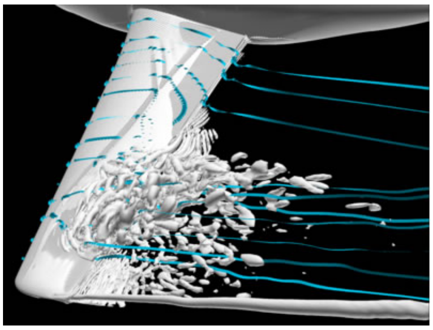

(a) Vortices

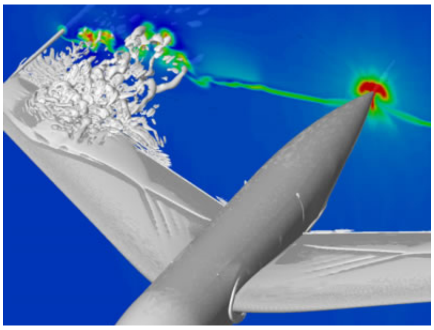

(b) Wake

Figure 2.1: Vortices and wake starting at the leading edge [3]

Buffet can also arise from localized flow separation originating from other local spots on the aircraft, such as the fuselage, spoilers or nacelles. Since this is considered to be rare, the assumption is made buffet originates from the main wing only. Question remains where is the buffet expected to be originating from, in span wise sense? It is highly likely buffet will originate at a span wise location at which the wing is highly loaded. That is, where the local lift coefficient c_l is highest. This can be investigated with a relative simple panel method, after which a cut in the wing section can be made to go from the 3-dimensional wing to the 2-dimensional airfoil case, for further detailed investigation. More on this approach in the section on numerical prediction method selection.

From an operational point of view it is necessary to define a certain buffet onset point, and construct an envelope in which the aircraft can maneuver without encountering buffet. What is the buffet envelope exactly, and what is defined as the buffet margin? The buffet envelope is presented as a limitation defined by flight test, and the onset is identified as the speed or Mach number and lift coefficient combination at which the vibration reaches $\pm 0.050g$. This means the $1.0g$ buffet onset does not represent a strict physical limit of the actual flight domain of the aircraft, it more or less sets a boundary between a safe flight region, and a part of the flight envelope in which one may encounter serious control problems or the structure is significantly affected by e.g. fatigue loads. In this regime, the aircraft's structure shakes due to this excitation, and the buffeting may endanger the stability of the flight. Buffet can also be seen as stall warning. Some buffeting can be felt from the turbulent flow above the wings as the stall is reached. One could ask how buffet influence the flight control. When buffet occurs, the pilot will notice the flight controls have become less responsive and feel the vibrations induced by buffet. A so called buffet onset graph is shown in figure 2.2. These figures show the combination of lift coefficient and Mach number at which buffet starts, and the (very basic) influence of certain wing parameters on this onset boundary.

There is a second phenomenon which is also based on induced vibrations, called flutter. Flutter is a dynamic aeroelastic phenomenon, and is a self-feeding and potentially destructive vibration where aerodynamic forces on the wing couple with the structure's natural mode of vibration. This produces a rapid periodic motion. If the energy during the period of aerodynamic excitation is larger than the natural damping of the system, the level of vibration will increase, resulting in a potentially destructive self-exciting oscillation.

Because of this, wings, airfoils and all structural elements that experience aerodynamic forces are to be designed carefully within known parameters to avoid flutter. Just as is the case with buffet, the best way to predict this behavior is through detailed testing. Even changing the mass distribution of an aircraft or the stiffness of one component can induce flutter in an apparently unrelated aerodynamic component. A mild form of flutter can be a so called buzz in the aircraft control system, but when becoming more violent, it can develop uncontrollably with great speed and cause serious damage to or the destruction of the aircraft. [15]

To understand buffet, it's physical causes and develop a way of predicting the buffet onset, some basic aerodynamic concepts regarding transonic flow over a wing and airfoil need to be elaborated. This chapter touches upon some of the basic aerodynamics involved, and in the final section focuses on a trade-off between various schemes to predict buffet. The advantages and disadvantages of several frequently used models is discussed, and some conceptual ideas are formulated on how to combine these tools to proceed with the development of the buffet prediction tool.

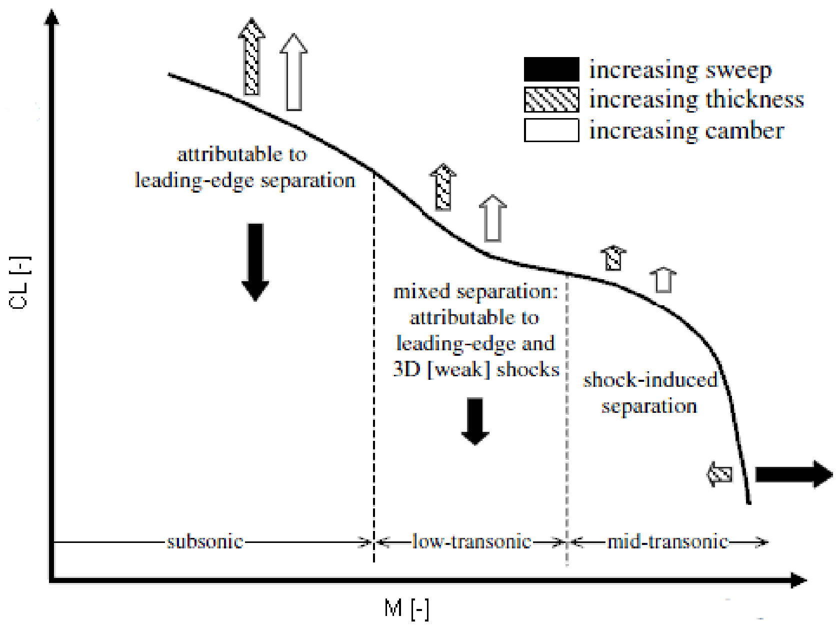

Figure 2.2: Buffet onset, lift coefficient versus freestream Mach number and influence of several wing parameters [1]

2.1.1 Transonic Flow

Buffet is a viscous phenomenon, which makes predicting the shockwave position and strength, as well as the shockwave boundary layer interaction, and there for the buffet onset, complicated. To do this in an efficient way without exponential increase in computational time, and having the ability to investigate unconventional wing geometries, is one of the challenges in this thesis work. Since transonic buffet is the result of trailing edge flow separation and instable shock wave movement, it looks relatively straight forward that buffet will originate from the wing and not somewhere else on the aircraft. The flow over an airfoil in transonic conditions is characterized in figure 2.3. Transonic flow can be divided in three sub-domains:

1. Subsonic domain
2. Sonic domain
3. Supersonic domain

Transonic phenomena occur for both subsonic and supersonic free-stream flows, because of the higher than free-stream Mach numbers on top of the (positively cambered) airfoil. From figure 2.3 it can be seen that at higher free-stream Mach numbers the subsonic domain becomes so small that it is almost non existing. The most important aspect that distinguishes transonic from both supersonic and subsonic flow is the fact that the disturbance propagation velocity and the local fluid velocity are comparable in magnitude. [4] In classical subsonic and supersonic flow theory the assumption is made that the local speed of sound is significantly higher and in the latter case significantly lower than the local velocity of the air. This allows the disturbance propagation mechanism to be uncoupled from the local flow phenomena. Transonic flow on the other hand cannot say to be uncoupled in that manner, which implies the nonlinear coupling between the local velocity field and the propagation velocity of the perturbations have to be included in the fundamental flow equations by some additional nonlinear terms. This complicates the system considerably. [4]

2.1.2 Laminar and Turbulent Airfoils

There is a difference in geometry and corresponding pressure distribution for laminar and turbulent airfoils. Both the laminar and turbulent airfoil have their own characteristics, advantages and disadvantages. Generally, the difference between a laminar and turbulent airfoil lies in the thickness and camber distribution of the airfoil, and the way the leading and trailing edge are shaped. A laminar airfoil may be useful for reducing skin friction drag, increasing maximum lift, or reducing heat transfer. It can produce lots of lift and low drag, but perform dramatically when the flow becomes turbulent due to for example roughness, dust or insects on the leading edge of the airfoil. Another problem with laminar airfoils arises when separation occurs before transition. That is, when the flow becomes separated before it turned turbulent. This laminar separation can create a laminar separation bubble, which turns turbulent in that process, and then re-attaches to the airfoil because mixing in a turbulent boundary layer is much more efficient than in a

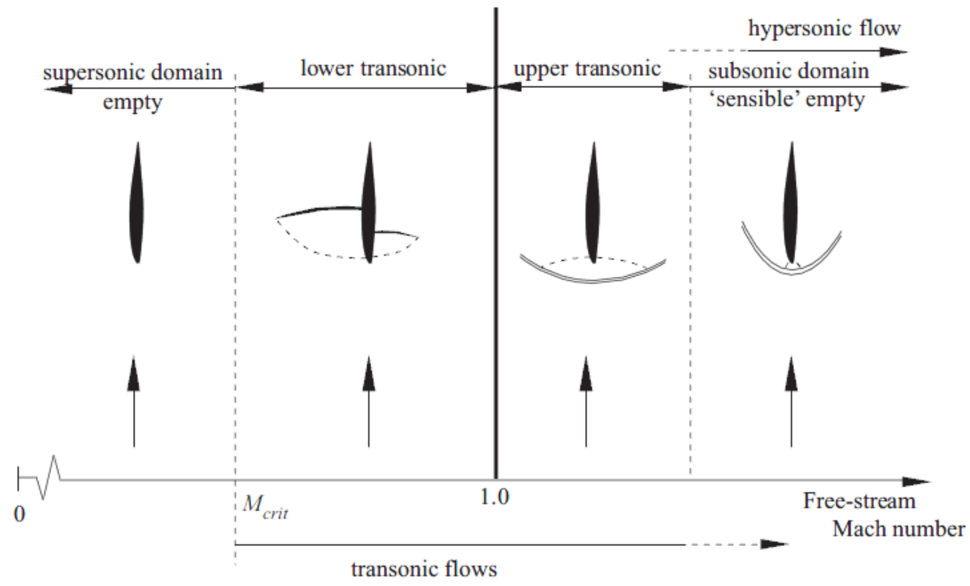

Figure 2.3: Basic classes of transonic flows [4]

laminar boundary layer. Under certain conditions the turbulent flow may fail to reattach to the surface. This phenomenon is called bubble bursting. After bubble bursting, the lift of an airfoil decreases sharply and the drag increases. [6] As can be seen in the section on boundary layer flow further on in this chapter, and figure 2.11 on Stratford's limiting pressure gradient, a turbulent boundary layer can handle much steeper adverse pressure gradients without leading to separation than a laminar one. Since this thesis is about the transonic regime, the use of laminar airfoils is excluded and there is no need to take laminar separation bubbles and so on in to account.

2.1.3 Supercritical Airfoil

Considering the typical supercritical airfoil as depicted in figure 2.4 on the right, normal shock waves exist on top of the airfoil section. When the local Mach number increases due to for example an increase in angle of attack (leading to a higher lift coefficient) or simply an increase in the free stream Mach number, the shock wave will move aft. The application of super critical airfoil sections, leads to a large relative thickness and a large leading edge radius and thus higher lift coefficients when compared to the sonic rooftop airfoil, as can be seen on the left in figure 2.4. Though on the other hand, the sonic rooftop airfoil has a higher drag divergence Mach number. Supercritical airfoil technology has not only allowed higher design lift coefficients, but has also led to improvements with respect to buffet onset boundaries compared to designs using sonic rooftop airfoils.

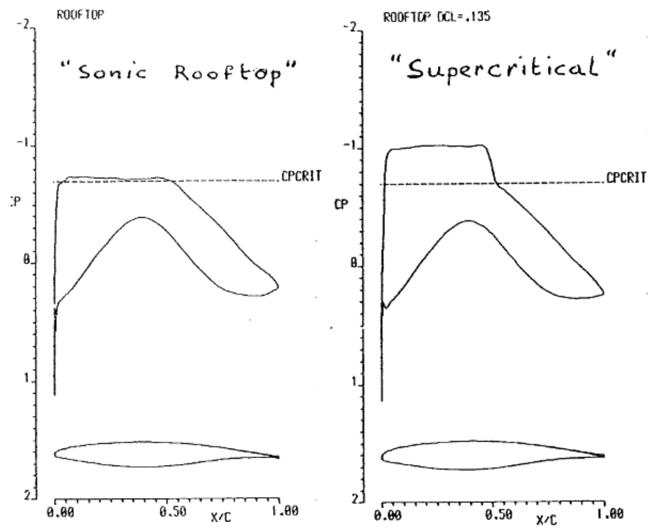

Figure 2.4: Typical sonic rooftop and super critical airfoil characteristics [5]

2.1.4 Boundary Layer Flow

Considering transonic flow over a supercritical airfoil as mentioned in the section above, the flow very close to the physical boundary (surface of the airfoil) will develop viscous forces. This thin layer of air is called the boundary layer. The pressure and shear stress acting on the airfoil are shown in figure 2.5. For a detailed calculation of velocity field and pressure distribution over the complete airfoil, boundary layer effects have to be incorporated. One way to do this is with the use of the boundary layer displacement thickness δ^*. The boundary layer δ is built up in the following way as is shown in a sketch figure 2.6. Two important parameters, the boundary layer displacement thickness and momentum loss thickness, defined respectively as δ^* and θ (derived through the use of conservation of mass) are the input for another important boundary layer parameter, the so called shape factor H. The shear stress as denoted by τ in figure 2.5 at the wall is given by equation 2.1. From this equation it can be seen that next to the viscosity μ, the wall shear stress is a function of the velocity gradient.

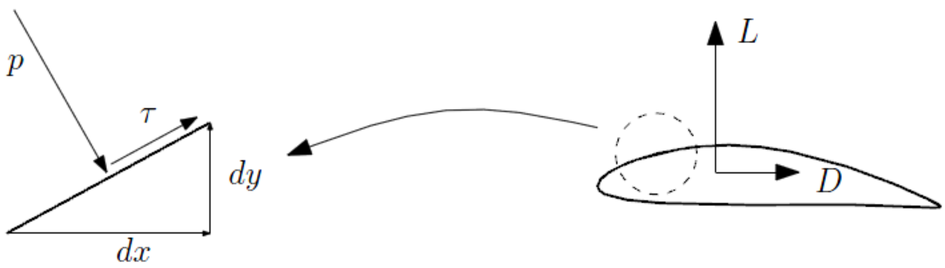

Figure 2.5: Pressure and wall shear stress acting on an airfoil [6]

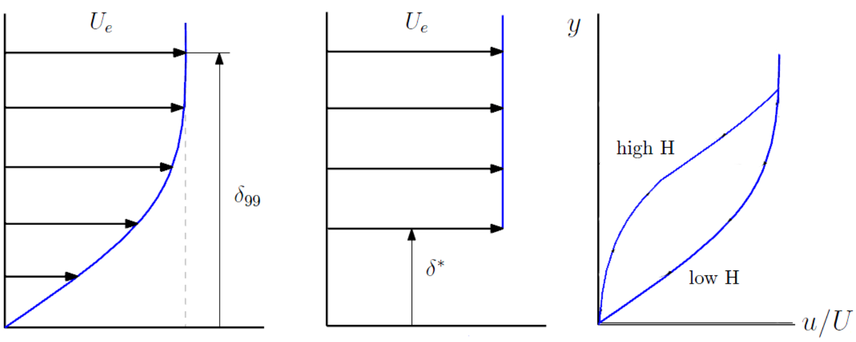

Figure 2.6: Boundary layer displacement thickness and shape factor [6]

$$\tau_0 = \mu \left(\frac{\partial u}{\partial y} \right)_0 \tag{2.1}$$

$$\delta^* = \int_0^\infty \left(1 - \frac{u}{U} \right) dy \tag{2.2}$$

$$\theta = \int_0^\infty \frac{u}{U}\left(1 - \frac{u}{U}\right) dy \tag{2.3}$$

$$H = \frac{\theta}{\delta^*} \tag{2.4}$$

θ, δ^* and H are all highly dependent on the shape of the velocity distribution U in the boundary layer. Important to realize is that the shape of the velocity distribution in the turbulent boundary layer is determined experimentally. The higher the value of H the stronger the adverse pressure gradient. A high adverse pressure gradient can greatly reduce the Reynolds number at which transition into turbulence may occur. There are two different types of boundary layers, the laminar boundary layer and turbulent boundary layer.

Laminar Boundary Layer

The laminar boundary layer shows a distinct velocity profile, called the Blasius profile. In this laminar boundary layer, the exchange of momentum takes place at a microscopic (molecular) scale due to shear stress. In the turbulent boundary layer transport of momentum is very large due to large scale motions of the air molecules. This implies two types of shear stress: laminar shear stress and turbulent shear stress. As a result, the flow velocities close to the airfoil surface are much higher in a turbulent boundary layer than in a laminar one, which leads to a higher drag due to shearing forces [6]. Turbulent and laminar boundary layers behave very differently and have to be treated in a separate way. A reasonable assessment of whether the boundary layer will be laminar or turbulent can be made by calculating the Reynolds number of the local flow conditions. Since buffet is a viscous phenomenon, which is a result of shock wave boundary layer interaction, this has to be accounted for in this thesis research.

Turbulent Boundary Layer

In a turbulent boundary layer, two main layers can be identified: The viscous sub layer, and the turbulent core region. In the turbulent core region strong fluctuation in a large region of the boundary layer occur, until very close to the wall, where the viscous sub layer begins. The turbulent shear stress dominates over viscous shear stress (the total shear stress is the viscous shear stress and the turbulent shear stress together). Furthermore a large effective viscosity and small velocity gradient occur. In the viscous sub layer fluctuations are very small towards the wall due to the so called no-slip condition. This condition implies that at a solid boundary, like the surface of an airfoil, the air will have zero velocity relative to the boundary. One can think of this condition as the outermost molecules of the fluid are stuck to the surfaces over which the flow runs. The relative fluctuations are still present, but momentum transport is less effective and the viscous shear stress dominates over turbulent shear stress. Here, a small effective viscosity and high velocity gradient can be seen [7].

The boundary layer flow is best represented by the boundary layer equation shown in equation 2.5. In this laminar boundary layer equation, the pressure term is hidden in the right hand side (RHS) of the equation, because one can relate the external flow properties to the pressure gradient via the first compatibility relation shown in equation 2.6 relating velocity profile to pressure gradient. For example, when we consider a flat plate, with no pressure gradient, this term drops out. when considering a turbulent boundary layer, an extra term can be added to the RHS, being the Reynolds stress term, which consists of $\frac{1}{\rho}\frac{\partial}{\partial y}\left(\overline{\rho u'v'}\right)$. Modeling this turbulent boundary layer Reynolds stress term is discussed later on.

$$u\frac{\partial u}{\partial x} + v\frac{\partial u}{\partial y} = u_e\frac{\partial u_e}{\partial x} + \nu\frac{\partial^2 u}{\partial y^2} \tag{2.5}$$

$$\nu\left(\frac{\partial^2 u}{\partial y^2}\right) = \frac{1}{\rho}\frac{dp}{dx} \tag{2.6}$$

When looking at the velocity profile within the boundary layer, again different regions can be defined. These three regions are:

1. Inner layer
2. Outer layer
3. Overlap layer

In the inner layer, the flow does not depend on free stream conditions. The flow depends on conditions near the wall; there is no direct effect of the free-stream. In the outer layer on the other hand, flow does not depend on wall conditions. The flow depends on free stream conditions; there is no direct effect of the wall conditions. All relatively straightforward. The overlap layer is, as the name suggests, a sort of intermediate region. [7]

When zoomed in on the inner layer only, the following layup of this part of the boundary layer can be defined:

1. Linear viscous sub layer
2. Buffer layer
3. Overlap layer

The difference in these layers with respect to the shear stress is, that in the viscous sub layer the viscous shear stress is dominant and in the overlap layer, the turbulent shear stress is dominant (as was already mentioned in the previous paragraph). In the buffer layer, they are of comparable magnitude. Considering the thickness of the boundary layer and the viscous layer, one could say the viscous layer is only a very small fraction of the total boundary layer thickness. When the boundary layer thickens with the length of the profile, it is important to note that the viscous layer thickness remains nearly constant.

The development of the two different components in the shear stress with increasing profile length, can be seen in 2.7 with y^+ being the location parameter in wall coordinates or wall units. These wall coordinates are the distance y to the wall, made dimensionless with the friction velocity u_t and kinematic viscosity ν.

$$y^+ = \frac{y u_T}{\nu} \tag{2.7}$$

$$u_T = \sqrt{\frac{\tau_w}{\rho}} \tag{2.8}$$

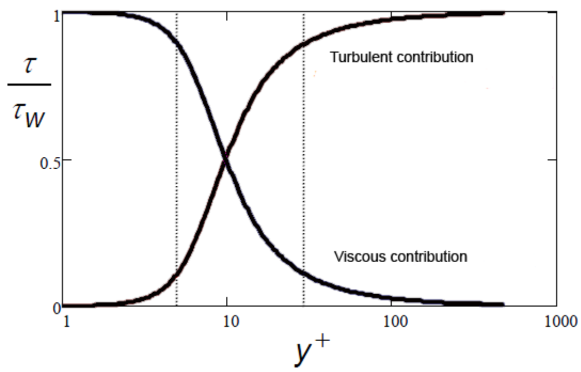

Figure 2.7: Shear stress components contribution in the boundary layer [7]

When shock-induced buffet occurs, the type of boundary layer to be dealt with is the turbulent one. Because buffet always begins with separation, the boundary layer present when the movement of the shock will induce buffet, has to be turbulent. The transition from laminar to turbulent boundary layer will be much earlier on the airfoil, generally in the order of $5 - 10\%$ of the chord.

What does all this boundary layer information imply? When the velocity distribution over the section is determined, and a detailed pressure distribution can be obtained by analyzing the airfoil with a certain (relatively simple) numerical code, the displacement thickness can be added to the contour of the airfoil, and the flow conditions can be calculated again over the new contour, as the boundary layer displacement thickness adds to the camber, radius and general contour of the airfoil [5].

Using an approximation for the shape factor of the boundary layer given by literature [6, 7], being $H = 2.6$ near the point of minimum pressure (the so called suction peak) there might be a way to incorporate the boundary layer effects, because this point of high suction (or low pressure $C_{p_{min}}$) is highly likely to be of interest when predicting buffet onset as is shown later on in this chapter. Other possibilities might be the use of a boundary layer model, depending on which type of numerical model selected.

When modeling the boundary layer, usually the total boundary layer is divided into two regions (instead of all the sub layers discussed above), simply being the inner and outer layer. The inner layer (including the viscous sub layer en overlap layer) is the part where:

$$\frac{y}{\delta} < 0.1 - 0.2 \tag{2.9}$$

And outer layer (also referred to as the wake region) is the part where:

$$\frac{y}{\delta} > 0.1 - 0.2 \tag{2.10}$$

Some additional information on the numerical way these boundary layer models are implemented is discussed in the section on numerical prediction methods (the paragraph on boundary layer models).

Boundary layer transition process

The process of transition from a laminar to turbulent boundary layer is quite complex and hard to predict. Determining whether a laminar or turbulent flow occurs is not that relevant when predicting buffet, because separation always follows transition, and not the other way around. This only occurs in the case of laminar separation bubbles, but it is assumed in transonic conditions no laminar profile will be present. It is found that in practice transition from laminar to turbulent flow is influenced by the following:

- Reynolds number
- Pressure gradient
- Sound (pressure fluctuations)
- Surface vibration
- Turbulence level of the flow
- Flow control techniques, e.g. boundary layer suction or surface temperature control
- Surface roughness (insects, rain, ice, rivets)

Graphically the process of transition is shown in figure 2.8. First, steady laminar flow becomes unstable at sufficiently large Reynolds numbers. Then unsteady 2-dimensional Tollmien-Schlichting waves appear that grow inside the boundary layer to 3-dimensional waves, which evolve in to spanwise vortices. Turbulent spots form, which eventually grow to fully turbulent flow at the end of the transition process, which leads to drastic changes in the boundary layer behavior. When trying to postpone transition with the help of flow control techniques, one essentially tries to suppress the amplitude of the Tolmien-Schlichting waves.

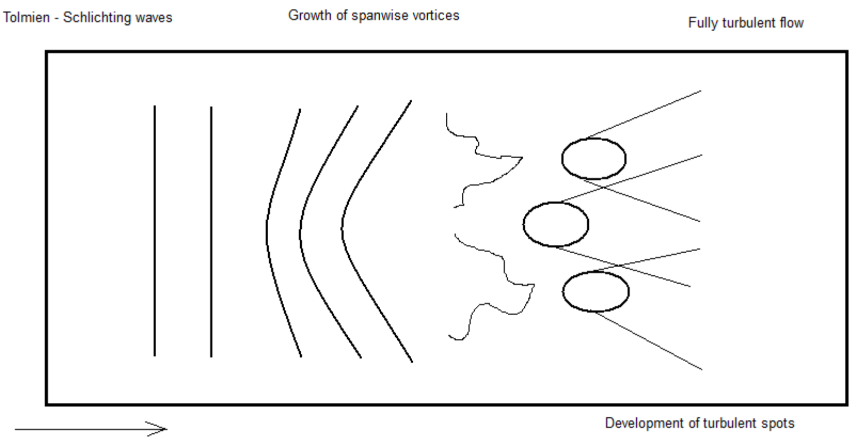

Figure 2.8: Boundary layer transition process, modified from [6]

Effects of Pressure Gradient on Boundary Layer Stability

Stability theory states that the inflection point in laminar boundary layer leads to instability. [6] Considering the Prandtl boundary layer equation 2.11 again, with the pressure term instead of the external flow parameters, it yields:

$$u\frac{\partial u}{\partial x} + v\frac{\partial u}{\partial y} = -\frac{1}{\rho}\frac{\partial p}{\partial x} + v\frac{\partial^2 u}{\partial y^2} \tag{2.11}$$

And at the physical boundary of the airfoil, the surface, where $y = 0$, the velocity components u and v are zero, as indicated in equation 2.6, it yields a negative pressure gradient is more favorable than a positive pressure gradient. In practice it has been found that the point of instability on an airfoil occurs very close to the point where the pressure gradient changes from favorable to adverse [6].

Vortex Generators

The influence of a vortex generator, added to add momentum to the boundary layer, on the boundary layer is shown in Figure 2.9a and 2.9b. In this figure it is shown the presence of a vortex pushes the larger velocity regions of the boundary layer downwards, which means the velocity and thus the shear stress τ increases, which postpones separation. The $\frac{dU}{dy}$ shown in these figures is a measure for separation. When this gradient becomes larger, separation is more likely to occur.

Kutta condition

For an inviscid flow the undisturbed free stream velocity and the geometry of the airfoil do not determine the strength of the circulation. Inviscid flow uses the simplifying assumption of an ideal fluid (air) that has no viscosity. However for a sharp trailing edge (TE), experiments have shown that the flow leaves the TE smoothly, which means the

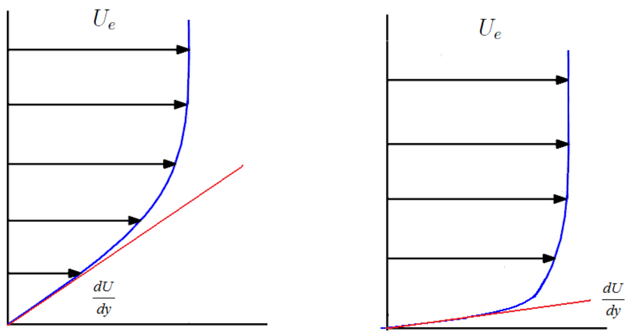

(a) Boundary layer without vortex generator

(b) Boundary layer with vortex generator

Figure 2.9: Influence of vortex generator on boundary layer

flow from the upper and lower side merge smoothly into the wake. This observation has led to the Kutta-Condition which states that a body with a sharp trailing edge produces a circulation such that the stagnation point is fixed at the trailing edge and the velocities the upper and lower side meet tangentially such that the velocities at both sides are equal [16]. In other words, the proper choice of the circulation should be such that smooth flow from the trailing edge is obtained. When the results of this theory are compared with measured lift characteristics, it is found that the actual lift-curve slope may be 10 to 20% less than the theoretical value. The reduction seems to depend on the boundary layer thickness on upper, δ_u and lower surface δ_l and hence on the Reynolds number, since high Reynolds number implies a thinner boundary layer. Especially the boundary layer characteristics near the trailing edge seem to be important. The so called modified Kutta condition accounts for this TE boundary layer characteristics, as can be seen in figure 2.10. It is this modified Kutta condition that appears to be the weakest point in most of the computer programs for the analysis and design of airfoils [6]. As will become clear in section 2.2 on numerical prediction methods, and especially the section on non-isentropic potential flow, using the correct, modified Kutta condition is an important part of obtaining the correct results in a flow approximation.

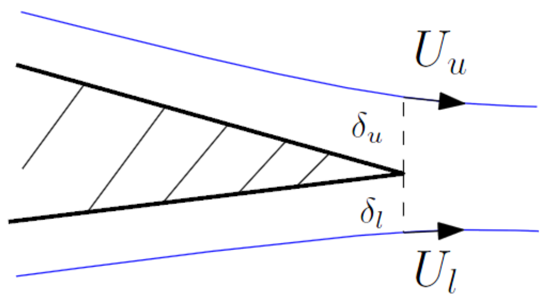

Figure 2.10: Modified Kutta condition for sharp trailing edge [6]

2.1.5 Flow Separation

Flow separation occurs when the boundary layer travels far enough against an adverse pressure gradient $\frac{dp}{dx}$ such that the speed of the boundary layer relative to the surface of the airfoil falls almost equal to zero. In other words, an adverse pressure gradient imposed on the boundary layer by the outer flow. Increasing the pressure means increasing the potential energy of the flow, leading to a reduced kinetic energy and a deceleration of the air. When this happens the wall shear stress will decrease, and will fall almost to zero. This is exactly what triggers separation, as the air is no longer 'pulling' on the wall and opposing flow can develop which effectively pushes the boundary layer off of the wall. The airflow detaches from the airfoil and (random) vortices form a wake. Flow separation often results in increased drag, particularly in pressure drag rise. The separation of the air creates turbulence and results in pockets of low and high pressure that leave a wake behind the airfoil. This opposes forward motion and is a component and thus a form of drag. One could see this as a pressure imbalance that occurs due to the separated boundary layer, resulting in pressure drag. Therefore, one of the main goals in aerodynamic design is to delay flow separation and keep the local flow attached for as long as possible. In general, minimizing the pressure drag amounts to preventing or delaying boundary layer separation [5]. When boundary layer separation occurs, a portion of the boundary layer closest to the surface experiences reversed flow. As a result, the overall boundary layer initially thickens suddenly and is then forced off the surface by the reversed flow [16].

The tendency of a boundary layer to separate primarily depends on the distribution of the adverse velocity gradient along the surface of the airfoil. But here is a difference between the laminar and turbulent case. The general magnitudes of this adverse pressure gradient required for separation is much greater for turbulent than for laminar flow. In other words, the more efficient mixing of the air which occurs in a turbulent boundary layer reduces the boundary layer thickness and increases the wall shear stress, often preventing the separation which would occur for a laminar boundary layer under the same conditions. This can be seen when examining Stratford's limiting pressure distribution. This boundary layer is on the verge of separation at every location, meaning a wall shear stress of $\tau_0 = 0$ and no skin friction $C_f = 0$. When the accompanying pressure distribution is computed, it can be seen that the turbulent boundary layer can handle a much larger adverse pressure gradient $\frac{dC_p}{dx}$ than the laminar boundary layer. This can be seen in figure 2.11. On the horizontal axis a scaled x-coordinate is plotted with respect to a flat plate approximation used from $0 < x < x_m$ [6].

Another important parameter in the flow separation process is the Reynolds number. One could see the influence of the Reynolds number on the separation of flow as some sort of 'resistance' against separation. The separation is postponed slightly with increasing Reynolds number in case of a turbulent boundary layer. In case of a laminar boundary layer, the separation resistance is independent of Reynolds number [16].

The negative effects of a thickening boundary layer, that eventually leads to separation, are clear; The increase in δ^* has a great effect on the outer flow and pressure field. It is likely this change in the pressure field will results in an increase in pressure drag, and if severe enough it can lead to a loss of lift or stall and therefore also lead to buffet onset.

As a result of boundary layer separation shedding vortices can occur. These vortices, known as the Von Karman vortex sheet 2.12 can occur at a certain frequency, which can induce vibrations to the structure of the wing. The air flow past the object creates alternating low-pressure vortices on the downstream side of the object. If the frequency of vortex shedding matches the resonance frequency of the structure, the structure will begin to resonate and the structure's movement can become self-sustaining, as described earlier. In that case, these vibrations can lead to serious structural failure. This is a different phenomenon than buffet, and is likely to occur at different frequencies, much closer to the f_n Eigen frequency of the structure and resembles flutter.

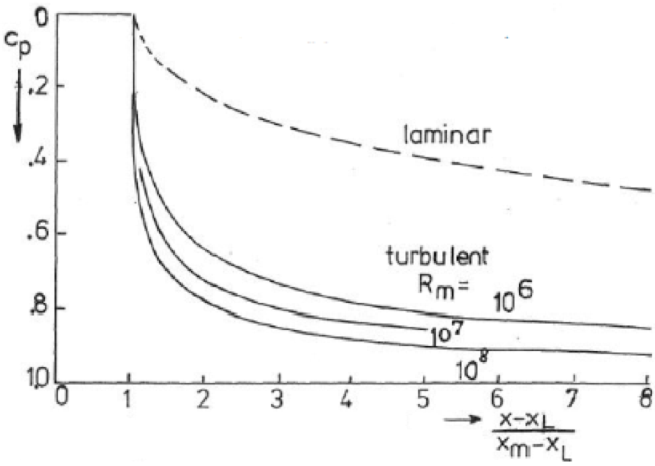

Figure 2.11: Stratford's limiting pressure distribution [6]

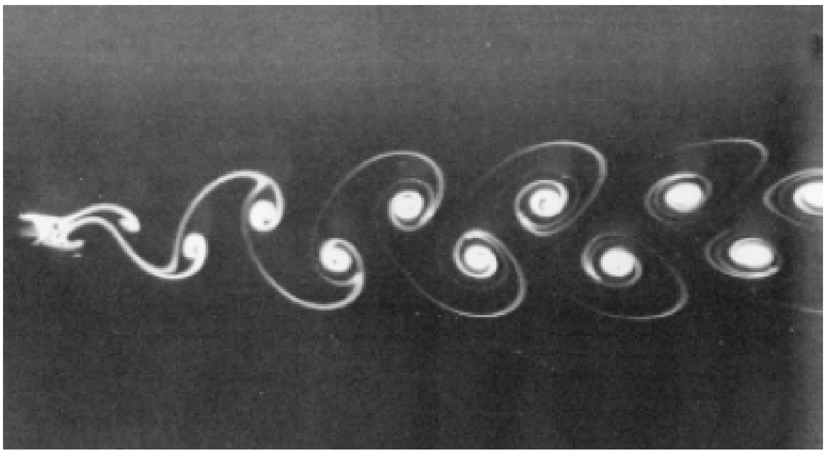

Figure 2.12: Von Karman vortex street behind a cylinder placed in uniform flow [8]

2.1.6 Shock Waves

One of the key aspects in predicting buffet onset at transonic speeds is the fact shock waves are present on the top (and bottom) of the airfoil. Hence the name, shock induced buffet. However, a local Mach number $M_{local} > 1$ does not automatically mean there will be a shock wave on the airfoil, as up to a $M_{local} = 1.4$ isentropic recompression is possible without the formation of a shock wave. [16]

Shock waves are characterized by an abrupt change in the characteristics of the flow. Across a shock there is an extremely rapid rise in pressure, temperature and density of the flow. From an conservation of energy point of view one can say the total energy is conserved, total temperature and enthalpy stay the same, but the energy which can be extracted as work decreases as the entropy increases. Vorticity is generated by shock waves due to this variation of entropy along the shock. In the following sections it will become clear that this increase in entropy is one of the complicating aspects of simulating shocks in a numerical model. One could see this change in flow parameters as follows; Because the pressure disturbance cannot propagate upstream in supersonic flow, the air is forced to change its properties (temperature, density, pressure, and Mach number) when in contact with a body. When this is done in a somewhat violent manner, a shock wave forms. Several different kind of shocks can be distinguished:

- Normal shock: perpendicular to the air flow direction.
- Oblique shock: at an angle to the direction of flow.
- Bow shock: Occurs upstream of the front (bow) of a blunt object when the upstream velocity exceeds Mach 1.

Since this thesis will address transonic flows and the upstream velocity does not exceed $M_\infty = 1$ no bow shocks or oblique shock waves are expected. On the top of the airfoil the supersonic patch of flow is decelerated to subsonic flow through a normal shock, at transonic flow conditions. The strength of the shock is of great influence in to which extend a certain analyses can be carried out with acceptable results, as will become clear in the section on numerical prediction methods in Section 2.2.2.

When an airfoil is subjected to transonic flow and the flow is decelerated to subsonic speeds, a recompression shock can form on top of the airfoil. The air is compressed, meaning the pressure and density have both increased compared to the supersonic patch in front of the shock. The formation of this recompression shock can be seen in this figure 2.13. A recompression shock and an adverse pressure gradient both result in an increasing pressure, but the manner in which they increase pressure is different. The shock is an instant increase in pressure, and the adverse pressure gradient results in a gradual rise in pressure. However, they both can cause separation.

These recompression shocks can occur from the moment on where the local Mach number on top of the airfoil equals 1 or higher. From this critical Mach number, M_{crit}, the free stream velocity is still substantially below Mach 1, but the Mach number at which some

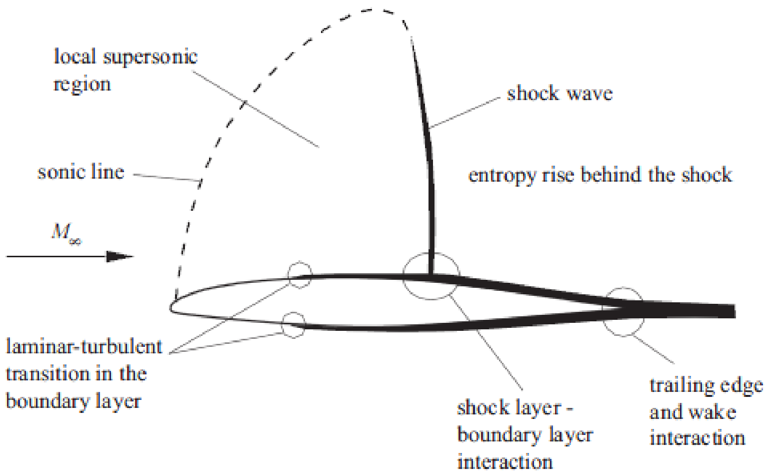

Figure 2.13: Representation of transonic flow over an airfoil with attached boundary layer [4]

portion of the airflow over the wing first equals Mach 1. The position of the shock is determined by the point where the air flow suddenly returns to subsonic flow, this is where the shock wave forms. This shock wave becomes more severe and moves aft on the wing as speed over the wing's top surface is increased, and eventually flow separation can occur.

Why is the formation of a shock so detrimental for the performance of an airfoil? This is because the pressure increase behind the shock means loss of suction, and could lead to loss of lift. Due to the expansion and compression waves that originate from the leading edge of the wing, the suction peak is flattened, so the $C_{p_{min}}$ is less negative, meaning loss in suction. The shock also interacts with the boundary layer as is discussed in the section on shock wave boundary layer interference, later on in this chapter. The increase in pressure drag, as addressed earlier on, is caused by a thicker boundary layer, and thus a larger wake. When the strength of the shock increases, there are two drag rise effects to be noticed that have a different cause. First, the thickened boundary layer and wake will result in pressure drag. The shock wave itself will induce an increasing wave drag.

Besides the effects mentioned above, the shock waves cause shock induced buffet, a condition where the separation and the shock interact in a resonating condition. This shock induced buffet can cause resonating loads on the underlying structure and can be an indication of buffet onset. Beside the shock strength, the position of the shock wave is also of great importance when trying to determine a correct and detailed pressure distribution over an airfoil [5].

When looking at shock waves from a numerical point of view, they tend to complicate the approximation methods for the flow, because they introduce entropy and thus rotation to the flow. For example the potential flow method cannot cope with this entropy change, but there are ways to correct for this rotation in the flow. The effect of this on different numerical models is discussed in detail in the numerical prediction methods paragraph, at the end of section 2.2.

Hugonoit-Rankine Shock Equations

When a shockwave is present, the flow through a shockwave is dominated by viscous and heat-transfer interactions. However, because the shock is a relatively thin layer, it can be assumed to be a mathematical discontinuity in for example the Euler equations. One of these discontinuities is the change in pressure across the shock wave. Physical quantities are rarely discontinuous, so in real flows these discontinuities are smoothed out by the viscosity of the flow. If the pressure before the shock is denoted with p_1 and the pressure behind the shock with p_2, their ratio across a normal shock wave will be:

$$\frac{p_2}{p_1} = \frac{(\gamma + 1)\rho_2 - (\gamma - 1)\rho_1}{(\gamma + 1)\rho_1 - (\gamma - 1)\rho_2} \tag{2.12}$$

This equation is known as the Hugonoit-Rankine equation. In transonic flow when a shock is present, two cases can be distinguished: Either the position of the shock is known, or unknown. If the position of the shock is known, the Hugonoit-Rankine equation can be used to find the pressure jump across the shock wave and to find other relations like the change in temperature, density, and entropy to determine the conditions after the shock. On the other hand, if the position of the shock is unknown it will show up in a pressure plot of the flow as a very large pressure gradient. Which is physically and mathematically incorrect [4]. This information regarding the position of the shock, is one of the key aspects in developing a prediction method for buffet onset, as will be discussed in the chapter on numerical methods together with a more detailed explanation on the shock conditions mentioned above.

To be able to assess the quality, advantages and shortcomings of several (numerical) approximation methods, it is convenient to have some sort of benchmark. The Rankine-Hugoniot conditions, also referred to as Rankine-Hugoniot jump conditions or Rankine-Hugoniot relations, relate to the behavior of shock waves traveling normal to the flow. They are named in recognition of the work carried out by Scottish engineer and physicist William John Macquorn Rankine and French engineer Pierre Henri Hugoniot. Rankine was the first to show that within the shock a non-adiabatic process must occur. Hugoniot showed that when we neglect viscosity and heat conduction, the conservation of energy implies conservation of entropy in smooth regions and a jump in entropy across a shock. This last remark could be of importance for this thesis research. In general, without going into too much detail at this point, these conditions are based on conservation laws and define a shock (discontinuity or abrupt change) in the system. [17] In the section on numerical prediction methods, several approximation models with the Rankine-Hugoniot case as benchmark will be addressed.

Shock Wave Boundary Layer Interaction

Interesting to know is how the turbulent boundary layer and shock wave interact. Is there a difference in interaction between the boundary layer and a normal shock, with respect to an oblique shock? Does the interaction go as far as in to the inner (viscous) sub layer of the boundary layer, or is only the outer part of the boundary layer interacting with the shock?

What happens at the physical boundary (e.g. the wall or upper surface of the airfoil) is that the air is brought to a rest. Unless there is separation, or extraordinary pressure gradients, the flow external to the boundary layer is substantially independent of the boundary layer flow. The boundary layer however, depends strongly on the pressure distribution and velocity profile of the flow. Since Shock waves are a viscous phenomenon, viscosity and heat conduction play an important role, as is the case with boundary layers. The major difference between the two is that a shock wave is considerably thinner than a boundary layer. This results in a difference in pressure gradient in a shockwave and a boundary layer. When shock waves appear in the vicinity of a surface, the large pressure gradients have an effect on the boundary layer that is propagated downstream and upstream through the subsonic part of the boundary layer (in the supersonic part of the boundary layer, information cannot propagate upstream). As a result of this shock wave boundary layer interaction, compression and expansion waves are pushed into the outer (external) flow. These waves will in their turn tend to influence the original shock wave pattern. Figures 2.14a and 2.14b visualize this situation. In these two figures, the resulting case is shown for a turbulent boundary layer and a turbulent boundary layer with separated zone [9]. The reflected waves are also called Prandtl-Meyer expansion waves. Note that in these figures, literature provides an oblique shock wave case instead of a normal shock which is expected to form on top of the airfoil in transonic buffet onset.

The interaction of shock wave and boundary layer can be viewed as some sort of competition between a flow with viscous forces and an abrupt pressure rise. The result of this conflict depends on the pressure rise magnitude and the boundary layer characteristics, such as laminar or turbulent state, as can be seen in Figure 2.11. Looking at the boundary layer equation for the streamwise momentum for a steady flow, which is given by Equation 2.13, in which τ represents the shear stress, the central part expresses the streamwise derivative of the flow momentum. An adverse pressure gradient will make this momentum decrease. The shear stress in the boundary layer inner part counteracts the adverse pressure gradient by transferring momentum from the higher velocity regions to the lower velocity regions near the surface of the airfoil, the physical boundary. [18]

$$\rho u \frac{\partial u}{\partial x} + \rho v \frac{\partial u}{\partial y} = \frac{\partial}{\partial x}\left(\rho u^2\right) \frac{\partial}{\partial y}\left(\rho u v\right) = -\frac{dp}{dx} + \frac{\partial \tau}{\partial y'} \tag{2.13}$$

The question remains to which extend the presence of a shock changes the boundary layer flow. How far does the shock disturbance propagate towards the surface? As seen in the paragraph on boundary layer flow, several layers can be identified within the boundary layer. In the example shown in 2.15 a relatively weak shockwave is shown, and the sonic line is not so deep into the boundary layer that it induces separation. When the shockwave strength increases, the interaction becomes strong and the sonic line descends into the lower layers of the boundary layer resulting in flow separation. The location of the sonic line is determined by the boundary layer velocity profile. The velocity profile, in turn, is a function of the pressure gradient under which the boundary layer had developed before encountering the interaction, as is discussed above [4]

There is a significant difference in interaction between the shock wave and a laminar boundary layer, or a turbulent boundary layer. As a result of the momentum being

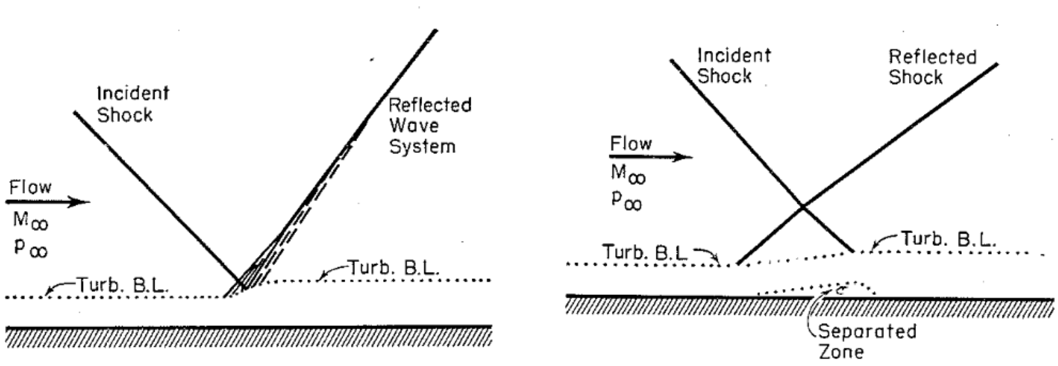

(a) No separated zone (b) With separated zone

Figure 2.14: Shock wave boundary layer interaction for a turbulent boundary layer [9]

transferred into the boundary layer, and the resulting capability to handle larger adverse pressure gradients, the effect of a shock on a turbulent boundary layer is much smaller than in the laminar boundary layer case. There will be only a moderate thickening of the boundary layer and the influence in downstream and upstream direction is relatively small compared to the laminar boundary layer shock wave interaction case. [9] The sonic line in figure 2.15 again shows the shock will not travel all the way to the physical boundary of the airfoil, and in most cases not interfere with for example the (inner) viscous sub layer of the boundary layer, also for stronger shocks. In transonic conditions, the fact that the region behind the shock is subsonic, allows for pressure fluctuations that occur downstream, to travel and influence the shock strength and location, creating an unsteady oscillation shock, which causes the problems this thesis work addresses.

Shock wave and turbulent boundary layer interactions are an important source of drag and can cause unsteady separation of the boundary layer, leading to increased aerodynamic drag, heat-fluxes and fluctuating pressure loads which can lead to vibrations and extensive stressing of the airframe and structure. The influence of an increasing Reynolds number on the shockwave position and buffet onset boundary is shown in qualitative way in figure 2.16a and 2.16b.

Critical Pressure Rise for Separation

Donaldson and Lange [10] have correlated the pressure rise required for separation as a function of the Reynolds number, shown in figure 2.18. In this figure, the pressure rise is defined in a way that can be seen on the middle and right in 2.17b and 2.17c for a respectively laminar and turbulent boundary layer. The schematic flow pattern is in accordance with figure 2.14b. Presenting this situation in a schematic manner, indication point A and B between which we consider the pressure rise, this results in the figure on the left in figure 2.17a. This could be very useful when determining the point of separation, when we can compute a certain pressure rise due to a shock, which occurs at a certain position at a certain Mach number, and introduces the buffet onset at transonic speed.

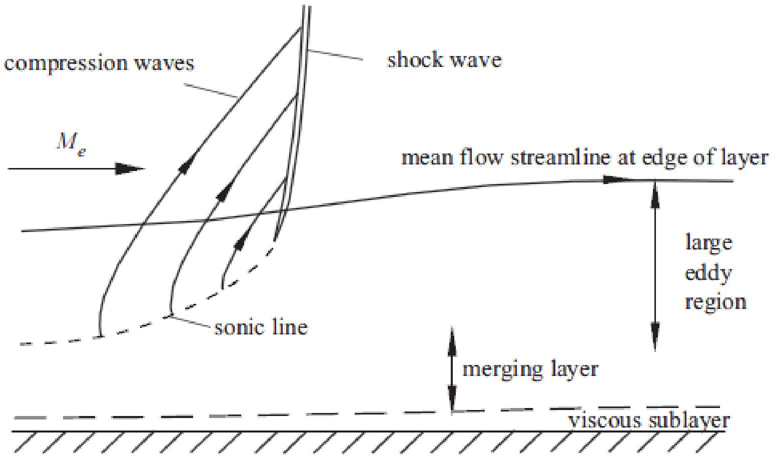

Figure 2.15: Detailed representation of a weak shock-wave boundary-layer interaction for turbulent flow [4]

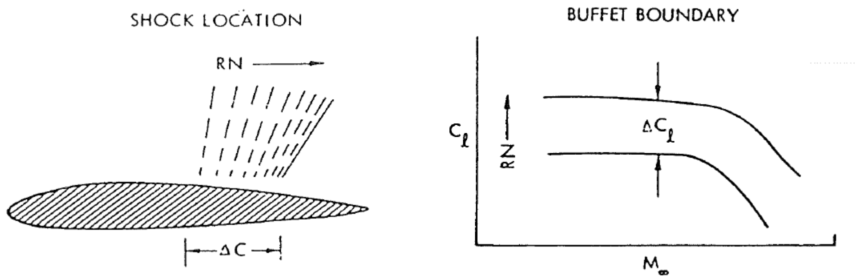

(a) Scale effect on shock wave position

(b) Scale effect on shock-induced boundary layer separation

Figure 2.16: Effect of Reynolds number on shock wave position and buffet onset [5]

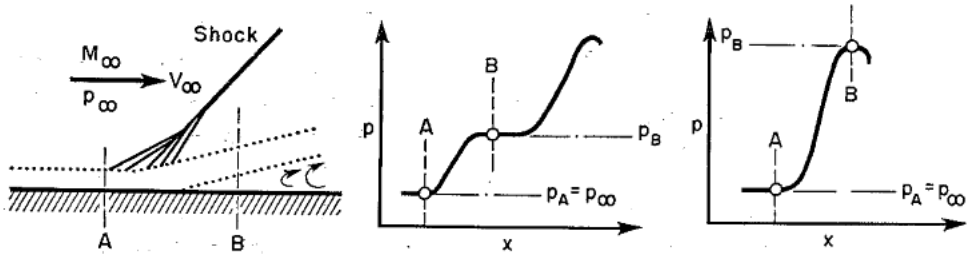

(a) Flow Sketch

(b) Laminar Boundary Layer

(c) Turbulent Boundary Layer

Figure 2.17: Schematic sketch and pressure rise definition [9]

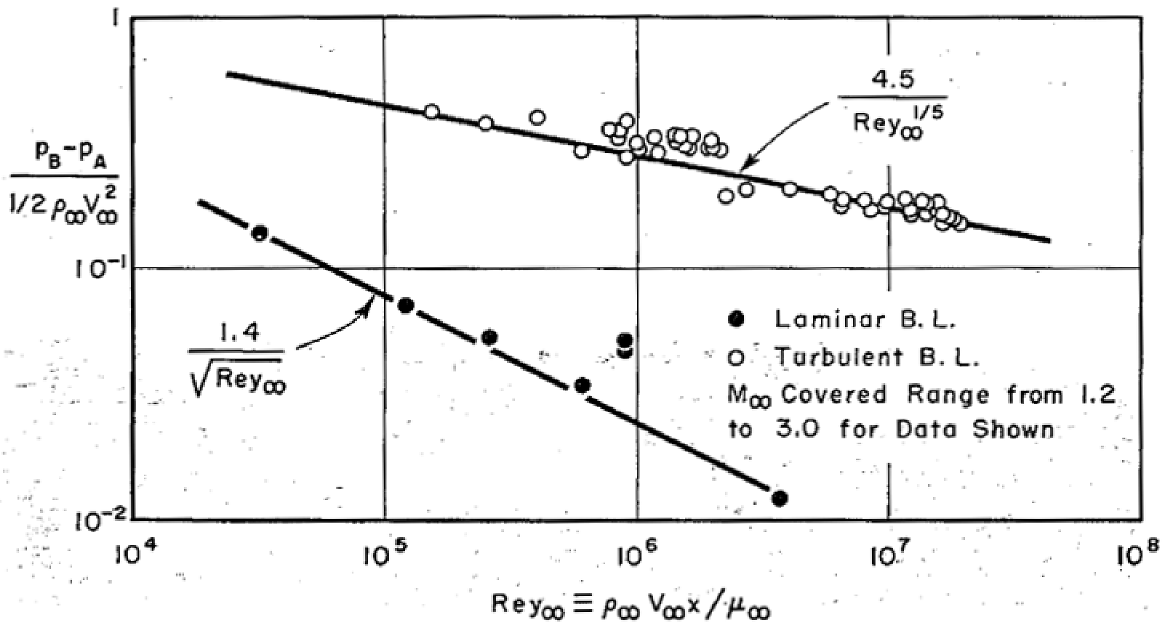

Figure 2.18: Pressure rise across a shock required to separate boundary layer [10]

2.1.7 Limiting Shock Wave Mach Number

In a paper published in 1964 by Laitone [19] the conclusion is drawn that in case of air, the shock on a convex profile that can terminate the local supersonic region can have a maximum Mach number of $M_s = 1.483$ in front of the shock, and the local supersonic flow over a thin convex profile (in isentropic flow) is limited to $M^* = \sqrt{2}$. In other words, velocities greater than the limiting value cannot produce a strong continuous shock that would reverse the streamline orientation and curvature to become straight downstream of the shock. It is so to say the maximum static pressure recovery through a normal shock for any given stagnation pressure. This means no stronger normal shock can exist, since a higher Mach number further downstream a shock would result in a lower static pressure and therefore allow the subsonic free stream static pressure (which is higher) to push the shock wave upstream until that point of maximum static pressure. This velocity limitation is based on the fact that pressure signals cannot travel sufficiently upstream. For an extensive mathematical proof, and derivation of the isentropic relations and shock wave (or jump) conditions involved, see [19].

These findings are rather dated as they originate from research done in the 1960's but form a good basis for understanding the problems with potential flow theory at higher Mach numbers. As described above, Laitone derived a condition for a limiting velocity expected to occur over an airfoil at transonic speeds. It is the ratio of static pressure behind the shock and the stagnation pressure ahead of the shock that is called Laitone's pressure ratio [13] One could see this as some kind of natural limiting phenomena or stability criteria, which results in a maximum Mach number. Since shock wave position and strength directly relate to buffet onset prediction, this is an important and useful conclusion.

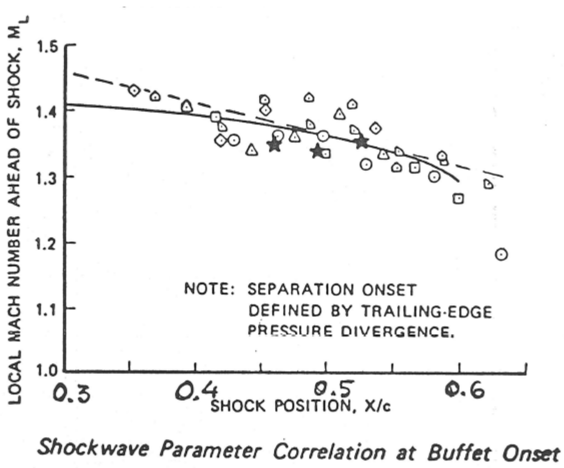

Figure 2.19: Local Mach number ahead of shock wave as a function of shock position [5]

Besides the separation criterion which relies on the magnitude of the pressure jump in combination with the Reynolds number at the position of the shock, one could also use a local Mach number separation criteria in determining buffet onset. Figure 2.19 shows the local Mach number and chord-wise position of the shock wave to produce buffet. The dotted line serves as a function for one of the separation criteria used.

2.1.8 Buffet Detection

Detecting buffet in during flight tests or wind tunnel experiments can be done by wake measurements and by means of pressure tabs along the profile to determine highly loaded sections with a low pressure, or a sudden pressure jump. Another method to detect buffet is measuring the oscillations in the root bending moment. In the latter case, the buffet onset is defined as the lift coefficient for which the root mean square (RMS) of the root bending moment exceeds a certain threshold value [20]. Different methods for detecting buffet are listed below, and can be detected during flight test or wind tunnel experiments.

- Trailing edge pressure deviation
- Local lift curve slope reduction
- Unstable pitch break
- Wing wake width at trailing edge
- Supersonic Mach number downstream of a shock
- Accelerometer recordings
- Axial force deviation

These methods will not be discussed in detail, but illustrate there are several different options for detecting buffet in an experimental setup.

2.1.9 Buffet Operational Regulations

The buffet margin or onset boundary defines the extend of maneuver capability of the aircraft during flight, so it is a flight envelope boundary, or operational limitation. Operational regulations indicate a margin of $0.30g$ in smooth air, which is equivalent to 40 degree bank angle while maintaining level flight [1]. This exceeds the normal flight operations, where a maximum bank angle of 30 degree is reached. One could say that the main design issue or goal is to ensure that during flight the climb and maneuver capabilities are not too much limited by the transonic buffet characteristics. A mismatch between the maximum operating Mach number and the high speed buffet onset Mach number in a way that when the maximum operation Mach number exceeds the buffet onset Mach number, the performance of the aircraft is reduced significantly. If on the other hand the maximum operating Mach number is higher than the buffet onset Mach number, there is nothing to worry about from a buffet point of view. From this perspective, one could say a good design requirement is to keep the maximum operating Mach number close to the high speed buffet onset Mach number in design condition, the lift coefficient at the top of the climb, or at least not overly limited by the buffet onset Mach number, during an important flight phase, for example during cruise.

In symmetric horizontal flight the buffet onset boundary determines the operational ceiling of the airplane. This can be seen in Equation 2.14. In this equation, $\frac{W}{S}$ is constant and the pressure p is a function of the flight altitude in horizontal symmetric flight ($n = 1$). At a certain altitude, where the pressure is constant, a certain Mach number and lift coefficient are required to maintain leveled flight. With increasing altitude, and thus decreasing pressure, the Mach number or lift coefficient need to be increased, until the buffet onset is reached. The resulting diagram is shown in Figure 2.20. The kink in the buffet onset boundary line is called the coffin corner [11].

$$\frac{n \cdot W}{S} = \gamma \frac{1}{2} p M^2 C_L \tag{2.14}$$

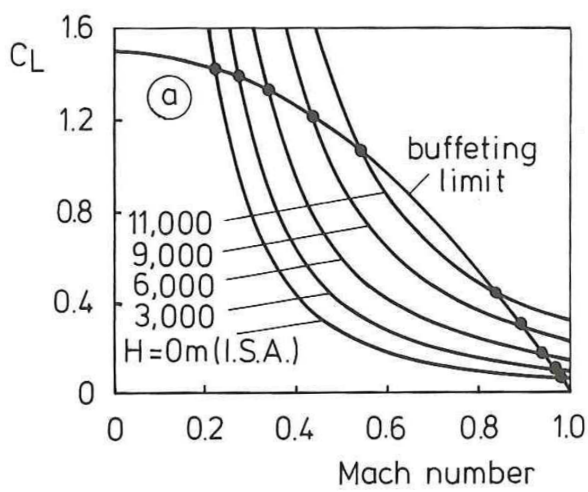

Figure 2.20: Buffet onset boundary and lines of constant altitude [11]

2.1.10 Buffet Cure

To cure buffet, or at least postpone it to extend the operation envelope of the aircraft, there are some methods currently under investigation. One way to control and (partially) cure or postpone the buffet onset is buffet control by means of mechanical an fluidic vortex generators [21]. Experiments have shown that both mechanical and fluidic vortex generators can suppress the flow separation.

A paper from Blinde [22] addresses the effect of very small (micro) ramps as vortex generators in the boundary layer. Different techniques are used to investigate the effects of so these called micro-ramp sub-boundary layer vortex generators. These micro-ramps are small vortex generators, with a height of one fifth the boundary layer thickness. These structures causes a more abrupt pressure rise and induces a pronounced spanwise variation of the flow properties and the probability of reversed-flow occurrence is decreased significantly. They stabilize the shock motion by reducing the length of its motion by about 20% which could be very beneficial for the buffet characteristics.

2.2 Buffet Prediction

To predict buffet one has to start with approximating the transonic flow over the wing. This section will introduce the fundamental equations that describe this flow. Various methods for predicting buffet will be discussed, varying from numerical methods to approximate the fundamental flow equations, to (semi) empirical buffet prediction methods. The previous section, containing information on pressure jumps, shock waves, viscous effects and the boundary layer supply a good understanding of the different aspects involved in predicting buffet onset. This is essential with respect to selecting a method to create the model that will be used in this thesis research. At the end of this section an overview of the different prediction methods will be given, and a conclusion and trade-off will be made.

2.2.1 Fundamental Equations

The fundamental equations are the starting point for describing the flow over the airfoil under investigation. In order to accurately predict buffet, the flow over the airfoil has to be predicted in a correct manner with the use of a numerical method, approximating these fundamental equations. The three equations used to describe the flow, are based on an Euler-like approach, where a fixed control volume is considered through which the air passes and over which the principles below can be applied. [4] This so called control volume can remain fixed in space or can move with the fluid. The Navier-Stokes equations are based on the assumption that the fluid is not made up of discrete particles but rather a continuous substance. Another necessary assumption is that all the parameters of interest like pressure, velocity, density and temperature are differentiable.

The equations are derived from the basic principles of conservation of mass, momentum, and energy. The start of these three conservation laws is the Reynolds transport theorem, an integral relation stating that the sum of the changes of some property defined over a control volume Ω must be equal to what is lost or gained through the boundaries of the volume plus what is lost or produced by sources and sinks inside the control volume [16]. The following derivations are based on a technical report on the governing equations in transonic flow by Roelof Vos [4].

Conservation of Mass

The first fundamental equation is the law of conservation of mass for a fluid (air) passing through a control volume Ω. This continuity equation is as follows:

$$\frac{\partial \rho}{\partial t} + \nabla \cdot (\rho V) = 0 \tag{2.15}$$

In which ρ is the mass density and V is the velocity. This equation generally accompanies the NavierStokes equation. When changing to the substantial-derivative notation [4], this equation reads:

$$\frac{D\rho}{Dt} + \rho\,(\nabla \cdot V) \tag{2.16}$$

When steady, incompressible flow is considered, ρ can be assumed to be constant the following equation (which is in fact a statement of the conservation of volume) holds:

$$\nabla \cdot V = 0 \tag{2.17}$$

However, since a flow is considered to be compressible if its change in density with respect to pressure is non-zero along a streamline, this can only be done in the case where $M_\infty < 0.3$. This assumption is not valid for transonic flows, in which changes in density must be considered.

Momentum Equation

The second conservation law is the conservation of momentum. Again, considering a control volume Ω, Newton's second law for air passing this control volume, when writing momentum as ρv, gives the following equation:

$$\frac{\partial}{\partial t}(\rho V) + \nabla \cdot \rho V V + Q = 0 \tag{2.18}$$

In which Q represents the sources and sinks in the control volume Ω. Without giving a detailed derivation, the following Navier-Stokes equation yields:

$$\rho \frac{DV}{Dt} = \rho f - \nabla p + \frac{\partial}{\partial x_j} + \tau_{ij} \tag{2.19}$$

In which τ_{ij} is called the viscous stress tensor, which is a function of the velocity component cross products.

Energy Equation

The third and last conservation law used in the fundamental equations is the conservation of energy. Although energy can be converted from one form to another, the total energy in a given system remains constant. Without giving a detailed derivation, the following energy equation yields:

$$\rho\frac{Dh}{Dt} = \frac{Dp}{Dt} + \nabla \cdot (k\nabla T) + \Phi \tag{2.20}$$

In which h is enthalpy (a measure of the total energy of a thermodynamic system), k is the thermal conductivity of the fluid, T is temperature, and Φ is the viscous dissipation function. The viscous dissipation function, in other words, governs the rate at which mechanical energy of the flow is converted to heat. The expression on the left side is a material derivative. The term is always positive since, according to the second law of thermodynamics, viscosity cannot add energy to the control volume. [4]

Equation of State

The ideal gas law or another equation of state is often used together with these equations to form a system to solve for the unknown variables. According to the state principle of thermodynamics, the local thermodynamic state is determined by any two independent state variables. Considering a perfect gas (which implies all intermolecular forces are assumed negligible) the gas equation of state reads as can be seen in equation 2.2.1.

$$p = \rho RT \tag{2.21}$$

In transonic flow it is assumed that the gas is calorically perfect and that consequently constant specific heat values can be defined. The following relations hold between the constant-volume-specific-heat constant, c_v, the constant pressure specific heat constant, c_p, the gas constant, R, and the ratio of specific heats, γ.

$$e = c_v T \quad h = c_p T \quad \gamma = \tfrac{c_p}{c_v} \tag{2.22}$$

With the constant-pressure and constant-volume specific-heat constants defined as can be seen in equation 2.2.1:

$$c_p = \tfrac{R}{\gamma - 1} \quad c_v = \tfrac{\gamma R}{\gamma - 1} \tag{2.23}$$

Using the relations above, the temperature and pressure can now be defined in terms of the variables e and ρ. This results in the relations shown in equation 2.2.1.

$$p = (\gamma - 1)\,\rho e \quad T = \tfrac{(\gamma - 1)e}{R} \tag{2.24}$$

Crocco's theorem

The vorticity can be related to the entropy according to Crocco's equation (which can be derived from the first and second laws of thermodynamics) as can be seen in equation 2.25.

$$\frac{\partial V}{\partial t} - V \times \zeta = T\nabla s - \nabla\left(\frac{V^2}{2}\right) \tag{2.25}$$

In which the fluid vorticity is $\zeta = \nabla \times V$. Crocco's equation is useful, because it states that whenever an enthalpy or entropy gradient is present in the flow, it must be rotational. This is particularly important for transonic flow which is considered in this thesis research, since a shockwave often terminates a supersonic portion, and a shock wave means entropy gradient, which means rotation is introduced in the flow. From the second law of thermodynamics it is known that there is an entropy discontinuity across the shockwave, which means the flow cannot be assumed irrotational [4].

2.2.2 Numerical Prediction Methods

Now the fundamental equations are known, this paragraph addresses the different ways to approximate these equations. One way to do this, is with the help of numerical schemes. Every numerical model has its accuracy, computation time, error and other characteristics. If a numerical scheme approximation is compared to the set of Navier-Stokes equations, it becomes clear theory has the advantage that the fundamental parameters can be immediately identified and the effect of varying a certain parameter can be investigated. In order to obtain very accurate solutions using a numerical scheme, either a very simple flow has to be chosen, or approximations to the full flow problem have to be used. The trick is to use an efficient scheme, that accurately approximates the flow case under investigation, without a computational time that is too high.

Using numerical models in Computational Fluid Dynamics (CFD) allows for solving the mathematical models up to the desired accuracy without the limitation that only simple conventional wing geometries can be investigated. Changes in the physical model or the shape of the wing under consideration are relatively easy to perform. Furthermore, it is quite easy to switch terms in the fundamental equations on and off in order to study the influence of that particular term on the ultimate solution, if the numerical model used is chosen correctly [23].

The quality of the results obtained with a certain numerical scheme will always depend on the ability to model the physics appropriately. In addition, the solution of the numerical simulation will also depend on any numerical parameters introduced in the model such as the time step, grid size and so on. This thesis will not address subjects like grid generation, grid size and so on, since this is beyond the scope of this research and off the shelf programs are used.

Two important concepts in the buffet onset prediction tool, will be verification and validation. Since there is data available on the buffet onset of a number of (conventional) wing geometries, this forms a good basis for validating and verifying the model developed, although there is buffet onset data of various aircraft available, there is still a need for the exact geometry and airfoils of this reference data to be able to verify the model. If this verification is done successfully with known buffet onset and wing geometry data, conclusion can be made on its accuracy, functionality and applicability on less conventional wing geometries[1].

The basis of a numerical method is a mathematical model which describes the flow to a certain degree of detail. Important decisions with respect to certain assumptions and simplifications on the flow conditions will have to be made. The amount of detail desired will have consequences for the complexity of the code and the amount of computer power and time required to obtain significant and usable results. Since a tool for the conceptual (initial) design phase is the goal of this work, this computational time aspect is of great importance. Most probably a trade-off will have to be made in fast results on one side, and detailed results with small error bandwidth on the other side. Important question to ask before choosing a numerical model are: 'What are the in-, and outputs of the tool? What parameters are important? Are viscous effects to be accounted for? How is the boundary layer modeled, and is there a separate turbulence model needed? Are there shocks that introduce rotation in the flow? Does this change the results, and if so, to which extend? How do the models investigated handle this? Can models be combined or modified in a smart way to improve their applicability and accuracy? Since the subject of this thesis focuses on the transonic regime, one of the challenging aspects is to find a method that results in less computational time, but has more detailed results that a simple potential flow code, which as described in the next few paragraphs has problems coping with viscous phenomena and boundary layer shock wave interactions and more.

Before addressing the various different approximation methods available in detail, one can see these methods in the following descending order of complexity:

- Full Navier-Stokes equations
- Reynolds-Averaged-Navier-Stokes equations
- Euler equations
- Potential flow

Starting from the Naviers-Stokes equations, one of the best approximations of the fundamental equations is the Reynolds-Averaged-Navier-Stokes equations (RANS). Neglecting viscosity results in the Euler method, and when the flow is considered to be irrotational, one can consider the potential flow method. In the remainder of this section, these different models will be discussed in detail.

It is important to make a clear representation of the inputs and outputs expected and needed for the buffet prediction tool, and with that information take a look at the various

[1] In this report although, one could speak of more a demonstration test case than validation, since the developed tool will be tested on the Fokker 100 wing only.

parameters involved and choose a numerical method to approximate the required information and flow characteristics. At the end of Chapter 2, an overview is given of the pros and cons of each numerical method with respect to issues like viscous effects, rotation, boundary layer incorporation and turbulence and separated flow. With the help of this, a trade-off can be made, following a conclusion on which model to be used in the rest of this thesis research.

Boundary Layer Theories and Models

The concept of boundary layer flow and why it is important in computing a detailed pressure distribution over a given airfoil is discussed in the previous section. The accuracy of pressure distribution computations of attached flow over the whole aircraft and all of its components is improved when boundary layer effects are incorporated. The question remains, how good these models are. The laminar boundary layer theory is well established and documented. The turbulent boundary layer theory on the other hand, is based on experimental data for the most part. furthermore transition and the accompanying transition bubble is not yet fully understood. Turbulent separation at the trailing edge, which might be the case in this thesis work because we are effectively dealing with trailing edge separation at transonic speeds, can be handled reasonably well in 2-dimensional flow [5]. On the field of shockwave-boundary layer interaction, the conclusion can be made that only relatively weak shocks can be treated and, as will become clear in the next paragraph, this introduces significant errors in the pressure distribution calculations.

Reynolds-Averaged Navier-Stokes Equations

One of the best, but time consuming, approximations of the fundamental equations is the Reynolds-averaged Navier-Stokes approximation. The RANS equations are time-averaged equations of motion for fluid flow such as air. The idea behind the equations is Reynolds decomposition, in which the parameters are decomposed into time-averaged and fluctuating quantities. The RANS equations are primarily used to describe turbulent flows. These equations can be used with approximations based on knowledge of the properties of flow turbulence to give approximate time-averaged solutions to the Navier Stokes equations.

Various models have been developed to extract the average motion of the flow when turbulent. One of the most commonly used approximation techniques is Reynolds averaging. As seen in the previous sections of this chapter, the interaction between the turbulent boundary layer and the shock wave is an important characteristic of transonic flow. It has a pronounced effect on the position of the shock wave, which, in turn, is a dominant factor for the pressure distribution over the airfoil.

Compressible Time-Averaged Flow Parameters The Reynolds-averaging procedure mentioned above is based on the method of splitting the flow parameters such as pressure, velocity, temperature, density and enthalpy into a time-averaged part and a fluctuating part. In Reynolds averaged compressible flow, it is convenient to apply a mass-weighted averaging in addition to the time averaging. Mass-averaging the flow parameters first can be done by multiplying the parameters by the density, averaging this product, and dividing by the average density, as is shown in equations 2.2.2, 2.2.2 and 2.2.2.

$$\tilde{u} = \frac{\overline{\rho u}}{\bar{\rho}} \quad \tilde{v} = \frac{\overline{\rho v}}{\bar{\rho}} \quad \tilde{w} = \frac{\overline{\rho w}}{\bar{\rho}} \quad \tilde{h} = \frac{\overline{\rho h}}{\bar{\rho}} \quad \tilde{T} = \frac{\overline{\rho T}}{\bar{\rho}} \quad \tilde{H} = \frac{\overline{\rho H}}{\bar{\rho}} \tag{2.26}$$

$$u = \tilde{u} + u'' \quad v = \tilde{v} + v'' \quad w = \tilde{w} + w'' \quad \rho = \tilde{\rho} + \rho'' \tag{2.27}$$

$$p = \tilde{p} + p' \quad h = \tilde{h} + h'' \quad T = \tilde{T} + T'' \quad H = \tilde{H} + H'' \tag{2.28}$$

In which fluctuating terms (the prime terms) are the time dependent terms that become zero when they are time averaged. In other words, they fluctuate above and under the averaged (over bar) terms equally over time. The averages of the doubly primed (fluctuating) parameters are non-zero. Instead the time average of the doubly primed fluctuations multiplied by the density equals zero. [4]

When the modified parameters above are substituted into the fundamental equations mentioned in the previous paragraph, and in addition, each of the equations is time averaged, the result yields a set of equations that have averaged fluctuating terms. When neglecting the fluctuating velocity component, various terms in the equations of motion can be dropped yielding a more compact version of these equations results. When examining the three conservation laws again, with these time-averaged parameters, this results in the following modified conservation laws.

Averaged Conservation of Mass For conservation of mass, the following continuity equation yields:

$$\frac{\partial \bar{\rho}}{\partial t} + \frac{\partial}{\partial x_j} \left(\bar{\rho} \tilde{u}_j = 0 \right) \tag{2.29}$$

Averaged Momentum Equation For conservation of momentum, starting from the Navier-Stokes equation, the following Reynolds-averaged equation in mass-weighed variables yield:

$$\frac{\partial}{\partial t} \left(\bar{\rho} \tilde{u}_j \right) + \frac{\partial}{\partial x_j} \left(\bar{\rho} \tilde{u}_i \tilde{u}_i \right) = -\frac{\partial \bar{p}}{\partial x_i} + \frac{\partial}{\partial x_i} \left(\bar{\tau_{ij}} - \overline{\rho u_i'' u_j''} \right) \tag{2.30}$$

In this equation the viscous terms with doubly primed fluctuations are often neglected based on their magnitude compared to the mass-averaged variables, which simplifies the equation to some extent.

Averaged Energy Equation For conservation of energy, when substituting the mass-weighted variables and eliminating the terms that go to zero yields the following Reynolds energy equation in mass-weighed variables:

$$\frac{\partial}{\partial t}\left(\bar{\rho}\tilde{H}\right) + \frac{\partial}{\partial x_j}\left(\bar{\rho}\tilde{u}_j\tilde{H} + \overline{\rho u_j'' H_j''} - k\frac{\partial \bar{T}}{\partial x_j}\right) = \frac{\partial \bar{p}}{\partial t} + \frac{\partial}{\partial x_j}\left(\tilde{u}_i\tilde{\tau_{ij}} + \overline{u_i''\tau_{ij}}\right) \tag{2.31}$$

In which τ again is a stress term.

Use of the Reynolds-Averaged Equations In addition to the stress terms, a laminar and turbulent heat flux term can be defined. These new (turbulent) stresses and flux terms that appear in both the Reynolds-averaged momentum and energy equation should be treated as new variables. Therefore, the system becomes a system with more variables than equations, which results in problems when trying to solve the system. Therefore, additional equations are required to solve the flow in a unique way. This is where turbulence models come into play. Since the RANS equation show additional terms with respect to the original Navier-Stokes equations. These fluctuating terms need to be related to the average flow parameters in order to close the RANS equations [4]. This closure of the Reynolds-averaged equations via turbulence models is discussed below.

Turbulence Modeling Several models have been developed to close the RANS equations as mentioned above. Ranging from simple algebraic models to more rigorous models like the $k-\epsilon$ model. It needs to be noted that the only way to verify whether a turbulence model is effective, is by experimental verification. Some different turbulence modeling solutions are [7]:

- Eddy-viscosity modeling: Algebraic models use direct relations between turbulence properties and the local mean flow field
- Second-moment closure: Modeling of individual Reynolds stresses, which implies additional transport equations are used
- Large Eddy Simulation (LES): Partial modeling for small scales
- Direct Numerical Simulation (DNS): Full computation of all scales

The Eddy-viscosity model approximates the Reynolds stress term in equation 2.5 in the following manner as can be seen in equation 2.32. The artificial ν_t is called the Eddy-viscosity.

$$\frac{1}{\rho}\frac{\partial}{\partial y}\left(\overline{u'v'}\right) = \nu_t\frac{\partial u}{\partial y} \tag{2.32}$$

Euler Method

Following the RANS equations, a reduced model of the complete Navier-Stoke equations is the Euler model. By dropping the heat-transfer terms as well as the viscous terms, these equations describe the flow of an inviscid, non-conducting flow of a homogeneous fluid in subsonic and supersonic regimes [23]. Furthermore, it is also assumed that there is no external heat transfer, such that the $\frac{\partial Q}{\partial t}$ term in the energy equation can be dropped. The Euler equations can be used to numerically predict the locations and shapes of shock waves that occur in regions of the flow where the effects of viscosity and heat conduction are neglected, as well as the absence of a boundary layer in the simulation. The Euler equations can significantly reduce the computational time with respect to for example a simulation using the RANS equations. As a shock is being diffused by the viscous boundary layer, which is absent in the Euler solution, this may cause inaccurate shock position prediction or incorrect magnitude of the pressure rise across the shock wave.

Another problem that arises when using the Euler equations, is the fact there is some excess entropy production in the flow field. In other words this means that due to a numerical stability requirement, artificial viscosity is introduced. Two areas where false entropy is produced are ahead of shocks and in areas of steep pressure gradients (i.e. leading edge of the wing). When a shock is present, rotation is introduced in the flow as shown by Crocco's theorem in equation 2.25, which means entropy is introduced. Crocco's theorem relates these flow parameters (velocity, vorticity, and stagnation pressure or entropy) to each other. This entropy may be small, but integrated over a large area might result in significant errors in the wave drag calculation. Some tricks are proposed in literature to limit the amount of false entropy included in the wave drag calculation and to reduce the computation time of the induced drag calculation [23]. This is not of very big importance in this thesis, since the Drag is not investigated in order to predict buffet onset.

Conservation of Mass For conservation of mass, the continuity equation remains the same, since it is neither dependent on the viscosity nor on the heat-transfer coefficient.

Momentum Equation For conservation of momentum, starting from the equation 2.18, the following equation yields when the viscous terms in the momentum equation are dropped:

$$\rho \frac{DV}{Dt} = \rho f - \nabla p \tag{2.33}$$

In which f is the body force per unit mass.

Energy Equation Dropping the viscous and heat-transfer terms in the energy equation 2.20, results in the following expression:

$$\rho \frac{De}{Dt} + p\left(\nabla \cdot V\right) = 0 \tag{2.34}$$

In which e is the internal energy. The energy equation can also be formulated in terms of enthalpy, resulting which would yield the following expression:

$$\rho \frac{Dh}{Dt} = \frac{Dp}{Dt} \tag{2.35}$$

As shown in the previous paragraph on shock waves (in section 2.1), it has to be noted that numerically, a shock wave is represented by a discontinuity in the flow field variables ρ, p and $\mathbf{u}$. These discontinuities may cause numerical instability for certain numerical solution schemes, such as negative density and pressure. [24]

Isentropic Potential Flow Model

Simplifying the fundamental equations even one step further, with respect to the Euler equations, the flow is assumed to be irrotational. Here the isentropic potential flow method comes in to play. The potential flow approximation was the dominate model for transonic aerodynamics for many years [13]. It is still used in many different engineering applications like (conceptual and preliminary) aerodynamic design and analysis. Potential flow methods have also been suggested for use in multidisciplinary design methodology because of the comparatively small computational cost, according to J. Dudley [25].

The traditional formulation of the potential equations is based on the integrated energy equation, mass conservation and the isentropic relations. But there are many ways to formulate the potential equations for a certain flow, for example if one wishes to allow for entropy changes or stream wise momentum conservation [13]. Each different formulation has its accuracy, so it is wise to investigate several different options before applying one in the model that is going to be used in any analyses. The shortcomings of the potential flow formulation for transonic flow will be discussed in the next paragraphs. Without going into too much detail of the math behind several of these approximations, an overview of three important approximations is given by figure 2.21, in which the pressure ratio across a normal shock is simulated with three different potential flow schemes.

A small side step from these general numerical methods is the use of the so called Kutta boundary condition. This condition takes into effect lift and is an empirical boundary condition which is not automatically satisfied. Physically the Kutta Boundary condition is coupled to the boundary layer flow at the trailing edge of the airfoil (essentially it implies aligning the air flow at the trailing edge with the local camber line) and a proper choice for this condition must incorporate the boundary layer when detailed information about the pressure distribution is required [5].

Non-isentropic Potential Flow Model

The full potential flow theory has his shortcomings as became clear in the previous section. Next to a non-isentropic method like the Euler method, one can also alter the full potential flow theory in such a way to remove the isentropic part. The difference between potential (isentropic) jumps and the above mentioned Rankine-Hugoniot jumps becomes clear in an analyses by Laitone [19] and revealed significant differences between

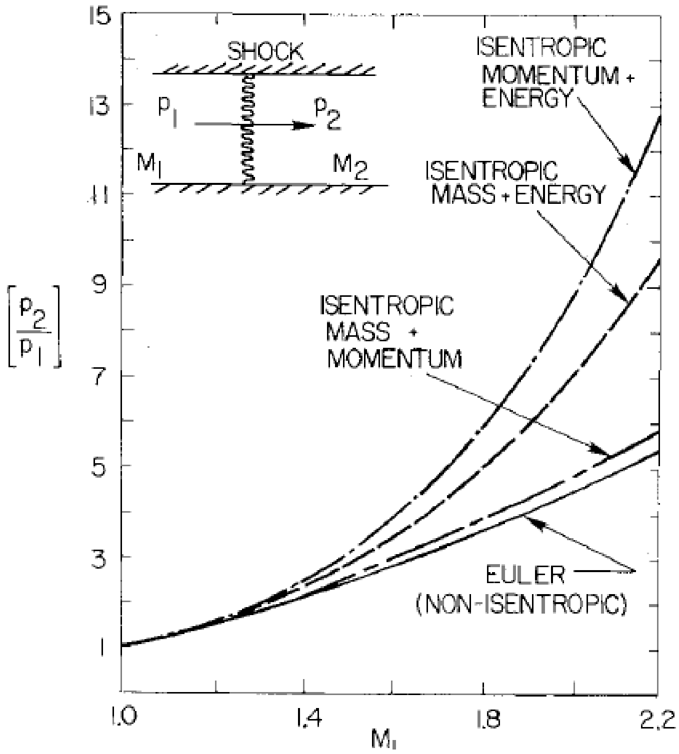

Figure 2.21: Pressure ratio across a normal shock for three different potential flow schemes [12]

the potential and Rankine-Hugoniot jumps as soon as a stronger shock occur. A potential equation for non-isentropic transonic flows can be formulated. This procedure captures these shock waves but retains the simplicity of the traditional potential equation. Also, because Crocco's theorem is not applicable to potential flows, a modified Crocco's theorem valid for potential flows has to be implemented to cope with transonic flows with non-constant shock strengths, which will never be irrotational, irrespective of whether the flow is isentropic or not [13].

When numerical solutions of the potential flow equation started being computed for transonic flows including shocks, it was found in the early eighties that the full potential solutions were seriously in error when shock waves became significantly strong, e.g. when the Mach number in front of the shock reached around $M_s = 1.25$. The result of this research showed that both the strength and the position of the shock were incorrectly predicted using potential flow methods. [13] This result was not completely unexpected, but the magnitude of the error was unexpectedly large. A report [13] on the magnitude of these errors shows the following results, as can be seen in figure 2.22a and 2.22b.

Figures 2.22a and 2.22b show a full potential and Euler approximation of a NACA 0012 airfoil at $M_\infty = 0.8$ and under a zero angle of attack $\alpha = 0°$. There is only a small difference between the results of the Euler and potential equations solution to the pressure distribution over the airfoil. It is worth noticing that the potential flow solution shows a **stronger** shock that is slightly aft of the Euler computation. The influence of the angle

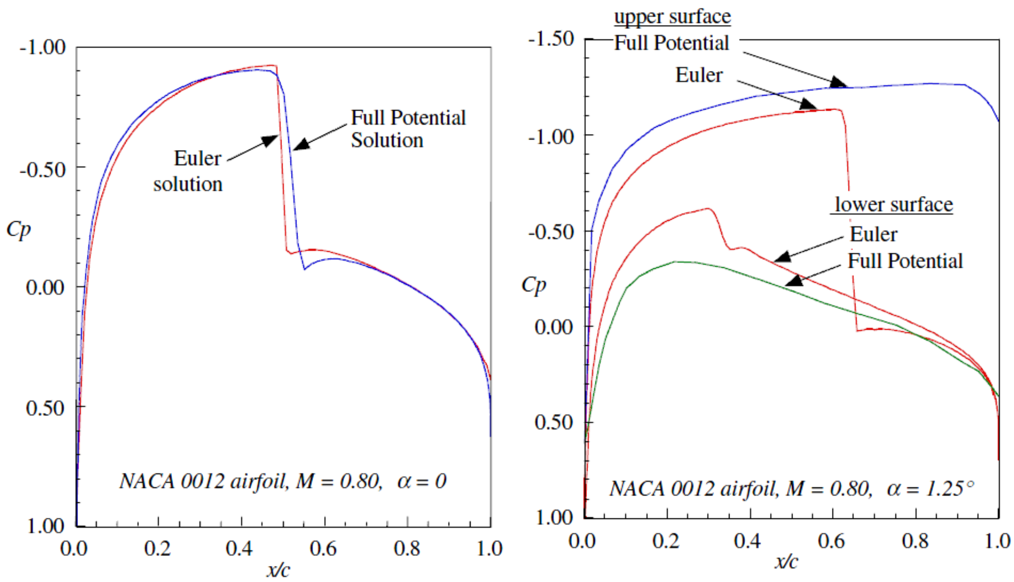

(a) NACA 0012 case 1 (b) NACA 0012 case 2

Figure 2.22: C_p around NACA 0012 airfoil for Euler and full potential model at $M_\infty = 0.8$ [13]

of attack shows an increase in angle of attack to $\alpha = 1.25°$ leads to a stronger shock (on the top side of the airfoil) and a shift further aft of 13% of the chord for the Euler solution, and a much larger shift of the (strong) shock towards the trailing edge. This difference is clearly visible in figure 2.22b. This is a good indication of the large discrepancies that occur between Euler and potential flow results when the shock strength increases.

The difference between non-isentropic potential flow and isentropic (full) potential flow approximation can be seen as follows: Under the potential flow assumption, entropy is held constant across the shock, and mass is conserved while momentum is **not**. Klopfer and Nixon [12] continued research on use of potential flow equations in transonic conditions, and published a paper on non-isentropic potential formulation for transonic flows which resulted in several so called jump formulations which showed that a potential jump which conserved momentum instead of energy was much closer to the actual Rankine-Hugoniot jump condition. It has to be noted that they made changes to the Kutta condition to achieve this result (which can be seen in figure 2.23). At supersonic speeds it was shown that by correcting the isentropic jump at the bow shock, the potential flow equation could even be used to obtain accurate results for a large scale of (strong) shocks with free stream Mach numbers way beyond the transonic regime, as high as $1 < M_\infty < 10$. [26]

A second issue when applying potential flow theory to transonic conditions is the non-uniqueness of the solution. It seemed that the error induced by the shock jump using the potential flow model leads directly to this non-uniqueness problem. But this problem also showed in the Euler equation but analysis by McGratten [27] concluded that it is unlikely that it is due to the isentropic assumption of the potential flow model. His assumption is that the Kutta condition (or its equivalent for the Euler equation) has an equally large influence on this non-uniqueness problem. What does non-uniqueness mean from a practical point of view? Roughly speaking, a non-unique (or weak solution) may contain discontinuities and may not be differentiable. To solve this problem, one can introduce a new criterion on the artificial entropy, as discussed in the beginning of section 2.2.2.

Non-isentropic Potential Formulation for Transonic Flows The isentropic potential formulation can be altered in such a way that the isentropic condition is 'relaxed'. The derivation of the non-isentropic formulation then includes entropy changes. Assuming a normal shock wave, the modifications of the standard potential formulation required to arrive at the non-isentropic potential formulation can be derived. This derivation can be found in a paper by Terry Holst [28] and will not be addressed in detail here, because it is beyond the scope of this thesis.

The results of this non-isentropic potential formulation is shown in figure 2.23. Although this case might be a little extreme because the full potential flow model indicates a shock near the trailing edge of the airfoil, where the Euler code locate the shock at approximately $60-70\%$ of the chord, the non-isentropic potential model is in line with the Euler results. Also the non-isentropic and Euler approximation show a lower side shock, which is not present in the full potential simulation. As a result of this, the lift and drag coefficients are also better approximated with this modified potential model as can be read in the same figure. The isentropic potential analysis is off almost 300% in terms of lift prediction, where the non-insentropic analysis shows only a 5% offset with respect to the Euler prediction [12].

In conclusion it can be said that it is possible to alter the isentropic potential equations in such a way that the isentropic assumption is not a requirement to be able to use a potential flow model. By allowing entropy changes and assuming irrotational flow a potential approximation to the Euler equations can be constructed. Assuming the velocity distribution outside the boundary layer can be accurately calculated, including the shock wave location and its strength, this could be used as an input in a boundary layer model. That way, it could be calculated whether or not there is separation at a certain instance. This would predict the shock induced buffet onset (assuming buffet always starts with separation) and reduce the problem complexity significantly.

Transonic small disturbance equations An intermediate step between Panel Codes and Full Potential codes were codes that used the Transonic Small Disturbance equations.

The assumptions made in the derivation of the transonic small disturbance equations are:

- The body is thin
- The body has a small angle of attack
- The body has a mild camber

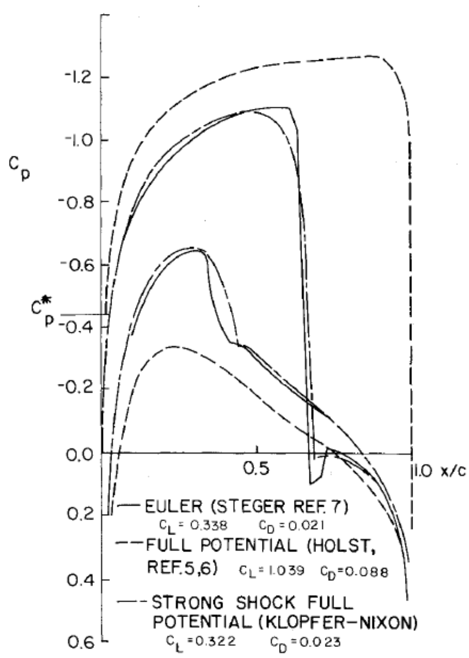

Figure 2.23: C_p around NACA 0012 airfoil at $M_\infty = 0.8$ and $\alpha = 1.25°$ [12]

As a result of this, the body slope $\frac{dy}{dx}$, in a coordinate system attached to the freestream (sometimes also known as the wind tunnel coordinate system) is small. It is also assumed the local flow velocity components u and v are not significantly different from their freestream values.

When the full potential equation is simplified by assuming that perturbation velocities are small and we relate the local speed of sound to the freestream value by making use of the isentropic relations, the small disturbance equation is obtained. This transonic small disturbance equation is still nonlinear, in spite of the approximations that were made to arrive at this equation. It is this nonlinearity that allows for modeling shock waves as was mentioned in section 2.1 of this chapter on shock waves. In subsonic and supersonic flows, for thin airfoils, wings and bodies, the governing equation is linear. [29] When investigating buffet at high lift coefficients, the angle of attack might become larger than the transonic small disturbance code can handle, but literature suggests a range of approximately $\alpha \in [-9°, 9°]$ will be achievable.

2.2.3 Empirical Prediction Methods

Off-course there are other ways to predict buffet than with the help of a numerical approximation of the fundamental equations, for example the (semi) empirical prediction methods. In the field of conceptual design prediction of the buffet envelope an interesting paper was published by Adrien Berard and Askin Isikveren in 2009 [1]. In this paper a methodology that predicts the buffet onset boundary of new transport aircraft wing geometries is discussed. This method identifies some key parameters that determine the buffet onset of a certain wing design, and uses a database of so called 'seed' aircraft to relate a new design to an already existing wing design from its database. It tries to match the new design as closely as possible to one of the database entries (looking at a certain number of parameters) and consecutively identifies modeling functions to account for the offset of the design parameter with respect to the known database entry. One could see these modeling functions as some sort of sensitivity indicators. In other words, what is the result if a certain parameter of the wing design changes by a certain amount.

Without going into too much detail on the exact formulation of these modeling functions, the parameters used in this empirical method are the aspect ratio, taper ratio, camber, maximum thickness-to-chord ratio, chord and the quarter chord sweep angle. Looking at the results of this method, Berard and Isikveren state this semi-empirical method has been shown to be adequately robust and flexible enough to deal with a wide variety of wing designs. For the transport aircraft considered in their research the relative error in prediction was found to be for the majority within the 5.0% region with occasional excursions not exceeding a 9.0% bandwidth. The standard error of estimate for the lift coefficient at 1.0 g buffet onset at a given Mach number was calculated to be 0.0262.

One of the downsides of this method is that if no seed aircraft are available to match the design at hand, or a match is made which has relatively large offset with the parameters of wings in the database, the offset in the end result (the buffet onset boundary: M_∞ vs C_L diagram) becomes large. This is even more the case when designing unconventional wing geometries, since it is likely there is no reference data available in most cases. In other words, there is a lack of seed aircraft.

2.2.4 Method Selection

After reviewing the various numerical and empirical prediction methods in the previous sections a trade-off has to be made. The previous sections have presented the fundamental equations for describing transonic flow, being the conservation of mass, momentum and energy. These equations need to be modified in order to simplify the analysis and enable an efficient approximation of the flow. There are several methods that can be used to approximations the flow.

The approximation with least complexity is the isentropic potential flow model. The problem with this method is it cannot cope with viscous effects, and does not account for rotation or entropy in the flow. Since shock waves produce rotation and entropy, the isentropic potential flow model cannot predict shock wave position or strength of the pressure jump, which is essential for predicting buffet.

In the Euler equations, rotation can be accounted for, but still no viscous effects can be incorporated. Therefore a boundary-layer model is needed in this approximation. The drawback of this approach lies in the viscid and inviscid calculations which have to converge in order to compute a solution. Furthermore, because of the absence of viscosity, the shock-wave boundary-layer interaction is not accounted for by the Euler equations. Instead, the displacement thickness is added to the contour of the airfoil, and the flow is solved again for the new resulting contour. The flow in and out of the boundary layer are solved separately, hence the need for convergence between the viscid and inviscid solution.

When comparing the Euler model with the full (isentropic) potential flow model, the difference becomes visible in the figures 2.22a and 2.22b. When weak shocks occur, the two methods show little difference in predicting the pressure jump over the shock, but at a certain moderate and strong shocks the potential flow theory seems to fail significantly in approximating the pressure over the airfoil correctly. Looking at previously mentioned figures, one could say there is a sort of cut-off local Mach number around $M_\infty = 1.2 - 1.3$. From this point on, the results seem to deteriorate quite suddenly as the shock becomes stronger as can be seen in figure 2.24a and 2.24b. This figure shows the upstream Mach number M_1 versus the downstream Mach number M_2 after the shock for isentropic potential flow and Rankine-Hugoniot shock jump.

From figures 2.24a and 2.24b it becomes clear that the potential flow jump smoothly diverges from the 'real' Rankine-Hugoniot jump condition from $M_1 = 1$ and on. Under M_1 the potential flow shock jump can be assumed to be in agreement with the real jump condition, looking at its asymptotical behavior in the region $0 < M_1 < 1$. Interesting to see in this figure is that the potential flow shock jump is larger than the Rankine-Hugoniot jump. In comparison to the first two figures 2.22a and 2.22b this M_1 versus M_2 graph does not show a sudden breakdown of the potential flow method. The difference between the potential flow and Euler method at e.g. $M_1 = 1.4$ and $M_1 = 1.6$ is not that large. If a similar graph is constructed for the upstream Mach number M_1 versus the pressure ratio $\frac{p_2}{p_1}$ the same development for the error of the potential flow calculation with respect to the Rankine-Hugoniot pressure jump can be seen. This second figure 2.25 is consistent with the Mach number differences in the previous graph. On the other hand, when the isentropic potential flow equations are altered, the non-isentropic potential flow equations have shown to produce results similar to the Euler method, and could therefore be an interesting option compared to the Euler method, when looking from a computational time perspective.

In conclusion, when using inviscid methods like potential flow, because of their execution speed and easy implementation in the initial design phase, one should keep the effect illustrated above in mind when interpreting the results from this analyses. This research reveals a fundamental difference between the potential flow and Euler models for approximating the flow over an airfoil, and although the difference between the Rankine-Hugoniot and isentropic Mach jumps is smooth, and does not show an abrupt change with increasing Mach number $M_1 > 1$, the Laitone pressure ratio described above does show a major change.

Looking at the paragraph on limiting shock wave Mach number (Laitone's analysis) determining the position of the shockwave on the top side of the airfoil, and determine the local Mach number in front of this shock (the sonic region of the flow) when trailing edge separation occurs, can be an excellent starting point for a relatively simple transonic buffet prediction tool. With this information, a second simulation can change the free stream Mach number and lift coefficient (or angle of attack) until the earlier determined local Mach number in front of the shock wave is achieved. This way the buffet onset lift coefficient as a function of the free stream Mach number can be constructed. Interesting to investigate would be how (and if) this condition described by Laitone also holds

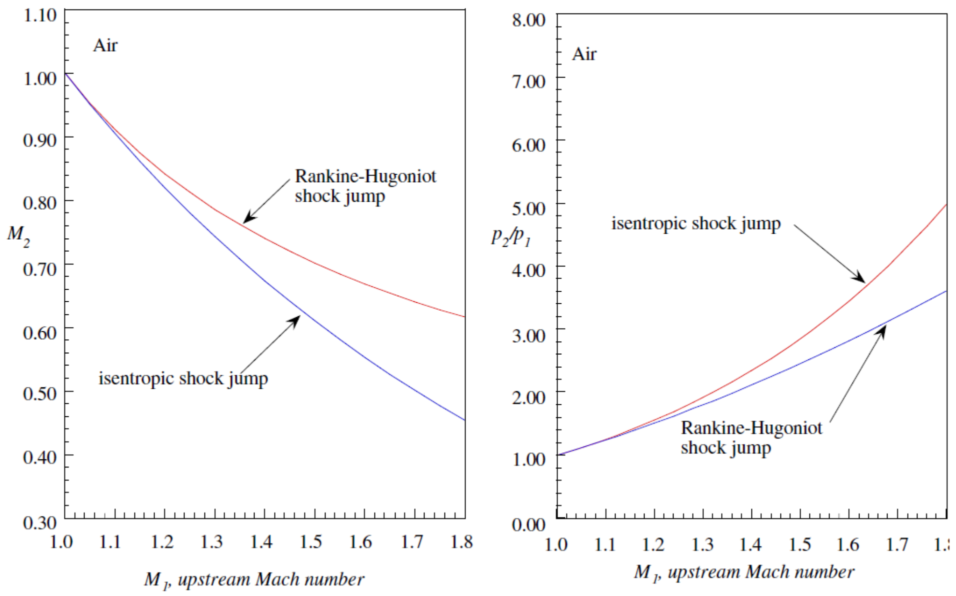

Figure 2.24: Shock jump for Euler and full potential model on NACA 0012 airfoil at $M_\infty = 0.8$ [13]

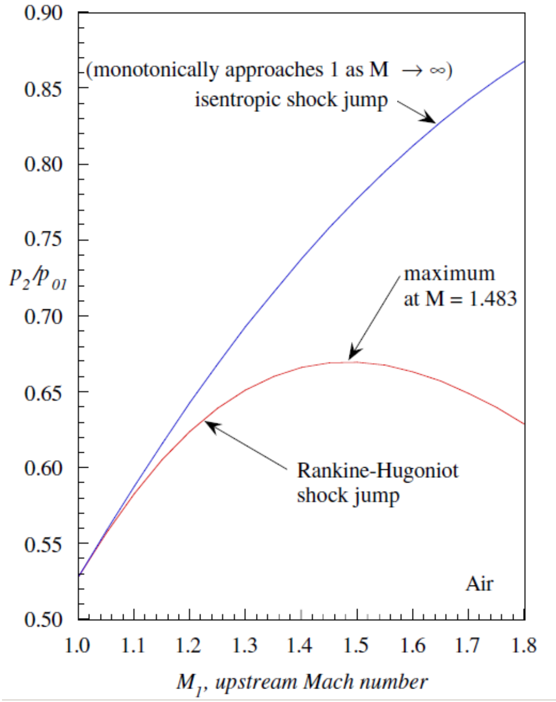

Figure 2.25: Pressure ratio comparison over NACA 0012 airfoil at $M_\infty = 0.8$ and $\alpha = 1.25°$ [13]

for unconventional wing geometries like blended wing bodies and what the influence of leading edge and trailing edge devices like slats, flaps, vortex generators and gaps. In other words, is this limiting shock wave Mach number also applicable in case LE or TE (high lift) devices are present? In addition, the calculation time and implementation are criteria to which this approach should be weighted in a trade-off.

Applying only time and mass averaging to the fundamental equations, the most accurate and most complex approximation of the Navier-Stokes equations results, being the Reynolds-averaged Navier-Stokes equations. This system of equations considers viscous forces to be present in the flow and are therefore more realistic than the Euler equations in combination with a boundary layer model. However, the fluctuating terms that are introduced require a turbulence model to close the set of equations. It could be possible to divide the domain of the transonic flow into subdomains where viscous forces are dominant (e.g. boundary layer and wake). In these domains the Reynolds-averaged equations can be employed while in the remaining flow field the Euler equations can be employed. This could simplify the overall computational complexity, and save computation time. Downside of the use of the RANS model, is the need for a (sometimes very complex) turbulence model.

Last but not least, next to all the numerical buffet prediction methods, the section on empirical buffet prediction shows an interesting method described by Isikveren et al [1]. This method indicates it might be possible to create a dynamic database of virtual 'seed' aircraft with a certain numerical method, so when a new design is made, a close match is more or less 'guaranteed' which will provide a better end result, the M_∞ vs C_L buffet onset diagram. Furthermore, this kind of database would be continuously updated and improved, when a new design is made. For example, one could start by implementing all NACA airfoils together with some supercritical airfoils, but this would still not solve the problem with the unconventional wing geometries.

It is still hard to say at this moment which method is the one to choose, only based on literature. Therefore, several different approaches have been configured combining the different numerical and (semi) empirical methods mentioned in this chapter. An approach to determine the buffet onset boundary of a given wing-fuselage combination could be:

1. Determine the highest loaded section $\eta_{\max}$ in spanwise sense with a simple vortex lattice or panel code
2. Determine 2-dimensional airfoil by making a cut at this position
3. Determine location and strength of the shock wave with non-isentropic potential flow model or other 2-dimensional code
4. Use a separation criteria to determine if the boundary layer is separated
5. Iterate to construct a Mach number vs. angle of attack buffet onset boundary for the 2-dimensional airfoil
6. Translate from 2-dimensional buffet onset to 3-dimensional buffet onset boundary

In other words, first the highest loaded section in spanwise direction is determined. For this step a low complexity and relatively simple panel code will be sufficient. From a computational time point of view, this is not expected to be the most critical time consuming stage. After that, the airfoil at that spanwise location needs to be constructed. To do this, a cut is needed to acquire the 2-dimensional airfoil to be investigated. One of the items still under discussion is way the cut is to be made. One can go from the 3-dimensional wing to the 2-dimensional airfoil by for example cutting perpendicular to the chord, which does not have to be in direction of the free stream velocity. The third step, is to investigate the airfoil under transonic flow conditions, with the use of for example the non-isentropic potential flow model to determine the location of the shock wave, and the value of the pressure jump (the strength of the shock). The non-isentropic potential flow model looks promising in terms of accuracy with respect to shock wave location and magnitude, as well as computational time.

At this stage, only the pressure distribution and local Mach number distribution over the airfoil will be known. So the use of a separation criterion as mentioned in figure 2.18 is needed to test whether the associated pressure jump or local Mach number at certain flow conditions is large enough to separate the boundary layer. This has to be iterated over various angle of attack and Mach number combinations, to construct a Mach number vs angle of attack diagram with data points indicating the start of separation, and thus buffet onset. Last step is to integrate the results over the entire wing, or use e.g. a 3-dimensional potential flow code to acquire the buffet onset boundary for the 3-dimensional case, taking into account a change in Mach number and angle of attack due to sweep and twist of the wing, resulting in a Mach vs C_L diagram instead of a Mach vs α diagram. The most time consuming part of this approach will most probably be the iteration with the non-isentropic potential flow code to construct the 2-dimensional buffet onset points. The diagram of this first approach is shown in figure 2.26

Another approach to determine buffet onset would be using a 3-dimensional inviscid calculation with for example an 3-dimensional Euler method, or 3-dimensional potential flow method. These methods however require a boundary layer model[2]or separation criteria (that can predict separation and transition accurately). Schematically, this would look as shown in figure 2.27 and 2.28.

The third approach would be using a viscid calculation, like RANS, together with a turbulence model to close the set of equations. Again, this turbulence model must be able to predict separation and transition accurately. The diagram of this third approach is shown in figure 2.29. When using a RANS model, it is highly likely that, because of the complexity of most of these turbulence models, an off the shelf model will have to be used to close the RANS equations.

It is expected the two separate calculations of the viscid and inviscid flow, and the convergence between both, is the most time consuming part of any method chosen. Therefore, a 2-dimensional tool like a small disturbance code (which does not rely on this inviscid and viscid convergence) might prove to be a good alternative next to the non-isentropic

[1]The boundary layer model can be seen as an uncoupled part of the simulation and therefore can be used modular to a inviscid or viscid simulation

potential flow code.

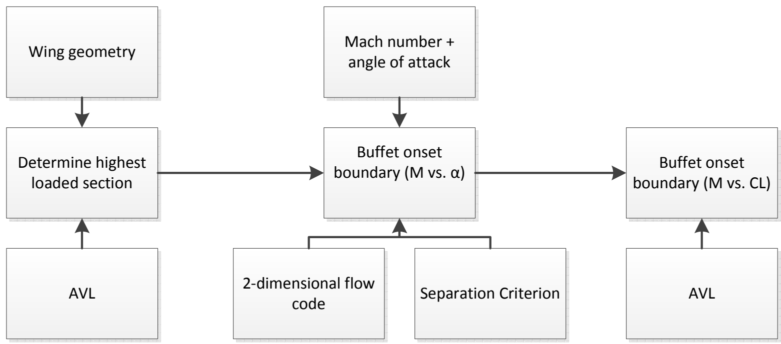

Figure 2.26: 2-dimensional non-isentropic potential flow approach

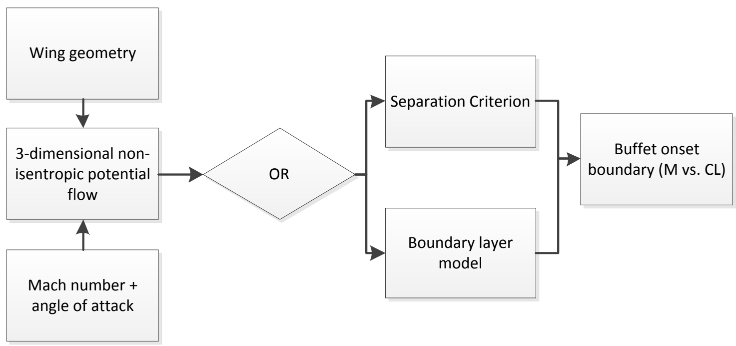

Figure 2.27: 3-dimensional inviscid potential flow approach

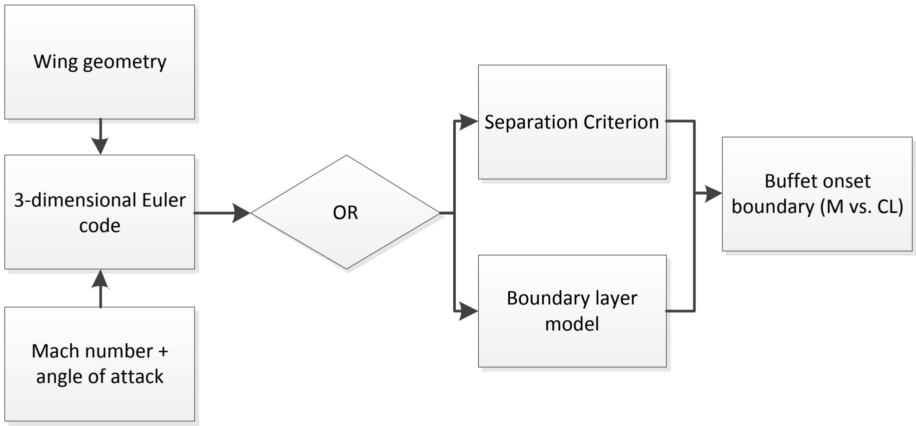

Figure 2.28: 3-dimensional inviscid Euler approach

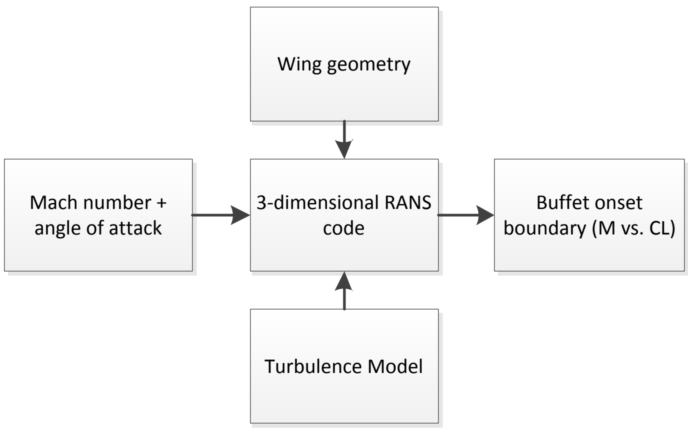

Figure 2.29: 3-dimensional viscid RANS approach

Model Trade-off

In table 2.3 different selection criteria are defined, being the computational time, complexity, how easy is it to implement in a modular fashion in a multi model generator environment, how accurate are the results and how capable is the method in handling various (unconventional) wing geometries. All these criteria are weighted equally and are assessed for the different numerical methods discussed in the beginning of this section. The (semi) empirical method discussed in section 2.2.3 is also included in this table. In table 2.1 a legend is shown for the various approaches, to improve the readability of table 2.3.

The various approaches are rewarded with a score as can be seen in table 2.2. From the result of table 2.3 it can be concluded the 2-dimensional non-isentropic potential flow method in combination with vortex lattice and a separation criteria is the best candidate for a transonic buffet prediction tool to be used in the conceptual design phase. This approach has the advantages it is built up a very modular way (that leaves room for improvement of one of the modules, for example better separation criteria can be implemented fairly easy) and the time consuming calculations are minimized by only using the non-isentropic model on the determination of the shock position and strength of the airfoil. In comparison to the other methods its low complexity, less computational power and time, and high accuracy with respect to for example the 3-dimensional Euler or RANS make it the better choice. Note that it can be seen the addition of a boundary layer model also increases complexity and computational time with respect to the use of a separation criterion. The (semi) Empirical model is discarded because of its incapability to handle unconventional designs and low accuracy. As the proposed method has a 3-dimensional $M_\infty - \alpha$ diagram as output, one last AVL run has to be made for all the buffet onset points to compute the wing lift coefficient C_L so the resulting $M_\infty - C_L$ line is determined. Since this is not significant from a computational time point of view, this is not taken into account in the trade-off.

Since there was no off the shelve 2-dimensional non-isentropic potential flow model at hand, a transonic small disturbance code TSFOIL was used. Another option was to create a 2-dimensional non-isentropic potential flow model during this thesis work, but this is beyond the scope of the assignment. It is expected this 2-dimensional model, which is developed for use in transonic conditions, can determine shock wave position and strength in the same accurate way as the 2-dimensional non-isentropic potential flow model. Next to TSFOIL, also a 2-dimensional Euler code will be implemented as a high end alternative to the 2-dimensional small disturbance simulation. This way, a comparison can be made in terms of accuracy and computational time between these two steps in the buffet onset determination process. In addition, two separation criteria will be implemented, being the critical pressure jump and limiting shock wave Mach number. This way, a total number of 4 combinations can be tested with the tool to be developed, and a trade-off can be made in which combination produces the best results for the conceptual design task at hand.

Table 2.1: Buffet prediction method legend

Approach	Method
A	2-dimensional non-isentropic potential flow with vortex lattice method and separation criteria
B	3-dimensional non-isentropic potential flow with boundary layer model
C	3-dimensional non-isentropic potential flow with separation criteria
D	3-dimensional Euler with boundary layer model
E	3-dimensional Euler with separation criteria
F	3-dimensional RANS with turbulence model
G	empirical method

Table 2.2: Buffet prediction method trade-off scoring

Score	Sign	Value
Outstanding	++	3
Good	+	1
Neutral	0	0
Bad	-	-1
Very Bad	- -	-3

Table 2.3: Buffet prediction method trade-off results

Approach	Time	Complexity	Implementation	Accuracy	Flexibility	Total score
A	+	+	+	+	+	5
B	0	-	0	+	+	1
C	+	0	0	+	+	3
D	0	-	0	+	+	1
E	+	0	0	+	+	3
F	- -	- -	-	++	+	-3
G	++	++	++	- -	- -	3

Chapter 3

Method Implementation

This chapter will give a detailed representation of the build-up of the buffet prediction tool in a way the approach resulting from the model trade-off in Chapter 2, as presented in Figure 2.26, indicates. The different parts of the buffet prediction process are discussed in logical order, starting from the geometry input of the wing-fuselage combination, and resulting in a $M_\infty - C_L$ buffet onset boundary.

3.1 Buffet Prediction Strategy

To predict the transonic buffet onset boundary using the tool developed, the three combinations available are investigated in an advancing order (in both complexity and computation time). That is, the first combination used is the fasted AVL, TSFOIL, AVL combination. If this combination fails to produce an acceptable result, the TSFOIL step will be replaced with the 2-dimensional Euler MSES code. The final combination explored is replacing the final AVL run to determine the wing lift coefficient by a more advanced 3-dimensional method, Matrix-V. Summarizing these three different combinations, in order of increasing computation time:

1. AVL $\rightarrow$ TSFOIL $\rightarrow$ AVL
2. AVL $\rightarrow$ MSES $\rightarrow$ AVL
3. AVL $\rightarrow$ MSES $\rightarrow$ Matrix-V

3.2 Program Architecture

In this section the global program architecture is presented. One of the important requirements for the buffet prediction tool developed was to build it in a modular fashion, meaning parts of the program can be uncoupled and replaced fairly easy. For example, if one would like a different separation criterion or another 2-dimensional flow solver, this can be done without having to alter the entire code. Figure 3.1 shows this modular build-up. It shows the inputs in the left column, the buffet prediction tool in the middle, and the external analyses tools on the right. In the remaining part of this chapter the various inputs, actions and outputs will be discussed in this order, starting with the geometry input, and ending with the $M_\infty - C_L$ buffet onset. Appendix A shows a detailed representation of only the middle column of Figure 3.1, which essentially is the backbone of the buffet prediction tool developed. Appendix A shows the way the different components and functions in Matlab interact together to form the basis of the buffet prediction tool.

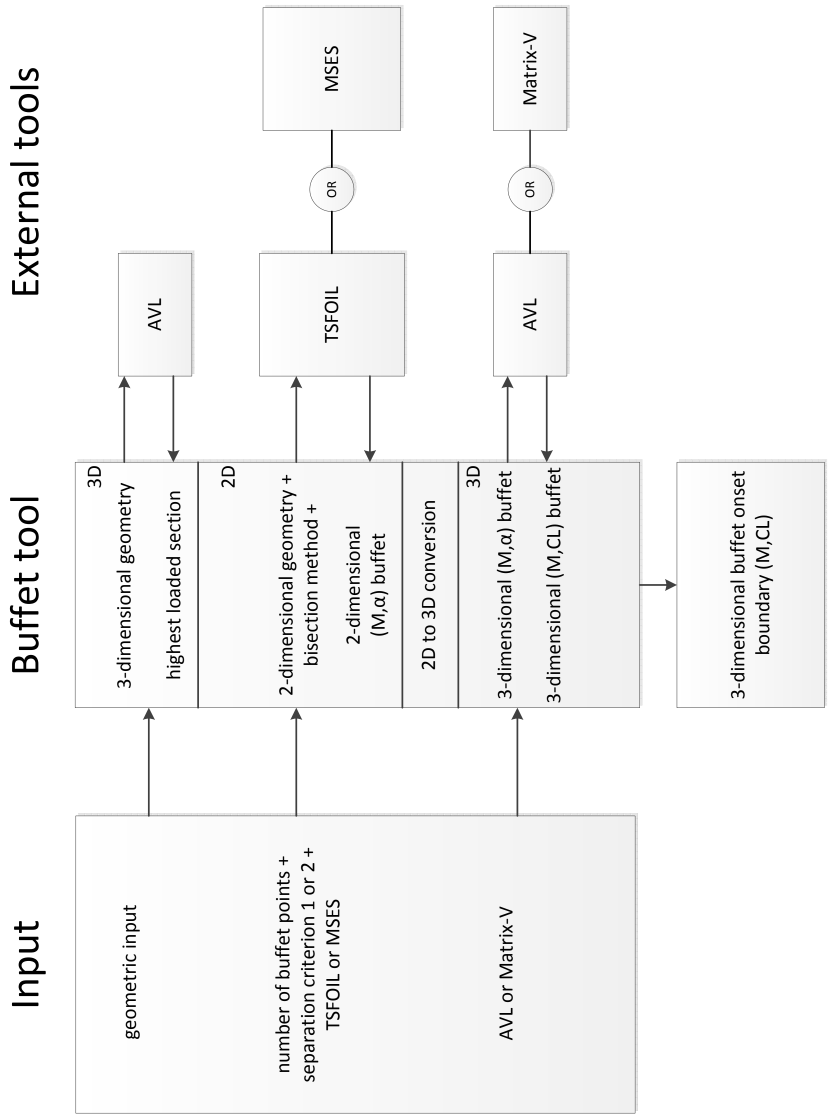

Figure 3.1: Detailed program architecture

3.3 Vortex Lattice Method

First step in the buffet prediction tool is the use of a vortex lattice method to determine the highest loaded section in spanwise direction. This is done using a program called Athena Vortex Lattice (AVL), a program for the aerodynamic and flight-dynamic analysis of rigid aircraft of arbitrary configuration. [30] In addition to the lift distribution AVL can also compute various trim calculations including operating variables, control deflections and their constraints, but this will not be needed during this thesis work. A vortex-lattice model in general works best for aerodynamic configurations which consist of thin lifting surfaces at small angles of attack and subsonic flow conditions. These surfaces and their trailing wakes are represented as single-layer vortex sheets, discretized into horseshoe vortices to compute lift and induced drag. The influence of the thickness, viscosity, turbulence, dissipation and boundary layers is neglected [30]. In addition to this, AVL provides the capability to also model slender bodies such as a fuselage by using sources and doublets. This however means these bodies will not generate any lift. Furthermore, AVL assumes quasi-steady flow, meaning that unsteady vortex shedding is neglected. In this thesis, AVL is only used to determine the spanwise location of the airfoil with the highest local lift coefficient c_l. By looking in the Trefftz plane of the wing-fuselage combination, the local lift coefficient over the wing can be predicted.

In AVL the following assumptions are made:

1. The angle of attack is small
2. The flow field is incompressible, inviscid and irrotational
3. The lifting surfaces are thin, meaning the influence of thickness on aerodynamic forces are neglected

The lifting surfaces of an aircraft is divided into several panels. A horseshoe vortex is applied on each of these panels and the velocity vector generated by the vortices at the collocation points of each panel is computed. The vortex is placed at the $\frac{1}{4}$ chord point of each panel, and the collocation point at $\frac{3}{4}$ chord. The flow at the boundary has to be parallel to the surface at the collocation points, which is the boundary condition in this method. This is also known as the flow tangency condition

Furthermore, the field is a conservative vector field, which means that there exists a velocity potential given by equation 3.1 and Laplaces equation holds. Laplaces equation is a second order linear equation, and is subject to the principle of superposition. This means a complicated flow pattern for an irrotational, incompressible flow can be seen as an addition or subtraction of a certain number of other flows, which are also irrotational and incompressible, for example being sources and sinks.

$$\bar{u} = \nabla\phi \tag{3.1}$$

In addition, AVL uses a compressibility correction, namely the Prandtl-Glauert transformation. This correction, found by linearizing the potential equations associated with compressible, inviscid flow is used to compare aerodynamics that occur at different Mach numbers. This linearization assumes small perturbations and thin surfaces.

In practice, this transformation means the incompressible and inviscid characteristic values of the flow can simply be multiplied with a correction factor to account for the influence of compressibility. This Prandtl-Glauert correction factor is shown in Equation 3.2. In this equation, C_p is the compressible pressure coefficient, M the freestream Mach number, and C_{p_0} the incompressible pressure coefficient. When the Mach number increases, the correction factor increases, and the model becomes unreliable when entering the transonic flow regime. For swept-wings, the wing-perpendicular Mach number is used, as simple sweep theory suggests.

Near sonic conditions, as M_∞ approaches the value of 1, the compressible pressure coefficient is calculated to approach infinity. Because the Prandtl-Glauert correction is a linearized approximation of compressible, inviscid potential flow, the nonlinear phenomena dominate when the flow approaches $M_\infty = 1$. This is completely ignored in the Prandtl-Glauert correction [16].

$$C_p = \frac{C_{p0}}{\sqrt{1 - M^2}} \tag{3.2}$$

As mentioned, AVL can model a simple fuselage, although it will not produce any lift. What exactly is the purpose of defining a fuselage shape together with the wing, when investigating the c_l distribution over the wing? The presence of the fuselage influences the flow over the wing, and can therefore influence the local lift coefficients. Because the local lift coefficient is a criterion on which the highest loaded section is selected, this can be of great influence on the airfoil contour used in the next step of the model, and therefore the resulting 2-dimensional, as well as the 3-dimensional buffet onset boundary. When a fuselage is implemented at this point, this could improve the method considerably. Therefore, a simple tube-like fuselage is attached to the wing. The only two user inputs for this fuselage are the length, and the (maximum) fuselage diameter, d_f. The presence of the fuselage only forces the flow over the wing outboard. This is exactly the purpose of modeling a fuselage in combination with the wing, since more outboard flow might influence the location of the highest local lift coefficient, which is used for further analysis in this program. The fuselage front and end need to be rounded off (decreasing cross sectional area) but not blunt, in order for AVL to be able to simulated doublets on the edge of the panels of the fuselage shape. To accomplish this, in the first and last 15% of the fuselage length the y-coordinate is given by a sinus shape instead of a constant fuselage diameter. Considering the placement of the fuselage with respect to the wings, there is a certain off-set in horizontal and vertical sense to fit the wings to the fuselage in a way it is a better approximation to reality when compared by a placement at 50% of the fuselage and at $z = 0$. The influence of the fuselage on the wing lift coefficient is visualized in figure 3.2. Note this is not a qualitative picture, is shows an expected shift in lift coefficient for an arbitrary wing-fuselage combination.

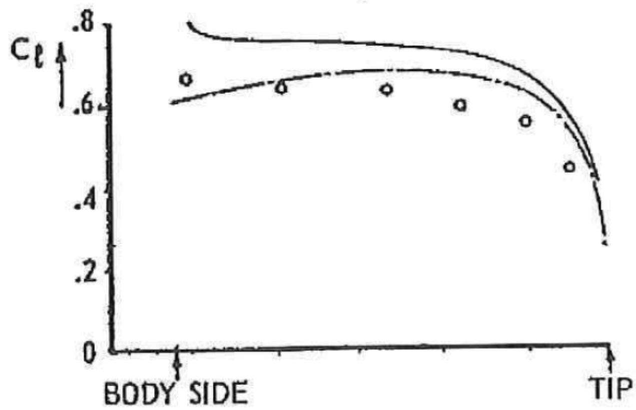

Figure 3.2: Fuselage effect on wing lift distribution [5]

3.4 Flight Conditions

Before the 2-dimensional analyses can start, the set of flight conditions like density, viscosity and temperature needs to be established in order to compute the Reynolds number, which is important for using a separation criterion to determine whether flow is separated or not. A flight altitude is specified by the user, and the other freestream state variables computed with help of isentropic relations and the gas law via Equation 2.2.1. Now the speed of sound, Mach number and viscosity can be computed using Equation 3.8. With this variables known, the accompanying Reynolds number can be computed using Equation 3.13 needed for the buffet onset calculations. T_0, ρ_0, p_0, g_0 and μ_0 are respectively the reference temperature, density, pressure, gravity acceleration and dynamic viscosity at sea-level. In the following equations, R is the universal gas constant, and λ in Equations 3.4 and 3.5 the temperature gradient in the atmosphere.

$$\rho = \frac{p}{R \cdot T}^{\frac{-g_0}{\lambda \cdot R}} \tag{3.3}$$

With the temperature and pressure being the only two variables, which can be obtained using the following two equations:

$$T = T_0 + h \cdot \lambda \tag{3.4}$$

$$p = p_0 \cdot \left[1 + \frac{\lambda \cdot h}{T_0}\right]^{\frac{-g_0}{\lambda \cdot R}} \tag{3.5}$$

With pressure, density and temperature known at a certain flight altitude, the speed of sound and Mach can be computed using the following equations:

$$a = \sqrt{(\gamma \cdot R \cdot T)} \tag{3.6}$$

$$M = \frac{v}{a} \tag{3.7}$$

To be able to compute a Reynolds number, the viscosity of the flow at the flight altitude is needed. Viscosity at sea level, and at a certain altitude are given by:

$$\mu_0 = 0.1827 \cdot c_p \tag{3.8}$$

$$\mu = \mu_o \left[\frac{0.555T_o + C}{.555T + C}\right] \left[\frac{T}{T_o}\right]^{1.5} \tag{3.9}$$

In which C is Sutherland's constant ($120K$ for air). One can rewrite Sutherland's formula to the following:

$$\mu = \frac{\beta \cdot T^{\frac{3}{2}}}{T + C} \tag{3.10}$$

$$\beta = \frac{\mu_0 \left(T_0 + C\right)}{T_0^{\frac{3}{2}}} \tag{3.11}$$

With β is a constant. The kinematic viscosity is computed by dividing the dynamic viscosity by the density, as can be seen in equation 3.12. [31]

$$\nu = \frac{\mu}{\rho} \tag{3.12}$$

And finally the Reynolds number at a certain point in the flow, at a given flight altitude, can be computed using the following equation:

$$Re = \frac{\rho \cdot v \cdot x}{\mu} \tag{3.13}$$

In which x is the position at which the Reynolds number is to be calculated, e.g. the position of the shockwave on the top of an airfoil. To determine the position of the shock wave on the top of the airfoil, that is the $\frac{x}{c}$ coordinate, one simply has to look at the position where the C_p jump is the largest. This translates to a real $x-$coordinate when the $\frac{x}{c}$ is multiplied with the chord of the section under investigation. The flight conditions calculated with the equations above serve as an input for the transonic small disturbance code used to evaluate the pressure distribution over the highest loaded section airfoil, as described in the following sections.

3.5 Airfoil Interpolation

To start the 2-dimensional analyses, first the airfoil contour of the highest loaded section found by AVL has to be constructed. Figure 3.3 shows how this is done. In this figure the highest loaded section is indicated by $\eta_{\max}$ and is surrounded by two user defined airfoils closest to it, indicated by section $\eta_{\max-1}$ towards the root, and $\eta_{\max+1}$ towards the tip. The chord of section $\eta_{\max}$ can be computed by simple linear interpolation of the wing geometry when the spanwise location $Y_{\eta_{\max}}$ where $\eta_{\max}$ is placed is known from the AVL simulation. For the contour of the airfoil $\eta_{\max}$ (the set of x, y coordinates that describe the airfoil upper and lower surface) this requires a more complex interpolation method [32].

When the two surrounding airfoils are defined in exactly the same way, with exactly the same number of coordinates at exactly the same $\frac{x}{c}$ positions, an interpolation between the two airfoils is straightforward. However, in a more general case, this will not occur. For example the $\eta_{\max+1}$ airfoil will consist of 81 coordinates and the $\eta_{\max-1}$ airfoil consists of 85 coordinates. A simple interpolation between each point can no longer be made. To solve this problem, both surrounding airfoils are redefined in the same way. A number of new x-coordinates is chosen (e.g. 100 points) in the domain $0 \leq x \leq 1$ and a weighted average is computed of the two original y-coordinates accompanying the two closest original x-coordinates in the set of airfoil coordinates, with respect to the new x-coordinate. A smart way of choosing the distribution of these new x-coordinates on the chord of the airfoil may result in a better representation of the airfoil contour, especially around the leading-, and trailing edge where in general the curvature is large, and difficult to represent by for example a polynomial expression.

By using a cosine distribution a more dense distribution of new coordinate points will occur at the leading edge and trailing edge. By redefining the airfoil in this way, all airfoils used consist of the same number of (x, y) coordinates and all containing the same x-coordinate on their respective chords. The latter is important because every y-coordinate can be averaged in a straightforward, linear way now. To visualize this, Figure 3.4a shows an airfoil constructed with this method. In this figure, the red dot is the new coordinate computed by averaging the two neighboring original black dots. Special care has to be taken when approaching the leading edge and trailing edge points of the upper and lower side of the airfoil, as they do not have two surrounding x- and y-coordinates to use in the averaging process. Implementing a boundary condition for these points, which essentially means forcing an extra x-coordinate of 0 or 1 and an extra y-coordinate of 0 to average with, depending on the LE or TE position, solves this problem. This is shown in Figure 3.4b and 3.4c where the leading edge and trailing edge are sketched.

The weighted average of each y-coordinate of the airfoil is done as follows:

$$dx = x_{+1} - x_{-1} \tag{3.14}$$

$$dy = y_{+1} - y_{-1} \tag{3.15}$$

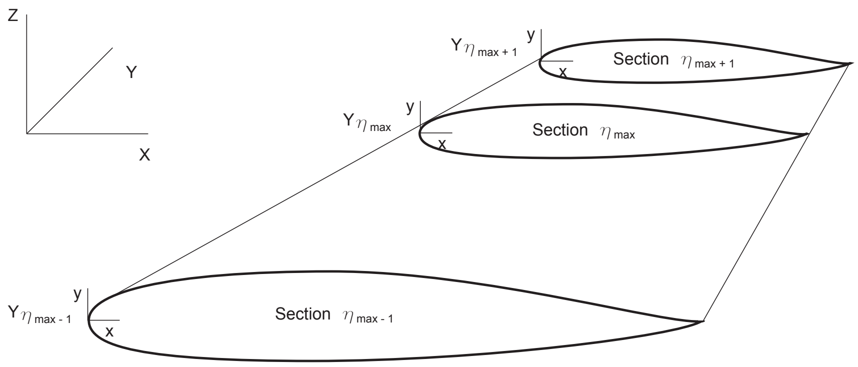

Figure 3.3: Wing trunk

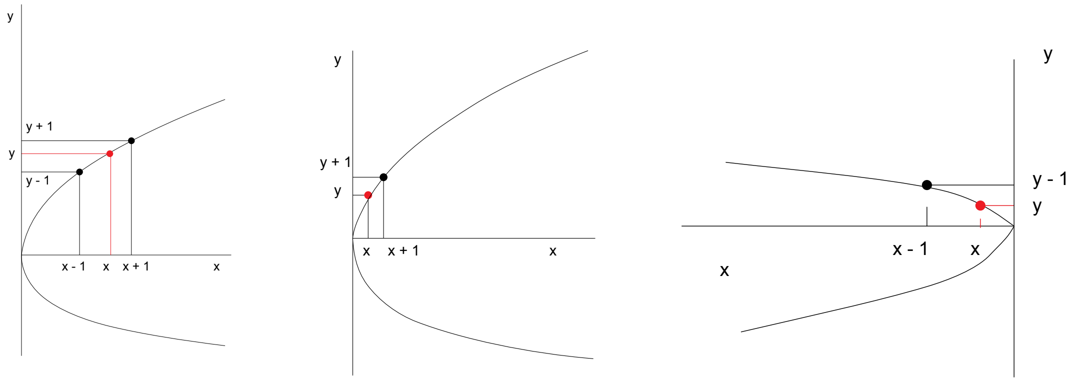

(a) Airfoil construction (b) Leading edge (c) Trailing edge

Figure 3.4: Construction of new airfoil coordinates for a given airfoil near the leading edge and trailing edge (exaggerated representation)

$$y = y_{-1} + \frac{dy}{dx} \cdot (x - x_{-1}) \tag{3.16}$$

The result matrix of y-coordinates for airfoil $\eta_{\max -1}$ and η_{max+1} are then averaged in spanwise direction to arrive at the (x, y) coordinates of the highest loaded section. This is done with help of Equation 3.17.

$$y_{\eta_{\max}} = \frac{Y_{\eta_{\max}} - Y_{\eta_{\max -1}}}{Y_{\eta_{\max +1}} - Y_{\eta_{\max -1}}} \cdot y_{\eta_{\max +1}} + \frac{Y_{\eta_{\max +1}} - Y_{\eta_{\max}}}{Y_{\eta_{\max +1}} - Y_{\eta_{\max -1}}} \cdot y_{\eta_{\max -1}} \tag{3.17}$$

In which capital Y indicates the y-coordinate on the leading edge (spanwise) where the airfoil is placed, and lower case y is the y-coordinate in the (2-dimensional) airfoil coordinate system. The resulting matrix of y-coordinates for the highest loaded section airfoil $\eta_{\max}$ is now know, as well as the accompanying x-coordinates defined earlier.

Airfoil Scaling to Sweep Angle

Cutting the wing at a certain point $\eta_{\max}$ as shown in the previous section in Figure 3.3, introduces a new problem when translating the resulting airfoil from 2-dimensional to 3-dimensional wing characteristics. One could argue how to make the cut. As is shown in Figure 3.3 a cut can be made in streamwise direction. However, when taking into account the perpendicular component of the freestream flow, one also has to make a cut in the wing resulting in an airfoil that is in line with this perpendicular flow component. In other words, a cut has to be made parallel to the flow component used in the 2-dimensional simulation, meaning not cutting in streamwise direction, but perpendicular to the sweep line of the wing. The only variable left is to decide which sweep line. This is a user input, one can choose for example the half chord sweep $\Lambda_{\frac{c}{2}}$, or quarter chord sweep $\Lambda_{\frac{c}{4}}$. To scale the highest loaded section to incorporate the sweep angle of the wing, first the sweep angle has to be determined. Figure 3.5 shows a view of a swept wing, with a known root and tip chord, known points $A(x, y)$ and $B(x, y)$, and known wing span. The sweep line QR is shown at an arbitrary point Q that lies at a certain fraction of the root and tip chord, ϕ, with $0 \leq \phi \leq 1$. So $\phi = 0.5$ indicates the half chord sweep line. The accompanying sweep angle Λ is computed as follows:

$$Q = (\phi \cdot c_{\text{root}}, 0) \tag{3.18}$$

$$R = (x_B + \phi \cdot c_{\text{tip}}, y_B) \tag{3.19}$$

$$|QR| = \sqrt{Q^2 + R^2} \tag{3.20}$$

$$cos\Lambda = \frac{y_B - y_A}{|QR|} \tag{3.21}$$

In which Q and R are points with coordinates (x, y) and $|QR|$ is the length of the sweep line QR. This sweep angle Λ, which now is a function of position of the sweep line, is needed to determine the Mach number and angle of attack of the airfoil with respect to the wing and free stream conditions.

The difference in resulting airfoil is shown in Figure 3.5 and 3.6. By cutting perpendicular to the quarter or half chord sweep line, the resulting airfoil is shorter and thus the thickness-to-chord ratio increases, as the absolute value of y remains constant. This is in essence the simple sweep theory. In this example it means the airfoil will become a little compressed with respect to the streamwise airfoil. The $y-$coordinates (being $\frac{t}{c}$ values, and not absolute y-coordinates) and the chord of the new airfoil cut are computed by using the following relation shown in Equation 3.22 and 3.23. In these equations, subscript s is in streamwise direction, and subscript e is parallel to the flow vector (and perpendicular to the sweep line).

$$y_e = \frac{y_s}{cos\Lambda} \tag{3.22}$$

$$c_e = c_s \cdot cos\Lambda \tag{3.23}$$

There are multiple ways of dealing with this mapping problem. The steps taken in this thesis is as follows: The airfoils $\eta_{\max -1}$, $\eta_{\max}$ and $\eta_{\max +1}$ are defined in the free stream direction, along the body axis of the wing. Then, when the resulting weighted averaged airfoil $\eta_{\max}$ is computed, also in stream wise direction, the airfoil coordinates are mapped onto a cut perpendicular to the sweep line of choice with the help of Equation 3.22 and 3.23. Figure 3.6 shows (exaggerated) the two airfoils, the long one being the streamwise airfoil, and the compressed one being the rotated airfoil.

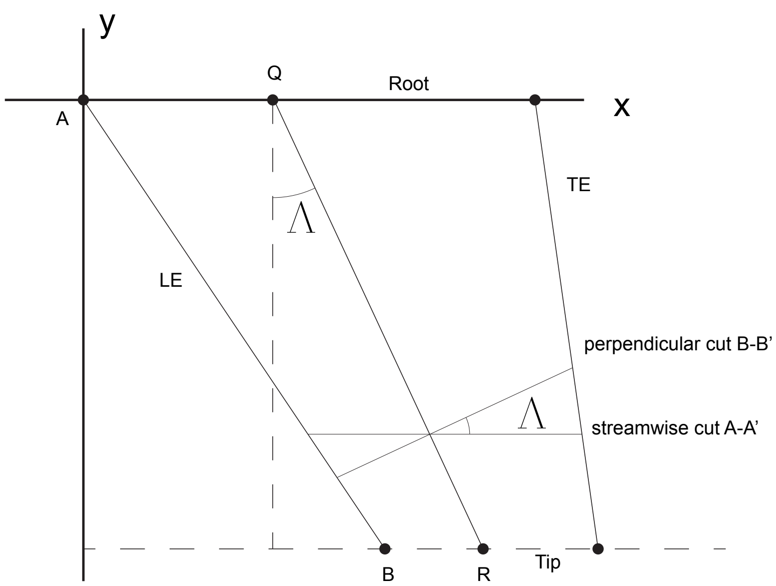

Figure 3.5: Mapping cut $\eta_{\max}$ perpendicular to sweep line QR under sweep angle Λ

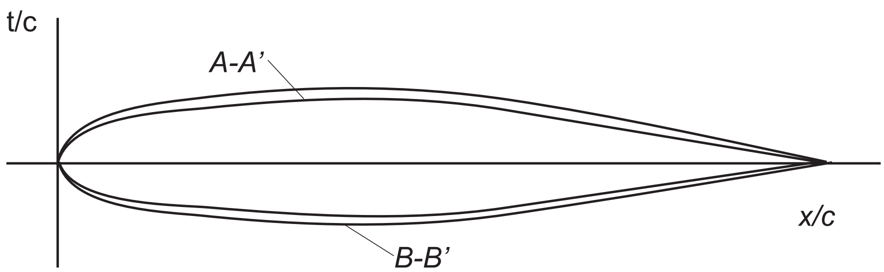

Figure 3.6: Difference in airfoils contour of cut $A - A'$ and $B - B'$

3.6 Transonic Small Disturbance Code

With the airfoil contour of the highest loaded wing section known, the second step in the buffet onset prediction is the 2-dimensional simulation of the flow under a range of angles of attack α and free stream Mach number M_∞. In this step the situation changes from the 3-dimensional wing to a 2-dimensional airfoil. For this part of the buffet prediction, the TSFOIL program is initially proposed. The TSFOIL small disturbance potential code is coupled to Green's lag entrainment method [33] to compute transonic separated flows over airfoils and does not use an iterative procedure between the viscous and inviscid flows because of this [33]. The code promises to be quick, and provides useful results. The reason TSFOIL is the code initially proposed, is the computational time aspect. There are some restrictions with respect to the input parameters for this program, for example $\alpha \in [-9, 9]$ degree, and $M_\infty \in [0.5, 2]$ with the exemption of $M_\infty = 1$. It has to be stated the program gives a warning that for certain combinations of α and M_∞ the pressure jump over the shock becomes that large, the results may be erroneous. This is the case when for example the local Mach number right before the shock wave reaches values of about 1.3 and up. This is somewhat in line with the cut-off Mach number of around $M_\infty = 1.2 - 1.3$ which was obtained from Figures 2.22a and 2.22b. The theoretical maximum local Mach number in front of the shock will be $M_\infty = 1.48$ as was mentioned in Chapter 2 by Laitone's analysis. If this poses a problem in computing the high speed buffet onset boundary, which could contain local Mach numbers in this realm, it might be better to use results obtained from a 2-dimensional Euler code.

The output generated by this 2-dimensional solver consists of the local Mach number distribution over the upper and lower surface, as well as the pressure distribution over both surfaces. With this information, the $\frac{x}{c}$ location of the shock wave can be determined, looking at an abrupt pressure rise (rise in C_p) and drop in local Mach number M_{local}. Besides the position of the shock, there is also information on the shock strength, by looking at the magnitude of the pressure rise over the shock. This information, together with the local Mach number before the shock, can be used in combination with a separation criterion to determine whether a certain combination of α and M results in separated flow, being the beginning of buffet, and therefore a data point in the buffet onset diagram.

3.7 2-dimensional Euler Code

The 2-dimensional Euler code used as an alternative to TSFOIL is MSES. MSES is a multi-element airfoil design and analysis software tool, which couples viscous and inviscid Euler method. It can be applied in a broad spectrum of airfoil design, for single and multi-element airfoil analysis. It has no speed limits, as it can analyze subsonic, transonic and supersonic flow. This in particular is interesting for the simulation of the transonic flow cases considered in this thesis research, since the transonic small disturbance code TSFOIL might have some problems coping with high local Mach numbers due to increasing angle of attack or freestream Mach number [34].

The numerical formulation of MSES consists of a finite-volume discretization of the Euler equations. Essentially, a streamline-based Euler discretization and a two-equation boundary layer formulation are coupled through the displacement thickness and solved simultaneously. MSES offers a number of modes to analyse the flow within its 2-dimensional Euler model. Analysis mode 3 uses boundary layer coupling with transition prediction. Momentum will be conserved, except near the leading edge and a second-order upwind scheme is used. Analysis mode 4 also uses boundary layer coupling with transition prediction but conserves entropy instead of momentum, except near shocks. Also a 2nd-order upwind scheme is used. [34] MSES allows for forced or free boundary layer transition, but to speed up the simulation transition is set at approximately 5% of the chord, since the exact transition point is not of interest in this thesis.

From the practical side, MSES uses two input files for every run, being a geometry file that defines the airfoil and gridlines, and a runtime parameters file that changes every iteration when α or M_∞ is changed. In this file also the Reynolds number is updated every run, since the airspeed is not constant. To compare: TSFOIL uses one file with all information. The advantage of using the MSES code is the geometry file does not have to be created every iteration, since only the file with runtime parameters changes. This is a little more efficient, and reduces the computational time to some extent.

One of the drawbacks of MSES is that it is a Linux based program. Using it in a Windows environment required the Fortran code to be compiled again. The Windows version, which was built at the faculty of Aerospace Engineering of the TU Delft, did not have the option to write the output data (the pressure distribution, boundary layer shape factor, skin friction coefficient and more) to a file. The Fortran source code had to be altered in order to make MSES run under windows, and Matlab, in an iterative way, and be able to write an output file with the pressure distribution instead of only using a plot routine as is the case in the Linux distribution. Because the only parameter of interest for this thesis was the C_p distribution as a function of $\frac{x}{c}$, some lines of code were added to make it possible to skip the plot routine, and write an output file instead.

3.8 Bisection Method

To arrive at the combinations of Mach number and angle of attack $M-\alpha$ that induce buffet for a certain airfoil, a smart choice has to be made in combining these two variables in calculating the shock position and pressure jump magnitude in the 2-dimensional airfoil case. One could choose to iterate for all combinations of α and M_∞ values, but this requires more computational time, since all combinations of these two variables are tested. Using a bisection method, one could minimize the number of computations needed to arrive at a certain buffet onset point. The bisection method is essentially a root finding method which repeatedly bisects an interval and then selects a subinterval in which a root must lie for the next iteration. To keep this bisection from running infinitely long, a certain stop criterion is needed. At each step the method divides the interval in two by computing the midpoint $c = \frac{a+b}{2}$ of the interval and the value of the function $f(c)$ at that point. Unless c is itself a root (which is very unlikely, but possible) there are now two possibilities:

1. $f(a)$ and $f(c)$ have opposite signs and bracket a root.
2. $f(c)$ and $f(b)$ have opposite signs and bracket a root.

The method selects the subinterval that is a bracket as a new interval to be used in the next step. In this way the interval is reduced in width by 50% at each step. The process is continued until the interval is sufficiently small, and the stop criterion is reached. This process is shown in Figure 3.7.

The first interval points a and b are chosen in such a way, the target value (the buffet onset point) is always in this interval, so the signs of $f(a)$ and $f(b)$ are always opposite. Meaning, there is always buffet (+) and no buffet (−) at each one of the interval Mach values a and b. In this case, $a = 0.20$ and $b = 0.95$. The whole process is visualized in Figure 3.8 for 5 and 10 buffet points. Essentially the method as shown in Figure 3.7 is executed along one of the red lines in Figure 3.8. The red lines along which this bisection method is applied are under a certain angle with respect to the $x-$axis as shown in this figure. This angle determines the coefficient C_1 in Equation 3.24 so an educated guess has to be made under which angle the red bisection lines have to be defined. The equation for a red line in Figure 3.8 is given by Equation 3.24.

$$f(x) = \alpha = C_1 \cdot M + C_2 \tag{3.24}$$

In which the constant $C_1 = 5\ \frac{deg}{M}$ and the same for every red line. Constant C_2 defines the starting point of the different lines along which the bisection method is executed. This means a number of C_2 coefficients is chosen, and together with C_1 this results in the same number of red lines on which bisection will determine a buffet onset Mach number, and with the relation in Equation 3.24 the accompanying α. The bisection method has to be ran for each red line. The resulting 2-dimensional buffet onset points will have to be connected in a smooth way later on, as is explained in the next paragraph. For each red line, the method will normally need some number of iterations to reach the target value, depending on the tolerance used (the stop criterion, $b-a$). But since the buffet prediction tool developed in this thesis work returns a 'true' or 'false' for buffet onset for a certain $\alpha - M$ combination, the stop criteria will not be an absolute number or function value $f(x)$. Instead a certain number of iterations after which is assumed the maximum error that can occur is small enough is defined. Assuming the error has become sufficiently small in the scope of the rest of the tools used in this model after 10 iterations, this is set to be the stopping criterion of the bisection method. Theoretically, the maximum error that can occur is shown in Equation 3.25

$$\frac{1}{2} \cdot (b-a) \cdot \left(\frac{1}{2}\right)^n \tag{3.25}$$

With n the number of iterations, and $\frac{1}{2}$ because the interval becomes smaller with 50% every iteration. This means after 10 iterations, the maximum error has become $3.66 \cdot 10^{-4}$ which is very accurate. The user could choose to lower the number of bisection iterations per line at a cost of a larger potential error. This however would speed up the total computation time significantly. The resulting target value computed is a Mach number, and can be coupled to the accompanying α by Equation 3.24.

What is left is defining the bandwidth and spacing of the C_2 points (e.g. the spacing of the red lines). The minimum value of $C_2 = -7.5$ and the maximum $C_2 = 0$. These values where found by trial and error, and produced good results when running the model. The distance between the red lines on which the bisection is executed is given by the C_2 step size, which is defined in Equation 3.26. In this Equation $C_{2_{\text{number}}}$ is the number of buffet points desired, a user input. This means the grid of the buffet onset diagram gets finer, as the number of buffet onset points increases, and the buffet onset diagram is not expanded into the subsonic or supersonic regime as the number of buffet points increases. This is shown in Figure 3.8(b) in which the number of lines have doubled with respect to Figure 3.8(a)

$$\Delta C_2 = \frac{5}{C_{2_{\text{number}}}} \tag{3.26}$$

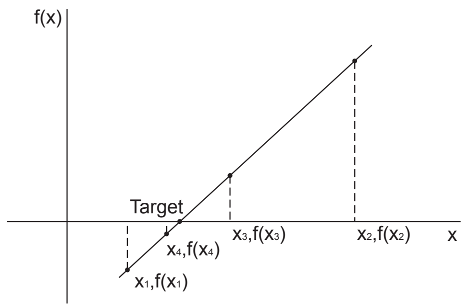

Figure 3.7: Bisection of method with one variable x used to approximate the root of $f(x)$

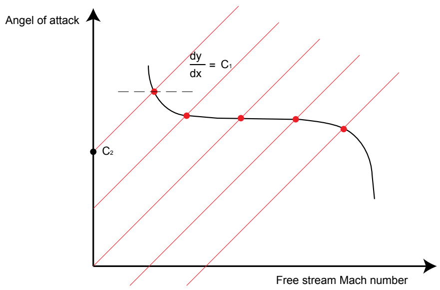

(a) number = 5

(b) number = 10

Figure 3.8: Bisection method with two variables, $f(\alpha, M)$ used in buffet tool

3.9 Separation Criteria

During the bisection method, the correct interval has to be chosen with the help of a separation criterion. As can be read in Chapter 2, two separation criteria were used in this thesis research, being the critical pressure jump across the shock required for separation, and the local Mach number in front of the shock. Since MSES was not programmed to write an output file containing the local Mach number as a function of the chord wise position $\frac{x}{c}$, the user does not have the option to choose the local Mach number separation criteria when simulating with the 2-dimensional Euler code. When using the transonic small disturbance option, one can choose which one of the two separation criteria to use.

3.9.1 Critical Pressure Rise Across Shock Wave

Donaldson and Lange [10] have correlated the pressure rise to separation for different Reynolds numbers as shown in Figure 2.18 of Chapter 2. The relation used to determine whether a pressure jump is large enough to induce separation to a turbulent boundary layer, Equation 3.27 is used. In this formula, Rey_∞ is the Reynolds number based on the velocity and viscosity of the undisturbed flow, at the x-position of the shock wave. This is computed by multiplying the location of the shock wave (the location of the pressure jump) in terms of $\frac{x}{c}$ with the chord of the section under investigation, being the chord of the highest loaded section $\eta_{\max}$ which is determined in the beginning of this process.

$$\Delta C_p = \frac{4.5}{Rey_\infty^{\frac{1}{5}}} \tag{3.27}$$

3.9.2 Limiting Shock Wave Mach Number

In Chapter 2 Section 2.1.7 it has been shown that the shock wave on a convex profile that can terminate the local supersonic region can have a maximum Mach number of $M_s = 1.483$ and the local supersonic flow over a thin convex profile (in isentropic flow) is limited to $M^* = \sqrt{2}$. Besides the separation criteria which relies on the magnitude of the pressure jump in combination with the Reynolds number at the position of the shock, one could also use the local Mach number as separation criteria. Figure 2.19 shows this local Mach number and chordwise position combinations of the shock wave that are likely to produce buffet. From this figure, the following linear relation was derived, as can be seen in equation 3.28. In practice this implies the position of the shock is the input for determining the local Mach number required for separation. This is compared with the local Mach number resulting from the simulation to see whether there is separation or not.

$$M_{sep} = 1.483 - 0.50 \cdot \left(\frac{x}{c} - 0.3\right) \tag{3.28}$$

3.10 Airfoil to Wing Transformation

With the shape and contour of the highest loaded section airfoil known, scaled to encorporate the sweep angle, and the $M_\infty - \alpha$ combinations which induce buffet of the 2-dimensional airfoil simulation, a transformation of the 2-dimensional results to the 3-dimensional wing case is needed in order to be able to provide a buffet onset diagram for the wing-fuselage combination instead of 2-dimensional $M_\infty - \alpha$ line for section η_{max}. This problem can be divided into two different parts:

1. Scale freestream Mach number from 2-dimensional to 3-dimensional
2. Scale angle of attack from 2-dimensional to 3-dimensional

When the 3-dimensional $M_{\infty_{\text{wf}}}$ and α_{wf} are known, the wing lift coefficient C_L can be computed with help of another run in a vortex lattice program, or other more accurate 3-dimensional code, and the buffet onset boundary of the wing is known.

Translate Angle of Attack

Next step is to define the translation between 2-dimensional angle of attack and free stream Mach number, and the 3-dimensional case. The dihedral effect on the tilting of the lift vector is neglected. One could choose to incorporate this by using the cosine of the dihedral angle to scale with, but since the dihedral angle will only be a few degree, this factor will be approximately one. The free stream flow vector and Mach number are not the same for the 2-dimensional case and the 3-dimensional case. The vectors are both not equal in size and direction because of the sweep, twist and incidence angle of the different airfoils at the various wing segments. The twist angle changes the orientation of the airfoil with respect to the incoming flow. The angle of attack used by the transonic small disturbance code or 2-dimensional Euler code is α. This total angle α consists of 2 angles θ and α_{airfoil}. Angle α_{airfoil} is the angle between the horizon and the local freestream vector, and θ the angle between the orientation of the airfoil and the horizon. This results in the following relation:

$$\alpha = \alpha_{\text{airfoil}} + \theta \tag{3.29}$$

The total angle of attack of the wing-fuselage combination, α_{wf}, is a function of the angle of attack of the airfoil, α_{airfoil}, the sweep angle at a certain percentage of the chord, Λ, and angle θ. The purpose of twist in general is to ensure that the wing tip is the last part of the wing surface to stall. Therefore, the wingtip is twisted a small amount leading edge down with respect to the centerline of the fuselage. This ensures that the geometrical angle of attack is always lower at the wingtip than at the root. Therefore the relation between the angle of attack of the airfoil, and that of the wing-fuselage becomes as shown in equation 3.30.

$$\alpha_{\text{wf}} = \frac{\alpha_{\text{airfoil}} + \theta}{cos\Lambda}) \tag{3.30}$$

Angle θ is the incidence angle of the airfoil section, which essentially is the twist of the wing at that spanwise location. Since the cut $\eta_{\max}$ is at an arbitrary point, θ is determined by a weighted average value of the known twist angles at $\eta_{\max-1}$ and $\eta_{\max+1}$. The wing twist of the input airfoils is defined with respect to the quarter chord line, projected on to the x-y plane. This averaging of the twist angle results in the equation as can be seen in Equation 3.31.

$$\theta_{\eta_{\max}} = \frac{Y_{\eta_{\max}} - Y_{\eta_{\max-1}}}{Y_{\eta_{\max+1}} - Y_{\eta_{\max-1}}} \cdot \theta_{\eta_{\max+1}} + \frac{Y_{\eta_{\max+1}} - Y_{\eta_{\max}}}{Y_{\eta_{\max+1}} - Y_{\eta_{\max-1}}} \cdot \theta_{\eta_{\max-1}} \tag{3.31}$$

Translate Freestream Mach Number

The freestream flow is composed of two components, perpendicular and tangent to the leading edge of the wing. The component of the flow vector that is perpendicular to the wing is the free stream Mach number used in the 2-dimensional simulation, so a transformation back to the 3-dimensional free stream Mach number is needed, when transforming the 2-dimensional buffet onset diagram to the 3-dimensional case. The relation between the 2-dimensional and 3-dimensional Mach number is described as follows:

$$M_{\infty_{\text{airfoil}}} = M_{\infty_{\text{wf}}} \cdot cos\Lambda \tag{3.32}$$

So to transfer back from 2-dimensional to 3-dimensional results, equation 3.32 is re-written to equation 3.33.

$$M_{\infty_{\text{wf}}} = \frac{M_{\infty_{\text{airfoil}}}}{cos\Lambda} \tag{3.33}$$

3.11 Wing Lift Coefficient

To determine the wing buffet onset boundary, the 3-dimensional $M_\infty - C_L$ line, the data known at this point in time is the 3-dimensional $M_\infty - \alpha$ points. This needs to be converted one last time from an angle of attack and free stream Mach number to wing lift coefficient C_L and freestream Mach number. To do so, the AVL program is proposed for a second time. The wing-fuselage combination defined in the beginning of the simulation sequence serves as input for this last set of AVL runs. Together with the angles of attack and free steam Mach numbers that result from the 3-dimensional buffet onset boundary, AVL returns a wing lift coefficient C_L. If the resulting $M_\infty - C_L$ values are plotted, this results in the final wing buffet onset boundary. The use of a (simple) panel method for computing the wing C_L values in transonic conditions is doubtful, but a fast way of relating angle of attach to wing lift coefficient. In the last combination proposed in Section 3.1 the AVL runs at the end of the program are replaced by Matrix-V runs to compute the final 3-dimensional $M_\infty - C_L$ line and predict the wing lift coefficients more accurately.

Chapter 4

Demonstration and Results

This chapter will focus on the demonstration of the method developed in this thesis with the help of a test case based on the Fokker 100. The Fokker 100 is an excellent example of a test case for this method, because its detailed wing geometry (including airfoils) as well as buffet onset data is available. First the geometric input of the Fokker 100 wing-fuselage combination will be presented. After this, the results of the three combinations and two different separation criteria (as mentioned in Section 3.1 and listed below) will be evaluated with respect to accuracy, range and computational time.

1. AVL → TSFOIL → AVL
2. AVL → MSES → AVL
3. AVL → MSES → Matrix-V

4.1 Test Case Fokker 100

The wing geometry of the Fokker 100 wing is shown in Table 4.1 [35]. Next to this main wing parameters, with the help of information in the DARWING repository of the TU Delft, six airfoils can be defined at accompanying spanwise locations, as can be seen in Table 4.2 and Figure 4.1a through 4.1f. The Fokker 100 has a kink in the wing, at approximately 33% of the span. In Table 4.3 the rest of the input parameters are shown, such as the $(x, y, z$ location of the airfoils of the wing. The X_{LE}-coordinates indicate wing sweep, the Y_{LE}-coordinates indicate the span wise location of the airfoil, and the Z_{LE}-coordinates indicate wing dihedral.

Next to this information, the incidence angle of all airfoils used in the wing is needed in order to make an accurate calculation of the location at which the local lift coefficient of the wing is largest and translate the 2-dimensional result to the 3-dimensional results.

From a Fokker report [36] the incidence angle of the wing itself with respect to the fuselage, and the twist of three wing segments (root, kink and tip) is implemented. The wing incidence angle is 3.66 degree, and the twist distribution at root, kink and twist is found in Table 4.2. This information proved hard to be found in detail, but with the help of the information from the Fokker report, and of the Aircraft Development and Systems Engineering company (ADSE) Table 4.2 could be constructed. The twist angle of the sections in between the root and kink, and kink and tip are determined by means of linear interpolation between the known thee values of the interval root-kink and kink-tip. It has to be stated these angles are in jig condition, and not under $1-g$ loading, which would have been a better representation of the wing shape in flight near buffet onset conditions. However, this data was not at hand. The twist is defined with respect to the quarter chord line, projected on to the x, y-plane, which is the same definition AVL uses. The incidence angle of a certain airfoil with respect to the incoming flow is the incidence angle of the wing-fuselage, 3.66 degree, plus its local twist angle.

The planform area, or reference area, is computed by using Equation 4.1 and is done by multiplying the span with the product of the wing root and tip chord, divided by 2. This is a reasonably accurate computation of the planform area of the wing. Although for certain wing geometries containing for example a kink like the Fokker 100, this calculation is incorrect. Using equation 4.1 the planform area of the Fokker 100 wing would be $91.78m^2$, but the Fokker report [2] states the planform is $93.50m^2$. Since this buffet onset prediction tool should work for an arbitrary wing geometry, there is a need for some sort of reference area computation formula, or to make it a user input parameter. The best option would be to determine the planform area for every wing trunk, separated by an airfoil. For simplicity sake, and the fact this small ΔS_{ref} is expected to have little influence on the outcome of the buffet onset prediction (since it is only used to compute forces on the wing during the AVL run) it is left a user input. This means for the Fokker 100 test case the computed lift coefficients of the wing will be somewhat higher than in reality.

$$S_{\text{ref}} = \frac{b \cdot (c_{\text{root}} + c_{\text{tip}})}{2} \tag{4.1}$$

Table 4.1: Fokker 100 wing parameters

Wing parameters			
Wing span	b	28.08	$[m]$
Wing area	S	93.5	$[m^2]$
Aspect ratio	A	8.43	$[-]$
Root chord	c_{root}	5.60	$[m]$
Tip chord	c_{tip}	1.26	$[m]$
Taper ratio	λ	0.24	$[-]$
Fuselage diameter	d_f	3.30	$[m]$
Quarter chord sweep angle	$\Lambda_{0.25c}$	17.45	$[deg]$

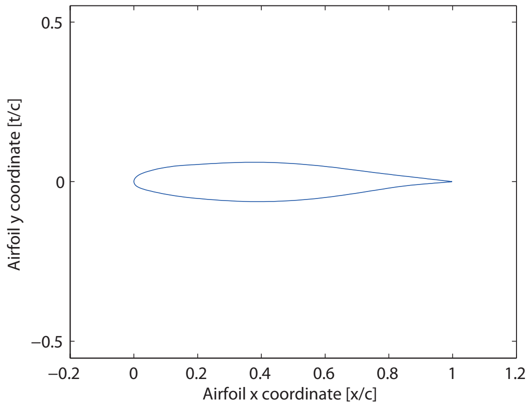

(a) F100-1mod airfoil

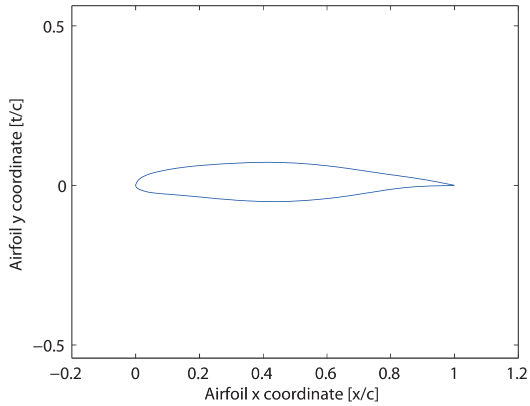

(b) F100-2mod airfoil

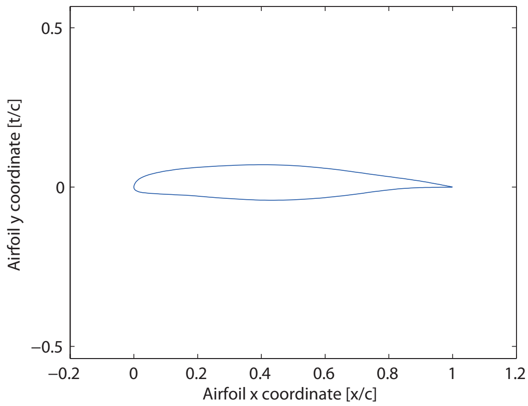

(c) F100-3mod airfoil

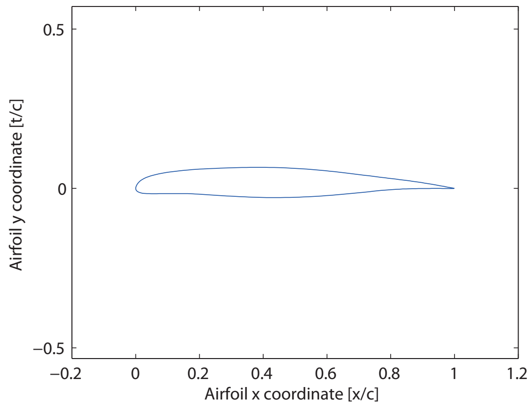

(d) F100-4mod airfoil

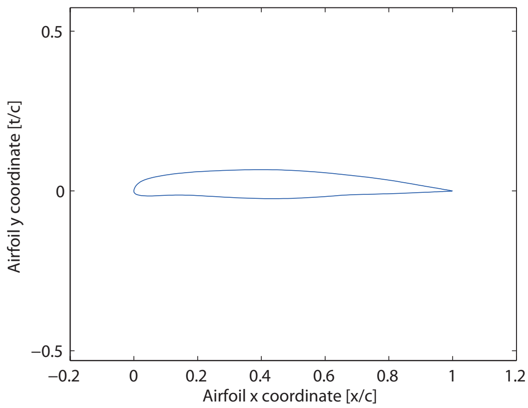

(e) F100-5mod airfoil

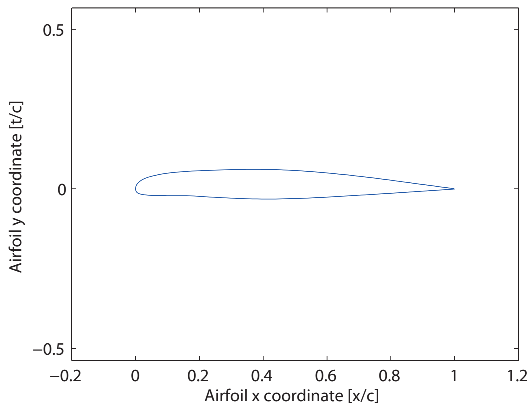

(f) F100-6mod airfoil

Figure 4.1: Fokker 100 airfoils

Table 4.2: Fokker 100 airfoils

F100 Airfoils	spanwise location [%]	twist [deg]	total incidence angle [deg]
f100-1mod	0.00	0.00	3.66
f100-1mod	0.12	-0.24	3.42
f100-2mod	0.33	-0.65	3.01
f100-3mod	0.46	-1.58	2.08
f100-4mod	0.59	-2.45	1.21
f100-5mod	0.79	-3.95	-0.29
f100-6mod	0.96	-5.13	-1.47
f100-6mod	1.00	-5.40	-1.74

Table 4.3: Fokker 100 wing, airfoil positioning, from root to tip

Airfoil positioning [m]								
	1mod	1mod	2mod (kink)	3mod	4mod	5mod	6mod	6mod
X_{LE}	0	0.86	2.34	2.96	3.54	4.54	5.32	5.50
Y_{LE}	0	1.70	4.60	6.44	8.18	11.16	13.52	14.04
Z_{LE}	0	0.07	0.20	0.28	0.36	0.48	0.59	0.61
Chord	5.60	4.86	3.60	3.14	2.71	1.97	1.38	1.26

4.2 Results

Since there are two 2-dimensional simulation tools available in the developed tool, being the transonic small disturbance code TSFOIL and the 2-dimensional Euler code MSES, and two separation criteria, being the pressure jump at the position of the shock and the local Mach number in front of the shock, in theory there are 4 combinations possible to determine the buffet onset boundary. However, this is not the case. Reason for this is the fact the MSES code was re-coded and built in order to remove the plotting options which are available in the Linux distribution. Instead, an option was made available to write the resulting C_p distribution over the airfoil to an output file. This was not done for the local Mach number in front of the shock, but only for the pressure distribution over the airfoil. This means when MSES is used instead of TSFOIL, only one separation criteria is available at this moment. This limits the total number of possible simulation options to three. More information on the re-coding of MSES can be found in Chapter 5 at the Conclusions and Recommendations section.

First the results of the AVL-TSFOIL-AVL method will be discussed, using both separation criteria. Secondly, the AVL-MSES-AVL method will be discussed, using only the critical pressure rise separation criterion for reasons mentioned above. And finally the results of the AVL-MSES-MatrixV method will be presented, which is essentially using the intermediate $M_\infty - \alpha$ results of the AVL-MSES combination, and predicting the wing lift coefficients with Matrix-V instead of AVL.

A report from Fokker [2] provides the flight test F100 buffet onset boundary which serves as a benchmark for the results of the AVL, TSFOIL, MSES and MatrixV simulations. Figure 4.2 shows this transonic buffet onset boundary.

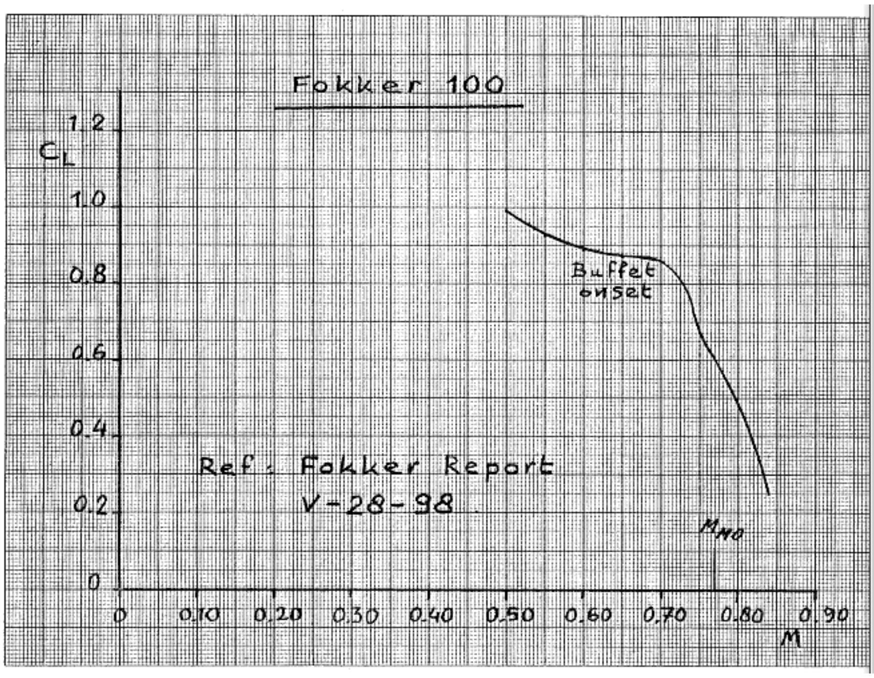

Figure 4.2: Fokker 100 buffet onset flight test [2]

4.2.1 AVL Prediction

The first part of the buffet onset program determines the highest loaded section of the wing-fuselage combination, in spanwise direction. When the wing and fuselage contours have been created with the user input parameters, AVL is ran and the c_l distribution is extracted from the results, as well as a plot of the loading over the wing and the Trefftz plane in the far field to visualize this. The resulting Trefftz plane analyses shows the local lift coefficient c_l as a function of spanwise coordinate. This Trefftz plane plot produced after the AVL run (at $M_\infty = 0.5$ and $\alpha = 0°$) is shown in Figure 4.4 in which the middle line is the local lift coefficient c_l.

Figure 4.3 shows the loading over the Fokker 100 wing and simple fuselage shape. The freestream flow conditions are chosen so they do not conflict with the limits of AVL with respect to maximum Mach number or angle of attack. Simulating at cruise conditions will only change the absolute value of the local lift coefficients, but will not influence the spanwise distribution of c_l. The resulting contour of the airfoil at this spanwise location (after airfoil interpolation procedure) denoted by section $\eta_{\max}$ is shown in Figure 4.5. The location of this airfoil in spanwise sense, incidence angle and chord are the input for the next step of the buffet prediction tool, the 2-dimensional analyses. The highest loaded section found by AVL lies at $Y_{LE} = 5.53m$ in spanwise sense, the chord is $c = 3.17m$ and the incidence angle $\theta = 2.54deg$. As mentioned in Chapter 3 a simple fuselage is modeled to incorporate the effect of the fuselage on pushing the flow outboard, and influencing the position of the section with the highest loading. A second run without fuselage was executed to see whether this influence is visible in the AVL results, and it did not. The characteristics of the highest loaded section remained the same with-, and without the fuselage.

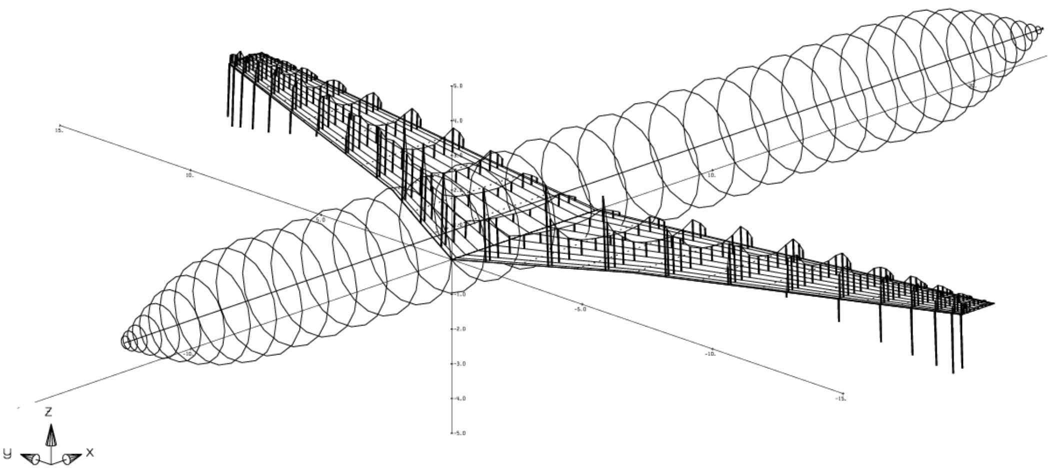

Figure 4.3: Fokker 100 wing-fuselage combination and loading after AVL run

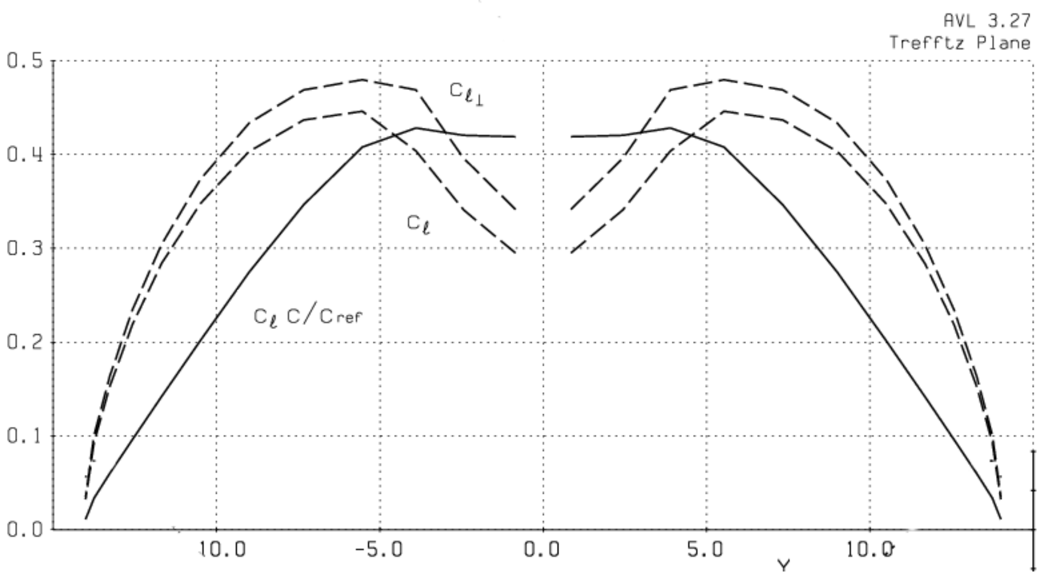

Figure 4.4: Fokker 100 wing-fuselage combination, Trefftz plane at $M_\infty = 0.5$ and $\alpha = 0°$

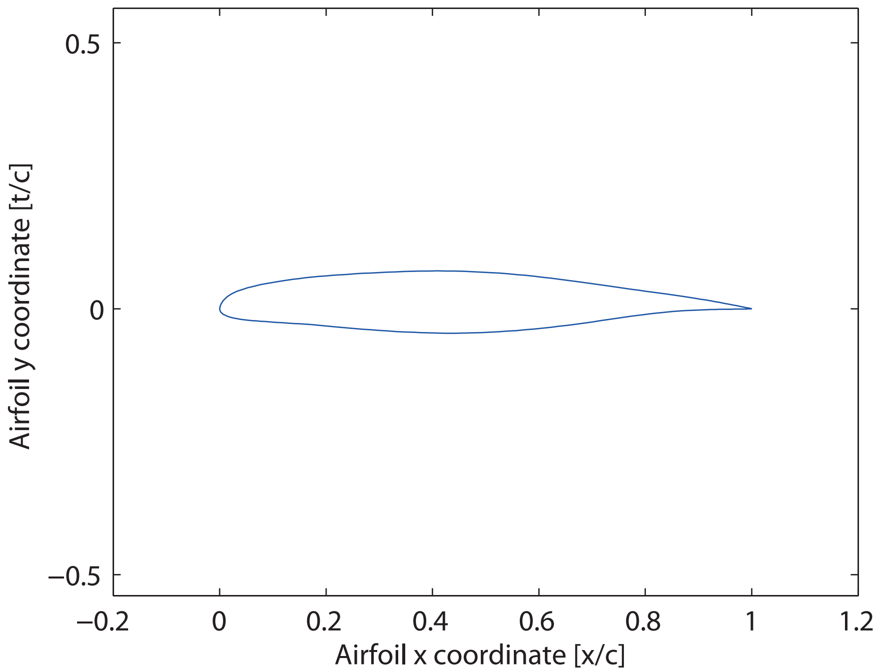

Figure 4.5: Fokker 100 highest loaded section $\eta_{\max}$

4.2.2 TSFOIL Results

Following the AVL run, the 2-dimensional analyses of the resulting airfoil $\eta_{\max}$ can be done in two ways. Using the transonic small disturbance code TSFOIL, both separation criteria can be used. Table 4.4 shows the summarized transonic buffet onset prediction of the Fokker 100 test case using TSFOIL. Accompanying this table, Figures 4.6 through 4.7 show the buffet onset boundary of this Fokker 100 wing-fuselage combination with a wing sweep angle at half chord. In addition, an indication of the Reynolds number is shown. Since the Reynolds number changes with the freestream Mach number, and thus is different for each TSFOIL run, an indication is given instead of all the separate values. The resulting figures are 3-dimensional buffet onset boundaries, so the transformation from 2-dimensional results to the 3-dimensional wing case as described in Chapter 3 has already been done. The red line shows the buffet onset data from the Fokker report [2] and the blue lines in Figures 4.6 and 4.7 represent a run of respectively 5, 10, 20 and 50 buffet onset points. From the results it becomes visible for example a spline method is not to be used to connect the data points in a smooth way. This is because of the shark tooth like behavior influences the spline line segments between two points drastically, resulting in a line that does not represent the buffet onset boundary in a reasonable way. It is chosen not to use a curve fitting method at this point.[1]

First, TSFOIL is ran in combination with the limiting Mach number separation criterion. The minimum Mach number which could be achieved in combination with an relatively high lift coefficient (or angle of attack) was about $M_\infty \approx 0.64$. Any buffet onset points with a lower Mach number and higher angle of attack or lift coefficient resulted in corrupted results, as the zigzag profile got exponentially worse. The local Mach number separation criterion runs show two issues; both an incapability to compute buffet at high C_L values, and a large offset in C_L sense. These results are discarded since it is very unlikely even a better 3-dimensional $M_\infty - \alpha$ to $M_\infty - C_L$ transformation would shift the wing lift coefficients down by a factor 2.

Next the second TSFOIL option is explored using the critical pressure rise separation criterion. These runs show a better approximation of the linear high transonic part of the buffet onset diagram. The C_L offset visible in Figure 4.6 is not present anymore, but still the end points are producing incorrect results. This zigzag pattern increases with an increasing number of buffet points.

4.2.3 MSES Results

The second option for the 2-dimensional flow solver is to use MSES instead of TSFOIL together with the critical pressure rise separation criterion. The results of the runs with 5,10,20 and 50 data points are shown in Table 4.4. The accompanying figures are shown in Figure 4.8. Again, the blue lines in Figure 4.8 represent a run of respectively 5, 10, 20 and 50 buffet onset points. Only the critical pressure rise separation criterion is used, for reasons mentioned in the introduction of this chapter. It clearly shows the MSES results

[1] All the runs are performed on a high end 2009 laptop with an Intel Core 2 Duo T6500, 2.1 GHz 4.0 GB DDR2 SDRAM - 800.0 MHz.

are more in line with the (red line) data from the Fokker report at high C_L values, but incorrect at low C_L values and high Mach numbers. The interval in which the pressure distribution can be determined correctly is increased significantly with respect to the $M \approx 0.64$ shown in the TSFOIL results. The zigzag profile at the and left end of the buffet onset boundary is not visible any more in the MSES runs, but a strange profile with outlier values around the lower regions of the buffet onset diagram still occurs. Figures 4.9a and 4.9b show only the points of interest without the incorrect outliers in the high Mach number regime above $M_\infty \approx 0.75$. [2]

A distinction has to be made between $\alpha_{2D} < 0°$ and $\alpha_{2D} > 0°$. In the case of negative angles of attack, the bottom side of the profile will show a suction peak and at positive angles of attack the top side will show the suction peak. The developed buffet onset prediction tool uses the largest pressure rise on both bottom or top side, to incorporate both cases. This seems in line with Mach number divergence figures from [5] as the bottom side of the airfoil is critical with respect to Mach divergence at low C_L values.

4.2.4 Matrix-V Results

Since the final step in the buffet prediction tool, the wing lift coefficient determination by AVL, is somewhat doubtful (especially at transonic conditions) a more complex code is used to translate the angle of attack values at certain Mach numbers to a wing lift coefficient in order to assess the influence and accuracy of the final step in the buffet prediction tool. Since the TSFOIL results in combination with the local Mach number separation criterion do not show a reliable result due to the fact the offset in terms of C_L is large, and the low transonic Mach numbers in combination with high wing lift coefficients cannot be modeled and using the critical pressure rise separation criterion only solves one of these problems (the C_L offset to some extent, but still the domain is limited to $M_\infty \approx 0.64$ and up) the MSES results qualify for further investigation.

The program used for this is called Matrix-V. This Matrix-V code uses the intermediate results, $M_\infty - \alpha$ of the MSES simulation from previous paragraph. The intermediate results are listed in Table 4.5 together with the AVL C_L and Matrix-V C_L results. The Matrix-V code was ran for the 12 reliable points from the 20 point MSES run. The total run time to compute these 12 wing lift coefficients was 55 minutes, or approximately 3300 seconds.

The results from the Matrix-V run are plotted on the data from the Fokker report and with respect to the MSES run in Figure 4.9a and in more detail in Figure 4.9b. Since Matrix-V is a full conservative, full potential code with boundary layer, it solves viscid and inviscid flow together and needs to converge to a solution. The last three values in Table 4.5 unfortunately do not converge to a solution in Matrix-V, probably because of the high angle of attack and high resulting lift coefficient. However, It shows the Matrix-V result shift the computed buffet onset boundary downwards towards the literature line. This indicates it is an improvement with respect to the AVL runs used in the tool developed.

[2] All MSES runs are ran on a fine grid with 100 Newton iterations per run

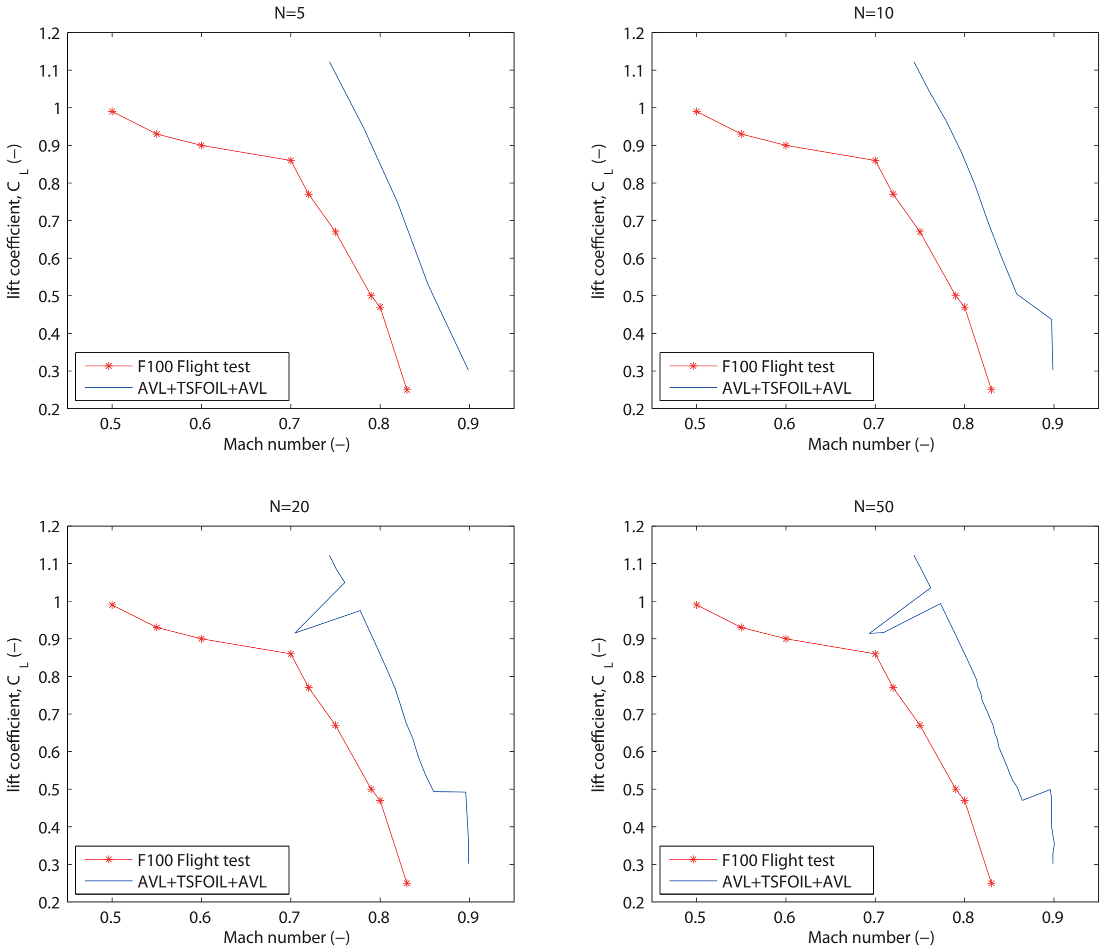

Figure 4.6: Buffet onset of Fokker 100 wing-fuselage combination, TSFOIL and M_{local} separation criterion

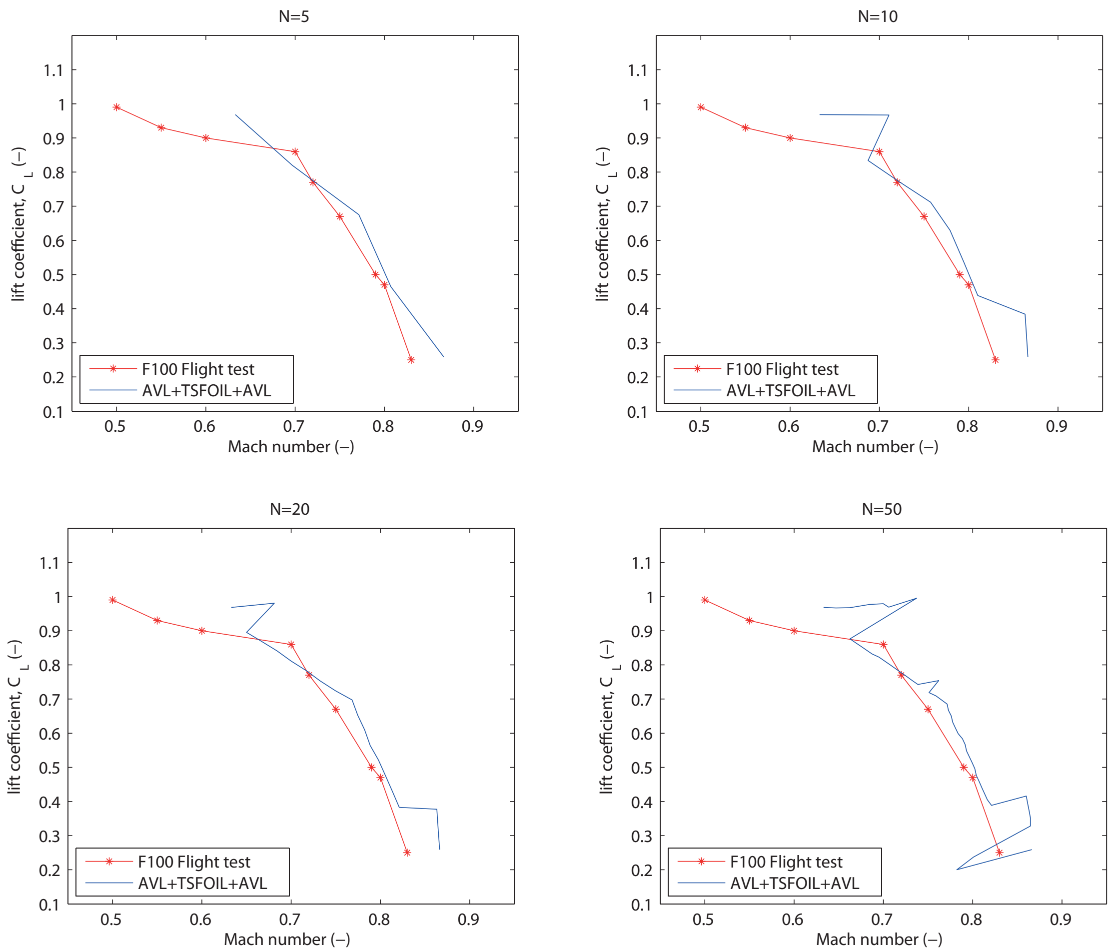

Figure 4.7: Buffet onset of Fokker 100 wing-fuselage combination, TSFOIL and ΔC_p separation criterion

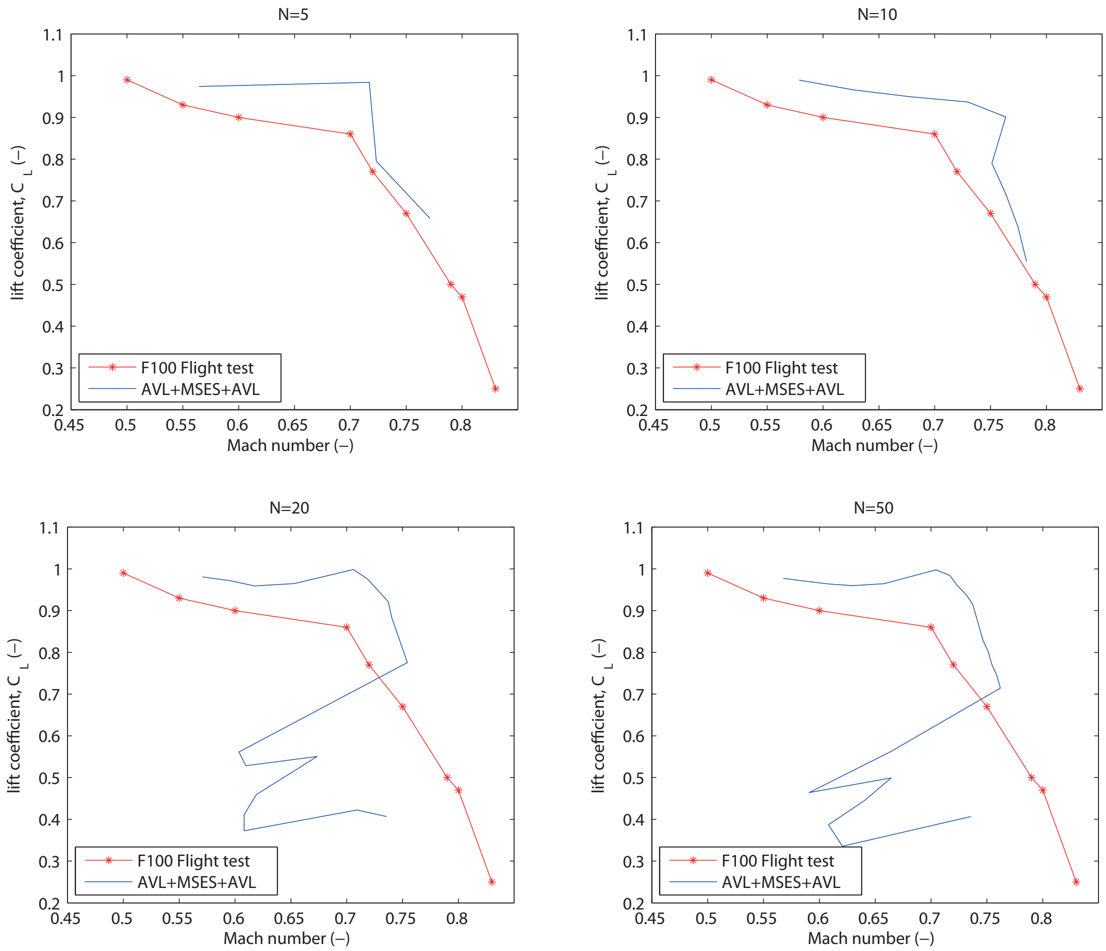

Figure 4.8: Buffet onset of Fokker 100 wing-fuselage combination, MSES and ΔC_p separation criterion

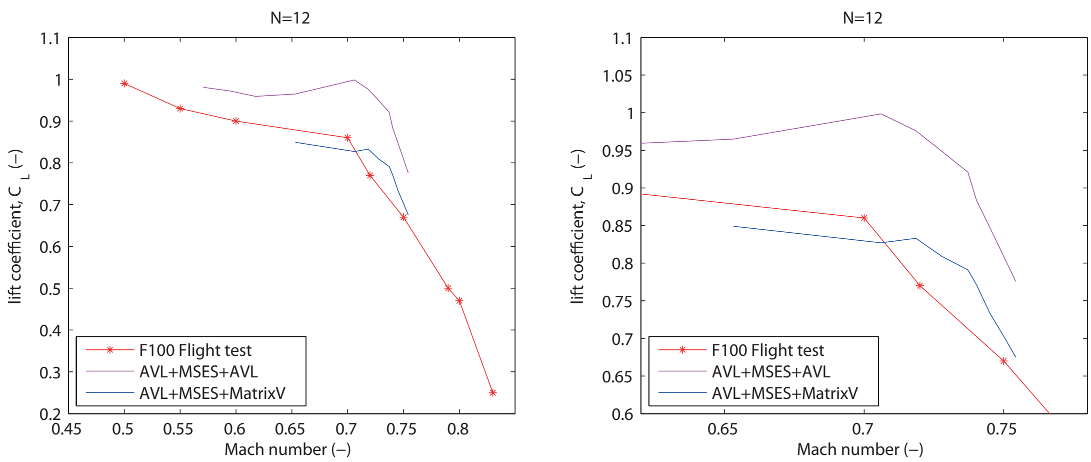

Figure 4.9: Buffet onset of Fokker 100 wing-fuselage combination, literature versus MSES intermediate results and Matrix-V run, number = 12, ΔC_P separation criterion

Table 4.4: Simulation results for F100, $\Lambda_{0.5c}$ at $Re \approx 1.5 \cdot 10^7$

separation criteria	no. points	time $[sec]$
TSFOIL and pressure jump	5	71
	10	141
	20	259
	50	692
TSFOIL and local Mach number	5	99
	10	193
	20	367
	50	944
MSES and pressure Jump	5	492
	10	1083
	20	1750
	50	4738

Table 4.5: 3-dimensional M_∞ and α from MSES and ΔC_p separation criteria, $C_{L_{\mathrm{AVL}}}$ and $C_{L_{\mathrm{MatV}}}$

Simulation	$M_\infty[-]$	$\alpha[deg]$	$C_{L_{\mathrm{AVL}}}[-]$	$C_{L_{\mathrm{MatV}}}[-]$
MSES and	0.754	2.91	0.776	0.675
pressure jump	0.750	3.24	0.812	0.705
	0.745	3.57	0.848	0.734
	0.740	3.90	0.883	0.771
	0.737	4.23	0.921	0.791
	0.728	4.54	0.949	0.809
	0.719	4.84	0.976	0.833
	0.706	5.13	0.998	0.849
	0.653	5.22	0.965	0.827
	0.617	5.40	0.959	-
	0.596	5.64	0.971	-
	0.571	5.87	0.981	-

4.3 Reflection

To reflect on these results the same approach will be used as in the beginning of this chapter. First the results of the TSFOIL runs will be adressed, after which the use of MSES and Matrix-V will be discussed. To interpret these results, one can compare them to a more high end simulation, windtunnel-, or flight test data. A report from Fokker [2] provides this data.

4.3.1 2-dimensional Euler versus Transonic Small Disturbance

It shows the 2-dimensional Euler code approximates the buffet onset quite accurate in the high C_L and low Mach number region. The transonic small disturbance code TSFOIL shows acceptable results when combined with the critical pressure rise separation criterion, but only in the low C_L and high transonic Mach number region. It cannot handle the region left of the coffin corner, which is an important part of the buffet envelope. Using MSES a broader bandwidth of buffet onset can be predicted in the transonic regime, when compared to TSFOIL. This is without a doubt an advantage when designing a wing or aircraft over the complete $M - C_L$ envelope.

When interested in the high transonic buffet onset of a certain wing-fuselage combination, say the linear part of the buffet onset in the case of the Fokker 100, a TSFOIL simulation with 10 or 20 data points can give a reasonable indication of the limiting C_L values at certain high freestream Mach numbers. This way a quick estimate can be made whether the performance calculations made will be degraded by buffet onset or not, since the computation time limited to 3-4 minutes.

It has to be noted all the results, both MSES and TSFOIL show the same begin and end buffet onset point, independent of the number of buffet points (5,10,20 or 50). This indicates in the bisection method the coefficients $C1, C2$ and $\Delta C2$ are implemented correctly to divide the interval into smaller sections instead of adding points to the right or left. In other words, the red lines on which the bisection method is executed are spaced closer together when the number of buffet onset points increase, but the interval between the first and last line (minimal and maximal value of C_2) remains constant.

Considering the outliers in the TSFOIL runs and in the MSES runs (at low wing lift coefficient - high Mach number combinations) a problem arises. The high M_∞ low C_L data points are, in the 2-dimensional case, the points with a negative angle of attack. Further research revealed the incorrect data points start exactly when the 2-dimensional airfoil is placed under a negative angle of attack. This negative angle of attack, and the stagnation point shifting upwards on the airfoil might lead to problems in the MSES grid making process. To investigate this, the pressure distribution over the airfoil at one of these high Mach, low C_L points is shown in Figure 4.10. The pressure distribution of this airfoil shows a suction peak at the bottom of the airfoil instead of the top side. In the tool developed in this thesis work both the upper side and lower side are included, so this should pose no problem.

The main cause of this problem is most probably the fact the linear relation between the freestream Mach number and angle of attack which describes a straight bisection line as can be seen in Chapter 3, $\alpha = C_1 \cdot M_\infty + C_2$, has a positive slope. When at negative angles of attack separation is detected, the Mach number decreases due to the lower interval chosen by the bisection method, which automatically makes α even more negative. This is undesirable, since α should increase ($\alpha \to 0$). Or even better, $\alpha \to \alpha_0$.

Problem with reversing the bisection lines slope when $\alpha < 0$ is that also at higher, positive α values, the bisection method might run into a negative angles of attack somewhere along its bisection track. This makes implementing a simple $if - else$ statement with respect to the orientation of the bisection lines in Matlab more complex. What could be done, is setting the slope of the bisection lines $C_1 = 0$ to eliminate the Mach number dependency of α. These horizontal bisection lines however caused problems in the upper C_L part of the buffet onset boundary because the values are more or less on a straight line at that point and a non-unique solution could occur. In addition a test with this change did not solve the problem in a correct way at low C_L values. Running the tool once with a positive C_1 and once with $C_1 < 0$ and neglecting the 'bad' half of the data, might result in a more complete buffet onset boundary, but further research is required to solve this problem in a decent way.

Another reason for this might be the separation criterion from literature is not applicable at the shocks induced at the lower side of the airfoil. Making the bisection method lines dynamic within the iterations should already be a good improvement. It is important to solve this issue, because 2-dimensional negative angles of attack are very likely to occur, especially with wings having a downward twist angle towards the tip. The more the highest loaded section $\eta_{\max}$ under investigation lies outboard, the higher the twist downwards will probably be, the more data points will have a negative angle of attack during the bisection method.

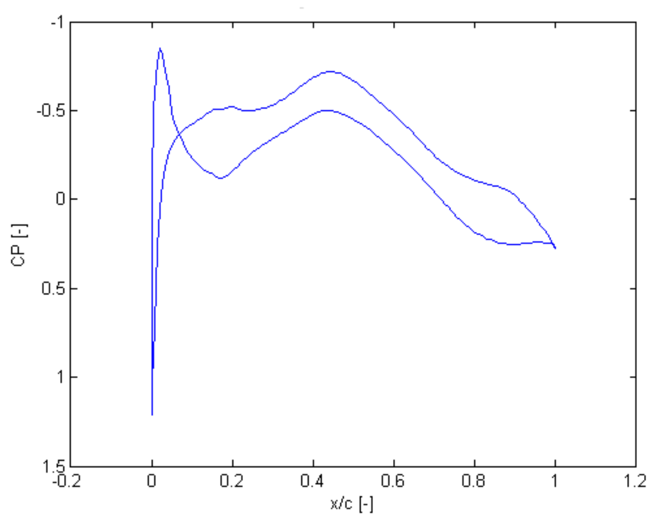

Figure 4.10: Pressure distribution over highest loaded section at $M_\infty = 0.70$, $\alpha = -1.0°$

4.3.2 Separation Criteria

Considering the two different separation criteria used a clear difference can be seen in the TSFOIL results. The limiting local Mach number separation criterion seems to have a certain off-set with respect to the buffet onset data from the Fokker report, but considering the runs at different numbers of buffet onset points (5,10,20 and 50) the lines are almost identical, except for the end points. This strange behavior at the end points of the buffet onset boundary is also visible in the figure from the TSFOIL and pressure jump combination. At high α and Mach number the end points show a strange alternating shark tooth like profile. This profile gets more pronounced with increasing number of buffet onset points. This could be caused because in the transonic small disturbance model the computed pressure distribution is incorrect at high angles of attack or freestream Mach numbers, resulting in a erroneous jump in pressure coefficient ΔC_P in terms of magnitude and position. In other words, the shock position and strength is incorrect. Consequently, the bisection method might select the wrong interval somewhere along its way. However, the later the wrong interval is chosen, the smaller the influence on the final value. So if for example at the 7th or 8th iteration this problem occurs, the wrong side of the bisection interval might result in a strange alternating value in the buffet onset data. An incorrect first or second interval would result in a very large incorrect value.

Different solutions to solve this strange alternating behavior in the TSFOIL results were investigated, such as increasing the bisection interval or increasing the bisection stop criteria from 10 to 20 iterations. Both did not work, and only increased the computational time. Although increasing the number of iterations decreases the maximum error made, this is not significant because the maximum error with 10 bisection iterations is already sufficiently small(as can be seen in Equation 3.25 in Chapter 3). Following the same logic, increasing the first bisection interval increases the maximal potential error, but this also made no significant difference in output.

Looking at the off-set of the local Mach number separation criterion case in terms of C_L, this could be due to the use of AVL for computing the wing lift coefficient when transforming the $M_\infty - \alpha$ values in to $M_\infty - C_L$. If this is the case, this should be visible in the results of a Matrix-V run using TSFOIL intermediate data instead of MSES data, although it is highly unlikely the TSFOIL and M_{local} separation criterion will prove to be correct when evaluating the C_L values more accurate, because a shift of a factor two will most probably not occur, as demonstrated in the MSES + Matrix-V case.

4.3.3 Matrix-V versus AVL

The results from the Matrix-V run are plotted on the data from the Fokker report and with respect to the MSES run in figure 4.9a. It shows the Matrix-V result shift the computed buffet onset boundary downwards towards the literature line. It is clearly visible AVL over predicts the wing lift coefficient This indicates it is an improvement with respect to the AVL runs used in the tool developed. To quantify the error made in the wing lift coefficient determination the ΔC_L is determined between the (interpolated) literature data and the Matrix-V run as shown in figure 4.9a. The Matrix-V run over-, and under predicts the wing lift coefficient in the region $0.65 < M_\infty < 0.75$ with an

Table 4.6: ΔC_L for literature and Matrix-V results, Fokker 100 wing, $\Lambda_{0.5c}$ at $Re \approx 1.5 \cdot 10^7$

M_∞	$C_{L_{Lit}}[-]$	$C_{L_{MatV}}[-]$	$\Delta C_L[-]$
0.75	0.68	0.71	-0.03
0.73	0.72	0.81	-0.09
0.70	0.87	0.85	0.02
0.68	0.86	0.84	0.02
0.65	0.86	0.83	0.03

intersection at approximately $M_\infty = 0.72$. The error bandwidth is shown in table 4.6. If compared to the empirical method by Isikveren [1], which concludes a margin of error of $\Delta \approx 0.026$ is possible, this is of the same order of magnitude. The advantage of using a numerical method is the use of reference data (or seed aircraft) is not needed, and random (unconventional) wing geometries can be investigated as well.

4.3.4 Computational Time

Plotting the computational time for both the TSFOIL and MSES case, shows the following result as can be seen in Figure 4.11. In this figure, the numbers 1,2,3 and 4 on the horizontal axis represent the four cases of respectively 5,10,20 and 50 buffet onset points. The blue bar is the TSFOIL simulation with pressure jump separation criterion, the green bar is the TSFOIL simulation with the local Mach number separation criterion, and the red bar is the MSES simulation with the pressure jump separation criterion. It is clearly visible the computational time increases, which is to be expected with an increase in data points. However, there is a difference in computational time within the TSFOIL simulation case between the two separation criteria. This is rather unexpected, since the math involved in comparing a measured value to a reference value (being a local Mach number or pressure jump) is essentially the same operation. Since the number of bisection iterations is the same for both (10 times for each buffet point) this cannot be the reason for this difference. It might be the bisection intervals chosen by the local Mach number separation criteria end up at certain $M_\infty - \alpha$ combinations that have some trouble in computing a solution for the flow by TSFOIL. An overview of the various results is presented in Table 4.7.

When for example Matrix-V would be used to compute the entire buffet onset boundary, at 5 minutes per data point, 20 points (each using 10 bisection iterations) would already result in a computation time of $2 \cdot 10 \cdot 20 = 1000$ minutes, being 60000 seconds. A 20 point MSES run, including a Matrix-V run to improve the accuracy of the wing lift coefficient calculation, would take $1750 + 3300 = 5050$ seconds. The reduction in computation time would in that case be over 90%, which is substantial. it has to be noted in the case of a Matrix-V only run, a different separation criterion in Matrix-V will be used. Matrix-V uses a separation criterion based on the shape factor of the boundary layer and the cross-flow angle between the viscid boundary layer velocity vector and the inviscid flow vector.

One has to see the computational times in Table 4.7 in the right perspective. 25 minutes might seem like a long time to compute a buffet onset boundary, but if the total time

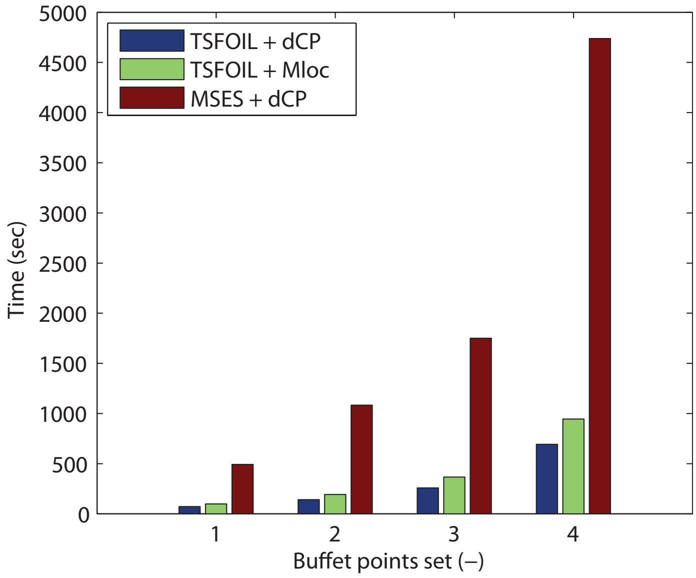

Figure 4.11: TSFOIL and MSES Computational time for 5,10,20 and 50 buffet onset points

used by a multi model generator or other design environment is in the order of hours, this might not be an issue. Furthermore, the buffet onset prediction module could be ran parallel with other tools to reduce this problem.

4.3.5 Chauvenet's Criterion for Outliers

To determine the best number of buffet onset points use when predicting the transonic buffet onset boundary, one would like to use some sort criterion in the post-processing process to determine the outliers in the dataset. This way, these values can be discarded, and for example a polynomial or using a least squares solution can be fitted in the remaining points. One of the criterions that could be used is Chauvenet's criterion. This criterion helps to assess whether a data point from a set of observations, is likely to be an outlier. It is based on the mean and standard deviation of the buffet onset data, and based on how much the data point under consideration to be deleted differs from the mean, it uses the normal distribution function to determine the probability that a given data point will be at the value of the suspect data point. When this probability is multiplied by the number of data points taken, and the result is less than 0.5, the suspicious data point may be discarded [37]. This criterion restricts the minimum number of buffet onset points required, since fitting for example a third order polynomial in 5 data points with two outliers is undesirable and in some cases even impossible.

Table 4.7: TSFOIL and MSES results for Fokker 100 wing, $\Lambda_{0.5c}$ at $Re \approx 1.5 \cdot 10^7$

separation criteria	no. points	time [sec]
TSFOIL and pressure jump	5	71
	10	141
	20	259
	50	692
TSFOIL and local Mach number	5	99
	10	193
	20	367
	50	944
MSES and pressure Jump	5	492
	10	1083
	20	1750
	50	4738

Chapter 5

Conclusions and Recommendations

In the previous chapter the results of the buffet onset prediction for the Fokker 100 wing-fuselage combination have been presented. The two different 2-dimensional simulation programs and two separation criteria available were combined to be able to decide the best way of predicting transonic buffet onset with respect to number of buffet points, accuracy, bandwidth, and computational time. In this chapter conclusions are derived from the results of the buffet prediction tool developed described in the Chapter 4. It will propose a recommended combination of external analyses tools and settings with respect to the use of the 2-dimensional TSFOIL or MSES program, the separation criterion and the optimal number of buffet points to use. Furthermore some recommendations will be given on further research and use of the buffet prediction tool, and a comparison will be made with respect to the performance of this tool and conventional buffet onset prediction methods.

5.1 Conclusions

The main goal of this thesis was to create a modular transonic buffet onset prediction tool which is fast and reliable. This is successfully done with help of a Vortex-Lattice method, 2-dimensional Euler code and Matrix-V code. It is 90% faster with respect to the use of only a Matrix-V code and it produces accurate results in the region left of the coffin corner, at high C_L low M_∞ combinations. Whether it is also reliable in the high transonic regime, has to be investigated during further research. The expected error is in the order of $\Delta C_L = 0.05$ which is in the same order as the error bandwidth presented in a semi-empirical method of Isikveren [1].

It can be concluded buffet is likely to originate at the wing section at which the local lift coefficient is maximal, neglecting the effect of aft loading. Aft loading causes an increase in lift, but no increase on the magnitude of the suction peak over the upper surface of the airfoil, so the ΔC_P remains the same. This way, the highest loaded section does not necessarily have to be the section with the highest suction peak. The wing sweep is of significant influence on the buffet onset boundary, as is the wing twist and incidence angle. The wing dihedral is neglected because the cosine of the wing dihedral angle is ≈ 1 for small dihedral angles. Modelling the fuselage in addition to the wing to account for the wing-fuselage interaction during the first AVL run did not prove to be of any influence. The wing-fuselage effect is not visible in the local lift coefficient distribution.

The separation criterion to be used is the critical pressure rise separation criterion, which produces better result compared to the limiting local Mach number separation criterion in the TSFOIL results. The MSES results only use the critical pressure rise separation criterion. It is recommended to specify 20 points on the buffet onset curve, and use the 2-dimensional Euler code MSES as 2-dimensional solver. By using 20 data points on the buffet onset curve, it will be possible during post-processing to determine the outliers in the dataset and still end up with enough points to plot a decent buffet onset boundary by using a polynomial or least squares solution to be fitted in the remaining set of data points. One of the criteria which could be used is Chauvenet's criterion. It is advisable to use the intermediate results of the buffet onset prediction method developed, being the $M_\infty - \alpha$ buffet onset data, and discard the last AVL step at which the wing lift coefficient is determined. Instead, one should use Matrix-V to predict the wing lift coefficients. This ensures a more accurate estimation of the wing lift coefficient, at the cost of about an hour more computation time in the 20 data point case. Using Matrix-V instead of AVL, the reduction in computational time between the developed tool with respect to the use of only a 3-dimensional code such as Matrix-V is still expected to be about 90%. When for example Matrix-V would be used to compute the entire buffet onset boundary, at 5 minutes per data point, 20 points (each using 10 bisection iterations) this would result in a computation time of $5 \cdot 10 \cdot 20 = 1000$ minutes, being 60000 seconds. A 20 point MSES run, including a final Matrix-V run to improve the accuracy of the wing lift coefficient calculation, would take $1750 + 3300 = 5050$ seconds.

5.2 Recommendations

The recommendations with respect to further research and use of this buffet onset prediction tool are structured in a similar manner as the rest of this thesis, and follows the logical flow presented in Chapter 3. From the geometrical input, addressing the AVL run, 2-dimensional solver and separation criteria, airfoil interpolation method, wing lift coefficient determination all the way down to the final $M_\infty - C_L$ output. The steps taken and assumptions made in developing the buffet prediction methodology are made with great care and good motivation, but there is always room for improvement.

5.2.1 Geometrical Input

Starting at the geometrical input, in the files with airfoil coordinates the number of data points and format can cause problems. When too little number of airfoil coordinates are specified, the airfoil interpolation routine results in a moderately smooth airfoil, which causes problems in determining the C_p distribution. The input incidence angles per wing segment or airfoil used in Chapter 4 to demonstrate the program developed, are in Jig conditions. It could be better to use the incidence angles under $1-g$ conditions instead, since this is closer to reality when flying in the buffet regime. Since this data was not at hand, the Jig values are used instead. The effect of $1-g$ loading on the twist angle will be the negative twist at the tip will increasing (become more negative) with an increasing load factor. In that respect, it might even be even better to use the twist angles at $n = 1.3$ conditions because this is the factor used in the operational regulations regarding buffet. In that case, depending on instantaneous weight, this will cause a certain amount of wing bending. The question is whether the influence of that wing bending on the aerodynamic twist will create a situation which is better or worse than the Jig codition case, from a buffet point of view. Furthermore, the unknown wing sweep angles and airfoil chord are computed using linear interpolation between the known values at the root, kink and tip. An additional error could be introduced by doing this.

5.2.2 Highest loaded section

Looking at the AVL run, executed to determine the section at which buffet is likely to originate, it is assumed buffet originates at the highest loaded section of the wing. This assumption could be incorrect. This is due to the addition of aft loading. Aft loading causes an increase in lift, but no increase on the magnitude of the suction peak over the upper surface of the airfoil, so the ΔC_P remains the same. This way, the highest loaded section does not necessarily have to be the section with the highest suction peak. In addition, the influence of other wing objects such as control surfaces, wing fences, spoilers, LE and TE high lift devices, nacelles, engines and other objects could be further investigated. Since these objects can influence the location of the highest loaded section, wing geometry, pressure distribution, boundary layer thickness, shape factor and so on, it could influence the buffet onset boundary of the wing-fuselage combination investigated.

Next step in the buffet prediction tool is the construction of the airfoil contour of the highest loaded wing section. Looking at the airfoil interpolation method developed in this thesis, a better result can be obtained when taking the derivative of the contour in to account when averaging. This means a smoother airfoil will most probably be achieved when using for example 4 neighbouring points instead of 2. One has to account for an extra set of boundary conditions, to make sure the leading and trailing edge are represented correctly.

5.2.3 2-dimensional Solver

There is a broad spectrum of tools that can be used in the 2-dimensional airfoil simulation part of this program. After a trade-off found in Chapter 2, both TSFOIL and MSES were selected. Instead of TSFOIL or MSES one could use another flow solver, for instance VGK or even a 2-dimensional RANS code. One has to keep in mind the computational time aspect of using such a program. Downside of using for example RANS is turbulence modelling, which is computationally expensive and could involve (very) complex turbulence models. However, it could eliminate the problem of convergence between the viscid and inviscid calculations done by MSES. The tool developed is easily extended with a third 2-dimensional flow solver, as long as the input and output handling is done in a correct way, which is different for each (off the shelf) program used.

TSFOIL Limitations

In Chapter 3 the TSFOIL program was introduced. It was already mentioned the angle of attack should not be to large, and is limited from $\alpha \in [-9°, 9°]$. In terms of freestream Mach number the flow should have $M_\infty \in [0.5, 2]$, and $\neq 1$. These requirements posed no problem for the demonstration case of the Fokker 100, since the freestream Mach number will not exceed 0.9 and the angle of attack does not exceed 9. Although, because the local Mach number could exceed $M_{local} = 1.3$ in some cases during the bisection method, TSFOIL sends a warning the pressure jump over the shock becomes so large, the resulting strength and location of the shock may be incorrect. In other words, the pressure distribution calculated could contain errors. In case this happens during a bisection run at high Mach number where separation is expected, this is not a problem. The bisection method assumes separation when TSFOIL produces this error. This might result in a somewhat conservative buffet onset boundary, and some problems during the bisection method at the end points of the buffet onset line.

Considering the zigzag profile at the end points of the TSFOIL simulations, it might be possible the problem is double valued at certain points, meaning there are two possible solutions to a certain flow condition. This could interfere with the bisection method is such a way, an incorrect data point results. This should be investigated during further research.

MSES Limitations

Since the MSES code was altered for use in this research, this could be done again to add the option to save the local Mach number in front of the shock to a file, and not only the C_p distribution as is the case at this moment. This is the reason only one separation criterion can be used at the moment when simulating the flow over the airfoil of the highest loaded section using MSES. Since MSES is open source, the Fortran code could be altered to accomplish this for use in further research. It would be advisable to create a function to write an output file for MSES that contains all data at hand (C_p distribution, boundary layer thickness, shape factor and so on) so every user can filter this data to his own use.

In addition, MSES is set to use 100 iterations to converge (on a fine grid) at each $Mach-\alpha$ combination run, but one could increase this number to for example 200. This would increase computation time, but produces more accurate results. One could also choose to simulate first 50 iterations on a coarse grid, after which e.g. 50 or 100 iterations are done on a fine grid. This could make the solution of one MSES run converge faster. The right balance might be different for different types of airfoils, but is worth investigating further.

Furthermore special care has to be taken when constructing the input file for MSES, containing the settings on the flow analyses mode, critical Mach number and dissipation weight factor. The artificial dissipation in MSES, as discussed in Chapter 3 section on upwind discretization, is analogous to bulk viscosity (also called volume viscosity or second viscosity). This viscosity becomes important when compressibility plays an important role, which off course is the case when dealing with shockwaves. The reason a critical Mach number M_{crit} and dissipation weight factor scaling coefficient C_{μ} are introduced, is to provide a user-adjustable margin when using MSES [34]. Since both M_{crit} and C_{μ} have an effect on the total dissipation level, which in turn can produce numerical instability at certain pressure jumps occurring when shockwaves are present, it is essential these parameters are set correctly. It could be the shock is 'smeared out' over a too large area due to this artificial viscosity, resulting in an incorrect C_p jump. In other words, the shock is not captured correctly, and this way the bisection method might select the wrong interval resulting in an incorrect buffet onset Mach number. The MSES manual [34] suggest $M_{crit} = 0.99$ and $C_{\mu} = 1.0$ for most cases, but $M_{crit} = 0.90$ and $C_{\mu} = 1.2$ for strong shocks. Since the magnitude of the pressure rise (shock strength) varies significantly during the iterations done in the bisection method, it is hard to estimate the most appropriate values for these parameters during each run. It could be this produces some issues when using MSES, resulting in incorrect pressure distributions over the airfoil when the pressure jumps become relatively large.

Surface Curvature Effects

On transonic airfoils and wings, the surface underneath the interaction is expected to show some concave or convex curvature instead of being flat. The freestream Mach number M_{∞} in front of the shock is also not constant, but changes with distance from the surface. It can be assumed this interaction region is much smaller than the size of the airfoil, and the surface curvature in the shock region is also limited. However, surface curvature does have an impact on the pressure and velocity profile over the airfoil, and thus affect separation and buffet onset. The first one is positive in terms of buffet onset; the shock wave strength or pressure jump required to induce separation tends to be larger for a curved surface than for a flat one. In a paper by Pearcey [18] it was suggested this was because convex curvature would cause a streamwise decrease in pressure that reduces the adverse pressure gradient a little bit. This way, the boundary layer can stay attached for a little longer, postponing separation. Though the effect of this curvature on separation postponement is relatively small. Another effect of surface curvature which is more significant is the fact that convex curvature tend to accelerate the flow (causing larger overspeeds) making secondary supersonic flow regions of the flow possible, and likely to increase in size. This is an unwanted effect, which most probably does not improve buffet onset characteristics. This indicates a transonic wing should be designed such that the shock waves are likely to occur on parts of the airfoil surface with relatively low curvature [18].

5.2.4 Different Separation Criteria

Because of the modular way this tool is built, adding a different component is relatively easy from a programming point of view. One could investigate different separation criteria to be used in the future, other than the two discussed in this thesis. The pressure jump and local Mach number across and before the shock location are by far not the only two separation criteria one can think of. For example a simple minimum pressure coefficient $C_{p_{min}}$ criterion, instead of a pressure jump ΔC_P criterion could be investigated. Loftin's criterion might also be worth investigating, since it states that the maximum value of the canonical pressure coefficient C_p' after the start of recovery is 0.88 [6]. Another pressure distribution based criterion which could be used is Stratford's limiting pressure distribution to find separation over a certain airfoil as a function of the minimum pressure coefficient. Stratford's criterion may be used to compute the shape of the pressure distribution that is everywhere on the edge of separation.

When a boundary layer is on the verge of separation, a parameter that plays an important role is the skin friction coefficient C_f. Based on research done by Zheltovodov [18] a critical pressure rise for separation is given by equation 5.1. In this equation, the parameter k is a dimensionless factor. Several values for k are found in literature, and $k = 6$ is a value which is used in various cases. To use this criteria, a relation between the skin friction coefficient C_f and for example the Reynolds number and freestream Mach number M_∞ should be determined.

$$\frac{p}{p_\infty} = 1 + kM_\infty^2 \frac{\sqrt{C_f}}{(M_\infty^2 - 1)^{\frac{1}{4}}} \tag{5.1}$$

Perhaps one of the most reliable separation criteria based on the computed boundary layer quantities will be the shape factor H of the boundary layer, as is used by the 3-dimensional Matrix-V method. Since the shock wave boundary layer interaction can influence the velocity profile, and thus induce reversed flow, which influences the skin friction coefficient C_f and shear stress τ, this could indicate separation. The higher the value of H the stronger the adverse pressure gradient [6] Since MSES is capable of plotting the shape factor, it can also be re-programmed to write this to an output file. This is the case for multiple parameters that could be used for different separation criteria, as is discussed in the section below on the limitations of MSES. In addition, the crossflow criterion as used by Matrix-V could also be implemented in this tool, only the crossflow angle needs to be computed with the output data generated by MSES.

5.2.5 Reynolds Effects at high Mach Numbers

Reynolds number effects can be much more substantial at transonic flow conditions compared to subsonic flight. This is caused by the following effects:

1. Transition point further ahead of shockwave
2. Increase of flow curvature

The boundary layer may be laminar up to the shock at low Reynolds numbers, but with increasing Reynolds number the boundary layer thickness decreases and transition will occur further ahead of the shock. Also, an increasing Reynolds number, and thus decreasing boundary layer displacement thickness effectively increases the flow curvature near the surface of the airfoil. This could result in a different shock wave position and shock strength, influencing the flow and separation characteristics, and thus buffet onset boundary of the airfoil [5]. However, when the transition point is fixed in for example the MSES simulation, as was the case during this thesis research, this effect is not taken into account. Only when free transition is possible, MSES determines the transition point at the cost of extra computation time.

5.2.6 Wing Lift Coefficient Prediction

Because AVL is used to evaluate the total wing lift coefficient at buffet onset conditions, results have to be treated with care. It is recommended to implement another 3-dimensional method to translate the $M_\infty - \alpha$ result to $M_\infty - C_L$ results. In this thesis research the AVL program is used to do this, but since this is a simple Vortex Lattice method, a 3-dimensional Euler model results in more accurate C_L values, improving the overall buffet onset results.

In addition, a better computation of the wing planform area, or reference area S_{ref}, for example by the separate calculation of the planform area of each wing trunk, and summing these values to arrive at the total wing planform area, would improve the c_l and C_L calculation to some extent, but is not expected to have a large influence on the result published in this thesis.

5.2.7 Various 3-dimensional Effects

Sweep Effects

Crossflow induced by a sweep angle of the wing might induce separation somewhat earlier. Research [18] shows that swept shock waves separate once the normal component of the freestream Mach number increased beyond 1.2. This could also be an interesting point of research with respect to creating a new set of separation criteria.

Control Surfaces and High Lift Devices

Trailing and leading edge devices can also influence the pressure distribution on the wing airfoils, and thus influence the buffet onset boundary of a certain wing. LE and TE devices aim to increase the maximum lift coefficient of a wing at take-off and landing. Three effects determine the increase of these devices, being:

1. Increase in camber
2. Increase in chord
3. Slot effect

In short, trailing edge flaps shift the $C_L - \alpha$ curve up, and leading edge devices extend the $C_L - \alpha$ curve. The presence of a LE devices can also suppress the suction peak of the main wing, so the adverse pressure gradient is less steep. This postpones separation, and allows for larger angles of attack. The effect of a slot between the elements of the wing, creates a thinner, fresh and energized boundary layer on the following element, which is also beneficial from a separation point of view. The downwash of the leading element in addition lowers the effective angle of attack for the trailing element. This also aids in achieving higher angles of attack [5]. Since high lift devices are generally not used during phases where transonic buffet can occur, they are not expected to have an influence on the buffet onset boundary. However, control surfaces are used in the transonic regime, and buffet is likely to occur during a e.g. a turning manoeuver. The presence of control surfaces, and their influence on the buffet onset boundary is neglected in this thesis research, but can be implemented since both AVL and MSES for example can perfectly cope with control surfaces and multi element airfoils.

If engines or nacelles are mounted close to, or in front of the wing, they might have some effect on the flow and boundary layer development over the main wing, and thus influence the buffet onset boundary. This was not the case for the Fokker 100, which was the only configuration investigated in this thesis work.

5.2.8 Programming Issues

During the prediction of the highest loaded section by AVL, it could occur the spanwise location found by AVL coincides with a location at which an airfoil is already defined by the geometrical input file. In this case, in which obviously no airfoil interpolation has to be done, the program will still computed an averaged airfoil with the help of the two surrounding airfoils. A conditional statement could be implemented skipping the airfoil interpolation routine if this situation occurs.

Next to correcting the bisection method to cope with negative angles of attack of the airfoil, the implementation of a criterion to select the incorrect outlying data points from the buffet onset determination (e.g. using Chauvenet's criterion) is something in the post processing that will aid in a smooth buffet onset diagram. Future research could implement a code to calculate α_0 of airfoil $\eta_{\max}$ to be used in this improved bisection method for negative angles of attack.

In addition an alternative to the bisection method could be used to arrive at the buffet onset points. This could speed up the whole process, if the right root finding method is used. The C_1 coefficient which determines the slope of the lines on which the bisection method operates, could be made variable. The bisection method works best when it is perpendicular to the function values. This means the optimal slope changes with the shape of the buffet onset boundary. Furthermore, if an educated guess can be made with respect to the lower and upper buffet onset Mach number, the bisection start interval could be made smaller, which decreases the maximal potential error made, and could decrease the stop criteria (number of bisection iterations) needed. Although for a general wing design it is hard to determine the smallest bisection start interval applicable.

In the various airfoil files used, the number of coordinates for the upper surface and lower surface should be equal. This can be changed with a routine that automatically searches for the end of the upper surface definition in the airfoil coordinate file, but at this moment the input is divided equally assuming the first half is upper side, and second half is lower side. The airfoil files used are required to have only the first line of the file as header. If more lines are used as header, the input will not be read correctly by Matlab, causing problems further on in the workflow of the model. Airfoil files have to be defined from TE towards LE and back from LE to TE (upper side first, then lower side).

With respect to further use of this tool, it is interesting to investigate how this transonic buffet prediction tool behaves when less conventional wing geometries are tested. For example a flying wing or blended wing body, or Prandtl plane. Possible the first AVL step has to be altered a little to cope with these geometries, but when the highest loaded section is determined, the program could run as normal. The results then could be an indicator of the transonic buffet characteristics of these unconventional, conceptual wing formations.

On a general note, to speed up the process one could think of using a parallel computing toolbox in Matlab to use a dual or quad core system and compute multiple bisection lines parallel to each other. This requires a somewhat different program architecture, but will most probably reduce computational time significantly.

References

[1] Askin T. Isikveren Andrien Berard. Conceptual design prediction of the buffet envelope of transport aircraft. *Journal of Aircraft*, 46:1593–1605, 2009.

[2] E. Obert. A data collection of the buffet onset boundaries of transport aircraft. Technical report, Fokker Aircraft B.V., 1991.

[3] Magali Dodemant. Internship report applied aerodynamics department. Technical report, Onera, 2006.

[4] Roelof Vos. Governing equations in transonic flow. Technical report, Delft University of Technology, 2008.

[5] E. Obert. Aerodynamic design and aircraft operation. Technical report, Delft University of Technology, 1989.

[6] L.L.M. Veldhuis. Aircraft aerodynamics primer. Technical report, Delft University of Technology, 2010.

[7] B.W. van Oudheusden. Ae4120 viscous flows lecture 6: Incompressible turbulent flow. Technical report, Delft University of Technology, 2011.

[8] Sadotoshi Taneda. An album of fluid motion. Technical report, Van Dyke, 1982.

[9] Keysmer Damo. Separation induced by shock waves. Technical report, Delft University of Technology, 2011.

[10] R.H. Lange C. Donaldson. Study of the pressure rise across shock waves required to separate laminar and turbulent boundary layers in supersonc flow. *UTIA*, 21:1–10, 1952.

[11] G.J.J. Ruijgrok. *Elements of Airplane Performance*. Delft University Press, 1994.

[12] David Nixon Goetz H. Klopfer. Nonisentropic potential formulation for transonic flows. *AIAA Journal*, 22:770–776, 1983.

[13] W.H. Mason. On the use of the potential flow model for aerodynamic design at transonic speeds. *AIAA Journal*, 1:1–7, 1995.

[14] European Aviation Safety Agency. Certification specifications for large aeroplanes cs-25. Technical report, European Aviation Safety Agency, 2010.

[15] R.L. Bisplinghoff. *Aeroelasticity*. Dover Science, 1996.

[16] J.D. Anderson. *Fundamentals of Aerodynamics*. Thomas E. Carson, 2001.

[17] Manuel D. Salas. The curious events leading to the theory of shock waves. Technical report, NASA Langley Research Center, 2006.

[18] John K. Harvey. *Shock Wave-Boundary-Layer Interactions*. Camebridge University Press, 2011.

[19] E.V. Laitone. Local supersonic region on a body moving at subsonic speeds. In *Symposium Transsonicum*, 1964.

[20] Edward Lan Jan Roskam, Chaun-Tau. *Airplane Aerodynamics and Performance*. DARcorp, 2008.

[21] P. Molton J.-C. Abart J. Dandois, V. Brunet. Buffet control by means of mechanical and fluidic vortex generators. *AIAA Journal*, 1:1–14, 2010.

[22] Ray Humble Paul Blinde. Effects of micro-ramps on a shock wave/turbulent boundary layer interaction. *AIAA Journal*, 1:508–522, 2009.

[23] M.I. Gerritsma. Computational fluid dynamics - incompressible flows. Technical report, Delft University of Technology, 2002.

[24] W. Andrew Keats. Two-dimensional anisotropic cartesian mesh adaptation for the compressible euler equations. Master's thesis, University of Waterloo, 2004.

[25] X. Huang J. Dudley. Multidisciplinary optimization of high-speed civil transport. *AIAA Journal*, 95:124, 1995.

[26] Visich M Siclari M.J. Shock fitting in conical supersonic full potential flows with entropy effects. *AIAA Journal*, 1:1–15, 1984.

[27] K. McGratten. Comparison of transonic flow models. *AIAA Journal*, 30:2340–2343, 1992.

[28] Terry Holst. An implicit algorithm for the conservation transonic full potential equation using an arbitrary mesh. *AIAA Journal*, 17:1038–1056, 1979.

[29] Lakshmi Sankar. The transonic small disturbance equation. Technical report, Georgia Institute of Technology, 2011.

[30] Paul Dorman. Study of the aerodynamics of a small uav using avl software. Technical report, Unknown, 2006.

[31] J.N.A. van Eijndhoven. Sensitivity of the lift-drag polar. Technical report, Delft University of Technology, 2010.

[32] David Marshall Kevin Lane. Inverse airfoil design utilizing cst parameterization. *AIAA Journal*, 48th AIAA Aerospace Sciences Meeting:1–14, 2010.

[33] Unknown. *TSFOIL2 Manual*. Virginia Tech Aircraft Design Software.

[34] Mark Drela. Mses / mises airfoil synthesis.

[35] BSc. Erwin Moerland. Development of an aeroelastic analysis tool for structural sizing of high-lift devices during preliminary design. Master's thesis, Delft University of Technology, 2011.

[36] Unknown. L-28-336. Technical report, Fokker, 1991.

[37] William Chauvenet. *A Manual of Spherical and Practical Astronomy V. II.* A Manual of Spherical and Practical Astronomy V. II, unknown, 5 edition, unknown 1960. Reprint of 1891 , pages 474 - 566.

Appendix A

Model

Chapter three already showed a general flow chart of the buffet onset prediction process, indicating the inputs, actions, outputs and use of external programs used to translate the geometry input in to a buffet onset boundary. This appendix shows how the middle column in Figure 3.1 is built up, and how the different Matlab components interact. This column can be seen as program that ties all separate programs such as AVL, TSFOIL and MSES together, in combination with the airfoil interpolation routine and separation criteria. Since all programs involved have different inputs and outputs, in different formats, every iteration done in Matlab requires a lot of creating, writing, updating and removal of in-, output files, and run cases. In Figure A.1 each block stands for a Matlab function or $.m - file$. Again, Figure A.1 has to be read top down, and left to right, in a similar fashion as Figure 3.1. Combining the global overview presented in Chapter 3, with the detailed Matlab structure in this appendix, gives a complete overview of the buffet prediction process.

Next to these program components, there is an airfoil database needed containing airfoil data files with x, y coordinates, together with the AVL, MSES and TSFOIL executable files. The tool developed only requires one input data file in which all wing parameters, airfoil contours, fuselage size and flight altitude have to be defined. In this file, the user can also indicate which separation criterion and 2-dimensional simulation method is to be used. This way, the Matlab code can be compiled into an executable that only needs this text file as input, and writes another text file with the buffet onset data as output. A detailed example of this input file and resulting output file can be found in Appendix B.

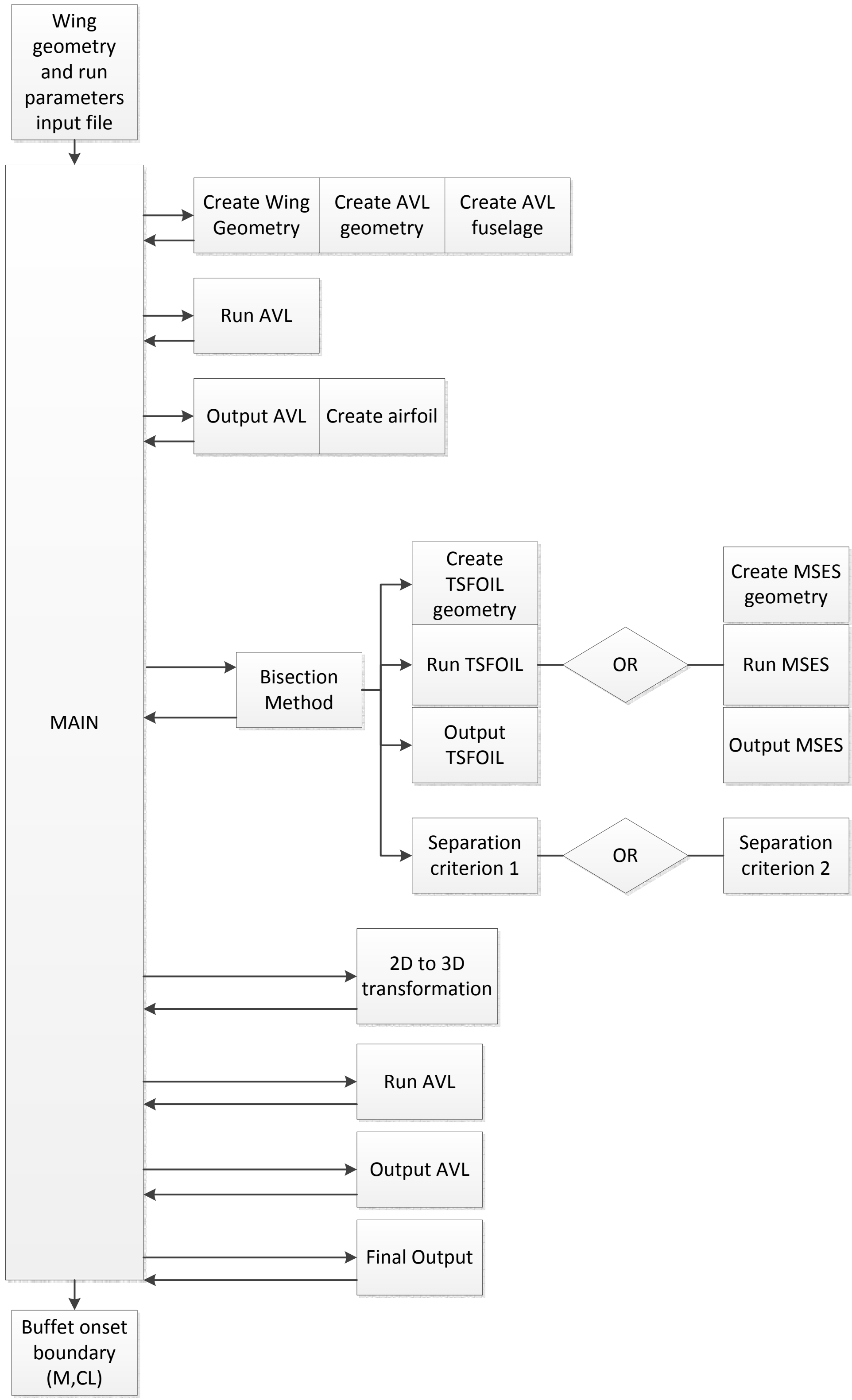

Figure A.1: Detailed architecture of the Buffet tool Matlab code

A.1 Geometry Input

The program's only input is a run case file *runcase.dat* which specifies the wing geometry and state variables that will be used. The format of this file can be seen in appendix B and contains in a predefined order information about the wing such as Span, root and tip chord, taper, sweep, twist and the different airfoils used in the wing design and their spanwise location. In this run case file it is also specified which type of simulation is used, as well as the separation criterion. This information is read in Matlab, and formatted in order to be written to the input file for the next step of the program, AVL.

A.2 AVL Run

After the wing is constructed by Matlab with the help of the input parameters supplied by the user in the run case file, Matlab writes a *fuselage.dat* file with fuselage coordinates, a *wing.avl* file with the wing geometry and an *AVLrun.dat* file. The latter one is simply a list of commands to be executed by AVL in a certain order, so everything is done automatically without user interference. AVL is executed by Matlab, and the output is saved in *AVLoutput.out*, which is a data file with resulting forces and coefficients. Matlab at this stage reads the output file of AVL, and searches for the row with local lift coefficient distribution c_l. This distribution is loaded in to Matlab, and the maximum value is determined. At the location at which this maximum occurs, the other wing parameters are retrieved, such as chord and span wise location.

A.3 Airfoil Construction

With the span wise point of the highest loaded section known, the airfoil at this locations needs to be constructed. This is done with the help of the airfoil interpolation routine as discussed in Chapter 3. The two neighbouring airfoils are determined, their coordinates redistributed and a weighted average airfoil is constructed. This airfoil is saved in Matlab workspace as x, y-coordinates for the upper and lower side of the airfoil (four vectors total) and not written into a file yet, because the format of the output file at this stage, which forms the input file for the next step, is different for TSFOIL and MSES. Until this step, the program is almost instantaneous in terms of computation time.

A.4 2-dimensional Simulation

Next the program is at an intersection; it can start to analyse the flow over the airfoil with the transonic small disturbance code TSFOIL or the 2-dimensional Euler code MSES. Depending on the user's preference, it starts with the one or the other. From this point on, the program enters a loop, because it has to simulate the flow over this airfoil a number of times to find the buffet onset points.

A.4.1 TSFOIL

If TSFOIL is the program of choice, Matlab creates an input file for TSFOIL called *section.inp* in which the upper and lower side x, y-coordinates are written, together with the first α and Mach number to be used in the bisection method. A run file is created with the commands to be executed in TSFOIL, just as was the case in the AVL step. At this point the bisection method described in Chapter 3 comes in play, and the program is ran 10 times in combination with a separation criterion check after each run, order to accurately arrive at a $M - \alpha$ combination that induces separation and thus buffet. This process is repeated a number of times and the resulting buffet onset points are saved in the Matlab workspace. It has to be noted the input file *section.inp* has to be update every time TSFOIL is ran, because it contains the α and Mach number setting at which the airfoil is subjected.

A.4.2 MSES

If MSES is the program of choice, Matlab creates two input files for MSES called *blade.air* and *mses.air*, and a run file which contains the commands to be executed by MSES. First an executable called *mset.exe* has to be executed to create the grid for the MSES run. After this, the MSES simulation can be ran by executing *mses.exe* , and the last step is to execute *mplot.exe* to write the resulting pressure distribution over the airfoil to an output file, which is read by Matlab after every MSES run to determine if there was separation.

MSES uses two input files. One file to describe the airfoil geometry, and one file to describe the flow parameters such as free stream Mach number and angle of attack. When used in an iterative way like in this thesis work, only the file with flow parameters needs to be updated each iteration. To use MSES on a Windows platform, the Fortran code had to be compiled with some changes with respect to the Linux version. This means for this thesis research, the MSES code was only altered to remove the plotting options and write the pressure distribution to an output file. No other data was produced in this versions of MSES. If MSES is compared to TSFOIL from a computational time of view, a larger set of equations has to be solved in the MSES case, and the conditions on the outer boundary of the boundary layer have to be matched with the outer flow field, which takes significantly more time.

A.5 Separation Criteria

The 2-dimensional analyses programs make use of one of the two separation criteria at hand, being the critical pressure jump criterion and the limiting local Mach number criterion. The latter one cannot be used when MSES is used in the previous step, as described in the paragraph above. The separation criterion of choice is called inside the bisection routine, because the interval is bi-sectioned as a function of whether there is separation or not.

A.6 2-dimensional Buffet onset boundary

After the program has exited the loop of the 2-dimensional airfoil analysis, the result is a matrix with Mach numbers and angles of attack. These Mach and angle of attack values will have to be scaled with help of the relations described in Chapter 3. When this is done, the result is a matrix with Mach numbers and angles of attack for the 3-dimensional wing.

A.7 3-dimensional Buffet onset boundary

The final phase of the buffet prediction tool is the computation of the wing lift coefficient C_L with help of the matrix of Mach numbers and angles of attack. For this tool this is done by AVL. The program enters another loop, writing a new run file and input file for each AVL run. AVL is ran for each buffet data point, and results in a matrix of Mach numbers and wing lift coefficients.

A.8 Final Output

What is left is the handling of the final output, since all computations have been made. A file is written by Matlab called $buffetonset.dat$ containing the 2-dimensional buffet onset data, and both the 3-dimensional $M - \alpha$ and $M - C_L$ buffet onset data. In addition to this, the Reynolds number of the last run is posted, to give an indication of the freestream Reynolds number based on the chord c_η of the airfoil at which the 2-dimensional analysis is carried out.

Appendix B

Run case

B.1 Introduction

This appendix shows an example of an input file used for the transonic buffet onset boundary determination method developed in this thesis, and the output file it creates, containing the wing buffet onset boundary in terms of $M_\infty - \alpha$ and $M_\infty - C_L$. The reason both these buffet onset boundaries are displayed in the output file is, this way the user still has the option to use another program of choice to compute the wing lift coefficient at certain $M_\infty - \alpha$ combinations, instead of the AVL program used by this prediction tool (for example Matrix-V). In addition, an indication of the free stream Reynolds number based on the chord c_η of the airfoil used is displayed.

B.2 Input File

The input file defines the wing geometry, including the airfoils, and simulation parameters used. Table B.1 shows the different parameters and their description. Line 1 through 30 is the file header, containing information on the format of the inputs required. Figure B.1 shows an input file for a wing consisting of 8 airfoils.

B.3 Output File

The out file contains the buffet onset data for the wing under investigation. Table B.2 shows the different parameters and their description. Figure B.2 shows an example of an output file for a run of 10 buffet onset points.

Table B.1: Input file parameters

Line	Parameter	Description
5	2-dimensional simulation choice	1)-MSES and 2)-SFOIL
6	separation criterion	1)-pressure jump 2)-local Mach number
7	sweep line position	$0 \leq \phi \leq 1$
8	number of buffet points	the number of data points desired
10	flight altitude	flight altitude in feet
11	Mach number for AVL run	Mach number desired for AVL run
12	angle of attack for AVL run	in degree
13	wing span for 2 wings	in meter
14	root wing chord	chord of root airfoil in meter
15	tip wing chord	chord of tip airfoil in meter
17	X_{LE} vector	vector with x-coordinates of airfoils in meter
18	Y_{LE} vector	vector with y-coordinates of airfoils in meter
19	Z_{LE} vector	vector with z-coordinates of airfoils in meter
20	airfoil chord vector	vector with chords of the airfoils in meter
21	incidence angle vector	vector with incidence angles in degree
22	number of spanwise vortices vector	additional AVL input
23	spacing vector	vector with additional AVL input
25	fuselage length	length of the fuselage in meter
26	fuselage diameter	maximum fuselage diameter in meter
28- 35	list of airfoils to be used	list of airfoils files to be used
37	local path	location of the local folder for TSFOIL

Table B.2: Output file parameters

Line	Parameter	Description
2	Reynolds number	Reynolds number based on the freestream and chord
5-15	2-dimensional buffet onset	in $M-\alpha$
18-28	3-dimensional buffet onset	in $M-\alpha$
31-42	3-dimensional buffet onset	in $M-C_L$

```
****************************************
*      Inputs in this order            *
****************************************

2
1
0.5
10

30000
0.5
0
28.08
5.28
1.26

0      0.86    2.34    2.96    3.54    4.54    5.32    5.50    0
0      1.70    4.60    6.44    8.18    11.16   13.52   14.04   0
0      0.07    0.20    0.28    0.36    0.48    0.59    0.61    0
5.60   4.86    3.6     3.14    2.71    1.97    1.38    1.26    0
3.66   3.42    3.01    2.08    1.21   -0.29   -1.47   -1.74    0
0      0       0       0       0       0       0       0       0
0      0       0       0       0       0       0       0       0

35.53
3.30

Airfoils\f100-1mod.dat
Airfoils\f100-1mod.dat
Airfoils\f100-2mod.dat
Airfoils\f100-3mod.dat
Airfoils\f100-4mod.dat
Airfoils\f100-5mod.dat
Airfoils\f100-6mod.dat
Airfoils\f100-6mod.dat

C:\Jeroen\TU\AE5-002\Matlab\Current\TSFOILdata
```

Figure B.1: Example input file

```
Reynolds number based on chord
1.81658e+007


2D Mach Alpha Buffet onset
0.815967    -4.03214
0.813037    -3.21126
0.763232    -2.5896
0.748584    -1.81852
0.733936    -1.04744
0.713428    -0.301265
0.679736    0.388879
0.64751     1.08525
0.669482    2.01197
0.59624     2.53402


3D Mach Alpha Buffet onset
0.866276    -1.58683
0.863166    -0.715333
0.81029     -0.0553404
0.794739    0.763279
0.779187    1.5819
0.757415    2.37408
0.721646    3.10678
0.687433    3.84608
0.71076     4.82994
0.633002    5.38418


3D Mach CL Buffet onset
0.866276    0.25908
0.863166    0.38393
0.81029     0.43863
0.794739    0.53581
0.779187    0.62951
0.757415    0.71169
0.721646    0.77275
0.687433    0.83403
0.71076     0.96704
0.633002    0.96822
```

Figure B.2: Example output file

Appendix C

Fokker 100 Airfoils

C.1 Introduction

This appendix contains the six airfoil coordinates of the six airfoils used in defining the Fokker 100 wing geometry from root to tip. The airfoils are defined trailing edge to leading edge upper side, and leading edge to trailing edge lower side.

C.2 Airfoil coordinates

```
f100-1mod upper side
0.9985122981240628      2.7695784821066304e-4
0.9966311412986861      4.926871268728354e-4
0.9943435803757285      7.550457453973921e-4
0.9916514353028233      0.0010638246299926317
0.9885568467509086      0.001418767623702268
0.9850622741497337      0.00181956941084463
0.9811704936704875      0.002265875226287289
0.9768845962427517      0.002757283095595076
0.97220798564855        0.003293348966785231
0.9671443766444736      0.0038735942960657164
0.9616977929518808      0.004497514680861941
0.9558725648896885      0.005164587555109752
0.9496733264610081      0.005874277272181942
0.9431050118362272      0.006626037039458814
0.9361728513283643      0.007419308505159692
0.9288823670599665      0.008253520705266654
0.9212393685668816      0.009128090484051365
0.913249948641492       0.010042427000854242
0.9049204799472667      0.010995944928845253
0.8962576138111591      0.011988098559146306
0.8872682863831324      0.013018481911671124
0.8779597583646038      0.014087222296895139
0.8683394720362897      0.015193783614268673
0.858415076108451       0.016337236677930203
0.8481945193549738      0.017517127243541486
0.8376859439151776      0.018732604520197375
0.8268975516874112      0.01998132667773606
0.8158382844979047      0.021265389705160474
0.8045175463051177      0.022588947670305858
0.7929445580464439      0.02395270743599733
0.7811287531109096      0.025357405935453534
0.7690799097685765      0.02680496893907095
0.7568081673665707      0.028298646410749983
0.7443238952384653      0.029841924489241792
0.7316374231420262      0.03143640027462245
0.7187588405986972      0.033080374738574204
0.7056980175233272      0.034769266039747046
0.6924646405972987      0.03649607791970292
0.679067831500596       0.038248578470326845
0.6655149072609887      0.039999656157623034
0.6518154245343712      0.041738067264194614
0.6379795837581145      0.04345619838915661
0.6240160822722118      0.045132718899499276
0.6099345254732118      0.04675131200049126
0.5957458577482694      0.04830509368539289
0.58146167498813        0.04979186796869707
0.5670936036487251      0.0512089404744855
0.5526531192570803      0.05255114454341941
0.5381516920797592      0.05381194852447472
0.5236008846210094      0.054984280642042443
0.5090124556114483      0.056061808856637675
0.49439843550631796     0.0570403196189503
0.47977096565122107     0.057916084778582955
0.46514223994193726     0.05868509172253336
0.4505245040689105      0.05934293418536523
0.43593008440403275     0.05988534230405256
```

```
f100-1mod lower side
6.23753685008751e-4     -0.003920183711970723
0.0024409552249451206   -0.007891734313092546
0.005417262198704551    -0.011608548915592586
0.009462263151004097    -0.014799161978405743
0.014270963411237413    -0.017549818893437173
0.019675561218162687    -0.0199699183465199
0.02559396149074122     -0.022121221273754387
0.03195613866408638     -0.024115546125892888
0.03873059286287937     -0.026002138212813674
0.04589283759610729     -0.02782760863177167
0.053423050090312424    -0.029636080590178523
0.0613078940063081      -0.03145183879463949
0.06953897339258043     -0.0332799811618186
0.07811223050100265     -0.03510508727650013
0.08702360110251954     -0.036908953104725285
0.09626869464056484     -0.03867164914231249
0.10583951178857669     -0.040388917527490936
0.11572876173316263     -0.0420511014926441
0.12592601089637628     -0.04366577261838524
0.136420562995477       -0.04524300844755428
0.14720263115776364     -0.046787082760145586
0.1582667497195748      -0.04826987773900725
0.169619454607639       -0.04955363447049493
0.18123661654419865     -0.05074617127734188
0.19310237028361757     -0.05190239759648138
0.2052058811870635      -0.05303303212808656
0.21753719590354734     -0.05413864260506035
0.23008707778003168     -0.05520969788721668
0.2428460803127719      -0.056235906021838006
0.25580442635935424     -0.05720756570422042
0.2689517729410145      -0.05811907119707347
0.2822774845321075      -0.05896607247562618
0.2957707388528386      -0.059744266166605955
0.30942063124675284     -0.06044747179649026
0.32321617932994545     -0.06106666592365213
0.33714615046083685     -0.06159250830365479
0.3511990435571513      -0.0620154769070973
0.36536308919460275     -0.06232535128174554
0.3796262123926399      -0.06251170933685635
0.3939760133188595      -0.06256454457763459
0.4083998085675503      -0.062479556950830614
0.42288482400604066     -0.0622574675887579
0.43741828493565854     -0.06189966542576386
0.4519874441331499      -0.06140822253507747
0.46657961425775013     -0.06078603659494501
0.4811821851310195      -0.06003655901535551
0.49578263671071404     -0.059163662561819326
0.5103685342929768      -0.05817133314824595
0.5249275361469703      -0.0570636883217349
0.5394474361351282      -0.05584539317027918
0.5539162391575262      -0.05452228211327737
0.5683221156588819      -0.05310050687538537
0.5826534301835864      -0.05158671262047559
0.5968984364281306      -0.04998518340359
0.6110454100890388      -0.04829944636352885
0.6250825111550489      -0.04653130361021442
```

Figure C.1: Airfoil coordinates upper and lower surface $\left(\frac{x}{c}, \frac{t}{c}\right)$ for airfoil f100-1mod

```
f100-1mod upper side continued
0.42137140104807264     0.06030883424755837
0.4068609484498598      0.060611078328051786
0.3924112531770079      0.06079071389208091
0.3780348358431795      0.060846883361479615
0.3637441574161669      0.060785200040775735
0.3495514378424628      0.060616256976498785
0.3354686141463325      0.0603497433095368
0.3215073504987724      0.059995426590751536
0.30767904539448165     0.05956312338283048
0.2939948648557815      0.05906196105188212
0.28046579767150476     0.05849952835857043
0.26710270837001265     0.05788141363140747
0.2539163568006125      0.05721149361307479
0.24091735100742992     0.05649323657350658
0.22811574240025076     0.055736477019871854
0.2155207153336187      0.05496103491845524
0.20314121331504081     0.05418579248689121
0.1909862098869316      0.05342548494752869
0.17906570886073203     0.052675406793511174
0.16738957676122143     0.051930170684015134
0.15596864737586455     0.05116725980902686
0.1448168115131625      0.050323537186443675
0.1339527963018034      0.04930045935673421
0.12339051691875724     0.048085196273165674
0.11313761424796429     0.04672029168198502
0.10320285629243198     0.045226135809961356
0.0935959230662271      0.04361162930853327
0.08432221550443568     0.04190721195483612
0.07539121778227512     0.04011561434104231
0.06681075779748818     0.03824712155917166
0.05859495509203555     0.03628362758367187
0.050753650925044844    0.03422890527119177
0.043300654149862186    0.032073039059535194
0.036248547543151655    0.029815314688135013
0.029614239108433457    0.02744479310885859
0.023430186562741734    0.024920308457741545
0.017738388034977633    0.02220024709320348
0.012642267598642962    0.019164270922980346
0.008236176928003713    0.01579114889823212
0.004659801571450399    0.012067454907213573
0.0021035694255019406   0.008037044487074228
5.506940406269129e-4    0.003943022358069445
0.000000000000000000    0.000000000000000000
```

```
f100-1mod lower side continued
0.6389986813300033      -0.04468784151266884
0.652784005358574       -0.04278312203353976
0.6664293982044067      -0.04083491644374295
0.679925254366527       -0.03885530815092353
0.6932607775510728      -0.036846798184693066
0.7064281718015344      -0.03483062785192878
0.7194190654333873      -0.03282251263660519
0.7322244050553723      -0.03083247072399867
0.7448332184217923      -0.02885713033645946
0.7572359459504974      -0.026901176964100357
0.7694234718232116      -0.024970993978831676
0.7813868356758498      -0.023072785865073633
0.7931181341210727      -0.02121826388062431
0.8046120136934711      -0.019434421365235335
0.8158629952443675      -0.01774761491657738
0.8268648777813792      -0.01618061183639808
0.8376106927061516      -0.014752750908076257
0.8480912893628203      -0.013468311230059099
0.8582950115158934      -0.012309082826989733
0.8682108074638947      -0.01125621191703794
0.8778284470940867      -0.010292747056970837
0.8871384193788001      -0.009403691221339515
0.8961318729152498      -0.008576311737574008
0.9048007753744108      -0.007802721949839532
0.9131376669113817      -0.007077857754470049
0.9211354517593121      -0.0063973926428495245
0.9287873869588664      -0.005757671679416886
0.9360870755320675      -0.0051556678667655205
0.9430284613288725      -0.004588935547395306
0.949605834132795       -0.004055671582306708
0.9558138945165728      -0.0035555050259973844
0.9616476855808757      -0.0030886342829544965
0.9671025406466704      -0.0026551362746489514
0.9721740881319512      -0.0022549786625965414
0.9768582567305069      -0.0018880392895569086
0.9811512802580278      -0.0015541251524524553
0.9850497021440173      -0.0012529907022402267
0.988550379553219       -9.843552759721465e-4
0.9916504871250017      -7.479194778474044e-4
0.9943475203232273      -5.433803390693112e-4
0.9966392983925263      -3.704451006287522e-4
0.9985239669195841      -2.2884347860347562e-4
```

Figure C.1: Airfoil coordinates upper and lower surface $\left(\frac{x}{c}, \frac{t}{c}\right)$ for airfoil f100-1mod - continued

```
f100-2mod upper side
0.999984642552021       1.0795102474525562e-4
0.9985270191019737      4.1376541921249764e-4
0.9966655580520029      8.03001753417188e-4
0.9944015536149253      0.0012744515788380428
0.9917365846509937      0.0018266621344161312
0.9886725159006856      0.002457945461843153
0.9852114990029763      0.003166387329039633
0.981355973083053       0.003949854957258815
0.9771086646610154      0.004806002319402814
0.972472586602808       0.005732271524040326
0.967451035808284       0.006725888522742811
0.9620475893116509      0.007783851081113321
0.9562660984605004      0.008902906641686054
0.9501106808468207      0.010079517387019388
0.9435857096947197      0.011309809492464901
0.9366958004761136      0.012589503249392274
0.9294457946425283      0.013913820449159852
0.9218407405491621      0.015277365150851794
0.9138858719344218      0.016673973711253957
0.9055865847417452      0.018096529725237134
0.8969484136806495      0.019536739290431124
0.8879770107873889      0.020984861743948986
0.8786781294518238      0.02242939068738625
0.8690580129813149      0.02385937837370385
0.8591284429858913      0.025299741409539812
0.8488978671799915      0.02675226806993759
0.8383744639746342      0.028215470163099783
0.8275700053010734      0.029712302700083633
0.816495378231109       0.0312580543447624
0.8051584479132162      0.03284466727838038
0.7935687581229907      0.03447459938567702
0.7817358988161062      0.03614912839202078
0.7696697051518679      0.0378698152047297
0.757380273237459       0.03963864762078078
0.7448777793083313      0.0414568226737745
0.7321721750057046      0.04332274854792871
0.7192728847050234      0.045230154357910425
0.7061886797752088      0.04716738953079801
0.6929280397903251      0.04911983801362588
0.6794998311826419      0.05107434509294376
0.6659124957847389      0.0530134530540903
0.6521742347141574      0.0549160894146789
0.6382932599374518      0.056758630336075526
0.6242796000995384      0.05852814892808969
0.6101445874847227      0.060220059571733875
0.5958998002929934      0.061830712914560035
0.5815566621279897      0.06335394686684652
0.5671266299558637      0.06478235243473947
0.5526212716482976      0.0661077127726132
0.5380523411112924      0.06732166859629228
0.5234319563571839      0.06841791535296837
0.50877242622735        0.06939064542600526
0.49408618805867105     0.07023376162797655
0.47938581575885164     0.07094083497679908
0.4646840630725791      0.07150585833396209
0.4499938738414377      0.07192406170592827
```

```
f100-2mod lower side
8.240264153892908e-4    -0.0038492458492290892
0.0033692974264407766   -0.007338662744874307
0.007220806889934853    -0.010102326973795058
0.011773949350018829    -0.012466605356503029
0.016840557145244173    -0.014640216332508045
0.02238505070002889     -0.01663168919915727
0.028383343347465142    -0.01843596932945918
0.03482153570704471     -0.020027983968974348
0.041676916390393934    -0.021416406075991677
0.04892948646139488     -0.02262114985468
0.05655615701031801     -0.023703931174480136
0.06454728024339064     -0.024661072466584485
0.0728921809742705      -0.025499015754300358
0.08158000194623197     -0.02623481315890665
0.09059596680385414     -0.026946203032655682
0.09992922801553904     -0.027676847062410078
0.10957204741478997     -0.028430118519434278
0.1195175623527453      -0.029194961211252184
0.1297542624456455      -0.030016467775211508
0.14027261254422635     -0.030909658009849204
0.15106970516185758     -0.03180785606480491
0.16213467065794832     -0.03273745925263962
0.17345636495445366     -0.033724807870061164
0.18502206152984893     -0.034808073871141945
0.19682394710929332     -0.035968515109853855
0.20885608282134174     -0.037168272733928635
0.22110813571569246     -0.03841373809761866
0.23357519833095927     -0.03965575705666398
0.24625005625520352     -0.04086474911248967
0.25912464957101156     -0.04201507865635588
0.2721868860955605      -0.043122414035593366
0.2854265603280048      -0.044180236318482814
0.29883259371931437     -0.04519094239305894
0.3123943414813967      -0.0461496166438808
0.3261011865633316      -0.04704846023625732
0.3399423871627186      -0.04787821603785744
0.3539070094728203      -0.04862885974776024
0.3679839382999312      -0.049288743588420864
0.3821617768416262      -0.04984584650790766
0.3964288177442843      -0.050287687056120134
0.41077304513424945     -0.05059991181899349
0.4251820152080651      -0.05076817735029745
0.4396428313481197      -0.05078035871419113
0.4541422965846738      -0.05063514180335444
0.46866721635136055     -0.0503346616704337
0.4832044754563837      -0.04988200297204284
0.4977411008822561      -0.0492817927131939
0.5122642840247476      -0.048539455162211975
0.5267613846210636      -0.047660791292416314
0.5412199022148377      -0.04665139287766572
0.5556274801980323      -0.04551679640424257
0.5699719324923931      -0.04426280573510485
0.5842413734625039      -0.04289674049838033
0.5984242594324415      -0.04142736594808925
0.612509196682645       -0.039862798235449415
0.6264846049578122      -0.038207793311367914
```

Figure C.2: Airfoil coordinates upper and lower surface $\left(\frac{x}{c}, \frac{t}{c}\right)$ for airfoil f100-2mod

```
f100-2mod upper side continued
0.43532834041245033     0.07219215868078706
0.4207006410118254      0.07230799317017098
0.40612397268626593     0.0722761635286753
0.39161125869216973     0.07211084203794026
0.377174955125402       0.07182881579831261
0.36282714463441446     0.07144399904371629
0.3485796135018366      0.07096856080503945
0.33444386706700474     0.07041424756038028
0.3204311805196668      0.06979182639724682
0.3065526800732965      0.06911007456149826
0.2928193170682203      0.06837704126057029
0.27924173464341373     0.06760268665269777
0.2658310530496292      0.06678547874641398
0.25259790903788465     0.06592975002214561
0.23955316112794725     0.0650342356503668
0.22670732207619865     0.0641005460815746
0.21407003192695523     0.06313991033643025
0.20165366835135037     0.06212644924417514
0.18947226412697757     0.06101854289317468
0.17753439927026213     0.0598391176563494
0.1658516189919482      0.05857725073281127
0.1544347204111157      0.05722991525374287
0.14329498166122664     0.055790328212307234
0.132442292573912       0.05426251268093391
0.12188224267403694     0.05267759579965346
0.11162530244784985     0.051030135658366664
0.1016824416310841      0.04931184545353033
0.09206210944903666     0.04752946197809629
0.08277576009102026     0.04567324829477215
0.07383190225109466     0.04374883487811347
0.065242931897886       0.04174460545789257
0.057019036758359724    0.03966030653841528
0.04917830478930998     0.03746891045673494
0.04174039270805685     0.035146094544325476
0.0347312787047149      0.03266120545208792
0.028191092023357945    0.029961865732961404
0.022171448431371785    0.02700334208980627
0.01675795657014379     0.023712535320598253
0.012020507390169305    0.020102763110106753
0.008039455947667801    0.01619959111509819
0.004828981630637915    0.012125293248163733
0.002365215675980679    0.00800747998824746
7.085940863494214e-4    0.003930664357296155
0.000000000000000000    0.000000000000000000
```

```
f100-2mod lower side continued
0.6403389352813439      -0.036466268801136736
0.6540607356569053      -0.034641892189216525
0.667640155346537       -0.032748885202052505
0.6810683736371685      -0.030806289717500948
0.6943363915340354      -0.028829501687309862
0.7074300701752121      -0.02679843083517917
0.7203444167528932      -0.02475164051371219
0.7330744768067821      -0.022724867051557403
0.7456136108470538      -0.020741712797183624
0.7579490348399929      -0.018786043526234728
0.7700741670816371      -0.016879901522597794
0.7819839351115918      -0.015054584165044222
0.7936725808985325      -0.013337954280061575
0.805132676586054       -0.0117482309541227
0.816354457634121       -0.010287628251767211
0.8273279493722033      -0.008955631227466586
0.838043331366019       -0.0077513471598243955
0.8484909413586288      -0.006673410982626584
0.8586611842633671      -0.005718822490561675
0.8685446013701615      -0.004883070186670008
0.8781319933362872      -0.004160990261905209
0.8874144502126707      -0.003546839494600054
0.8963833778510502      -0.0030343685281343903
0.9050304031977309      -0.0026143674405562436
0.9133472672044073      -0.0022698645734166916
0.9213263137938782      -0.0019845178905336758
0.9289604849668198      -0.0017444701710526414
0.9362432271220686      -0.0015381887686791256
0.9431684228880917      -0.0013562919680699765
0.9497303442993037      -0.0011913898420706749
0.9559236682164435      -0.0010397877882157049
0.9617434693289783      -9.018234255351187e-4
0.9671851180855923      -7.778092287032424e-4
0.9722442763495999      -6.676819729187967e-4
0.9769169034177968      -5.710686767173797e-4
0.9811992616540971      -4.873510587295159e-4
0.9850879216014263      -4.157278035570416e-4
0.9885797664878402      -3.5527396037628644e-4
0.9916719960890803      -3.0499683332604064e-4
0.9943621299486333      -2.638877649158131e-4
0.9966480099871713      -2.3096926199943135e-4
0.9985278025556187      -2.0533696751167833e-4
```

Figure C.2: Airfoil coordinates upper and lower surface $\left(\frac{x}{c}, \frac{t}{c}\right)$ for airfoil f100-2mod - continued

```
f100-3mod upper side
0.9999897138832178     2.5646285292635593e-5
0.9985288910811491     3.220894985424642e-4
0.9966633682836264     6.994333600863295e-4
0.994394464616378 9    0.00115655651323118 1
0.9917237933917504     0.0016921347043918106
0.9886532647707279     0.002304658597371112
0.9851850876907352     0.0029924492802943744
0.9813217705802219     0.0037536690706109527
0.9770661203843582     0.004586325081592246
0.9724212394523013     0.005488262953441523
0.9673905198859386     0.006457148177534011
0.9619776350240407     0.00749043255551365
0.9561865278375934     0.008585303535781142
0.9500213961471766     0.009738614455297081
0.94348667474949       0.010946794077954227
0.9365870147677067     0.012205734250845101
0.9293272608310659     0.013510654979819674
0.9217124270555959     0.01485594673281293
0.9137476732522852     0.016234990284252748
0.9054382833422354     0.01763995488190812
0.8967896486191936     0.0190615759115632
0.8878072592756944     0.02048891351931662
0.8784967085070502     0.02190909379853215
0.8688640795488665     0.023309595728342854
0.8589210281799664     0.024714703945807548
0.8486759100909563     0.02612531007250811
0.8381367903541596     0.027538764267230557
0.8273156265278769     0.028980064616552066
0.8162238220892064     0.030468947446818904
0.8048687223999974     0.031993162019962364
0.7932595894570925     0.033553191860021335
0.7814059631439654     0.03515004935107241
0.7693175974290148     0.036784846172099074
0.7570044492972052     0.03845875740499964
0.7444766666608135     0.040172979455336856
0.7317445749112109     0.041928680195614236
0.7188182956669384     0.04372431082853666
0.7057067867354322     0.04554884425327342
0.6924189152904896     0.047389560164458354
0.6789637660109666     0.04923413578274251
0.6653501320784933     0.05106674568793201
0.6515861460376379     0.05286475839285387
0.6376808354635181     0.05460986794529913
0.6236445095521899     0.05629145562314544
0.6094882891101366     0.05790394727288469
0.5952236567350787     0.05944366849627832
0.5808620645423017     0.060905547539215794
0.5664149546782562     0.06228303002815979
0.5518937969052949     0.06356811394470883
0.5373102942084        0.06475342209061341
0.5226764295276456     0.06583303302082848
0.5080043845187928     0.06680193971280064
0.49330644442456945    0.06765492967407273
0.47859498470130296    0.0683862396169188
0.4638825168452825     0.06899024396040535
0.4491817148430123     0.06946240017471782
```

```
f100-3mod lower side
5.407766233242036e-4   -0.003908717041265431
0.0025767878264750317  -0.007714468291952455
0.0061944605641779255  -0.010754871668829642
0.01077558765398675    -0.013040022980026373
0.015965669151990533   -0.014874838477069347
0.021670129733047203   -0.016314204646036033
0.027836388852708654   -0.017366396590148072
0.0344142043717222     -0.01814857874724935
0.04136749160485737    -0.01882824459412247
0.04868475257122961    -0.019443092466390532
0.056358067033640324   -0.02000393562053047
0.06437917532889248    -0.020531160175383523
0.07273990212670405    -0.02104717649513016
0.08143309860744764    -0.021557939511091993
0.0904515325333716     -0.022067365539253193
0.09978816823682093    -0.02257167854243931
0.10943567614425367    -0.023067521080077806
0.11938637867415844    -0.023553319372469825
0.12963191765610624    -0.024036792423023756
0.14016349074068588    -0.024531040244624075
0.15097150032757467    -0.02506102798745324
0.16204595619459963    -0.02565202078748038
0.17337603255479087    -0.026334202387217218
0.1849483377541199     -0.027162849185496333
0.19675401157240324    -0.028116493443135143
0.2087886348899477     -0.029125700755446928
0.22104542200217395    -0.03015554522642122
0.23351557711007917    -0.03119377390165324
0.2461899178811681     -0.03223046891407703
0.25905943770181217    -0.03325097281372719
0.2721146903099415     -0.03424309167391049
0.28534560343702703    -0.035199831883637074
0.29874173874610116    -0.03611656666401033
0.31229281694522154    -0.03698367923133347
0.3259880005001578     -0.03779703215140954
0.33981642654704763    -0.03855019696750738
0.353767117973782      -0.03923537896383681
0.3678290918219671     -0.03984031494896208
0.38199106241655006    -0.040353175195227034
0.3962414437747922     -0.04076226232319514
0.4105683627014721     -0.04105486537850286
0.4249595982883864     -0.04121792750772754
0.4394025455501943     -0.041243398521223294
0.45388440622443504    -0.04113167380077912
0.46839239224671597    -0.04088448722586082
0.48291377642615885    -0.04050474767296266
0.49743594805470603    -0.039996907631606855
0.5119464261103917     -0.03936599522732431
0.5264328562886766     -0.03861718132478602
0.5408829881348882     -0.03775530077785661
0.5552846889152929     -0.03678519424123262
0.5696259783937835     -0.03571213243453508
0.5838951259268162     -0.034542817543796296
0.5980806623370508     -0.033285046718327514
0.6121711523469479     -0.03194503431960487
0.62615511945295       -0.030527003808706477
```

Figure C.3: Airfoil coordinates upper and lower surface $\left(\frac{x}{c}, \frac{t}{c}\right)$ for airfoil f100-3mod

```
f100-3mod upper side continued
0.43450538815083917     0.06979971219357103
0.4198664169753099      0.07000012449238069
0.4052777217810231      0.07006560517771085
0.3907521004384563      0.07000706367110214
0.37630199206536225     0.06983961062049589
0.361939485677011       0.06957639847909795
0.34767639555560115     0.06922869788307913
0.3335242829155011      0.06880729378760679
0.3194944849449392      0.0683223206106635
0.3055981771157844      0.06778221363449059
0.29184639929746387     0.06719386673806557
0.2782499102668218      0.06656628198927426
0.26481961925661623     0.06590138142973855
0.2515663958889143      0.06519907245765785
0.23850080846901878     0.06446249126837632
0.22563427789126378     0.0636777190236738
0.21297657164222675     0.062856860317373
0.20053865368563029     0.06199075625105093
0.18833634896524512     0.061007880601616465
0.17638036051050568     0.05991350606049297
0.16467276157225366     0.05879887458954062
0.1532283371827997      0.05761310162786575
0.14205999923449356     0.056330701067189966
0.13117724177184997     0.05495934126772735
0.12058949484054977     0.05350478114099516
0.11030439384453099     0.05198312533262369
0.10033191242125754     0.050391827693732724
0.09068078669039664     0.04873566227402262
0.08136345412626113     0.04699841806194124
0.07239256763770498     0.04516596979810418
0.06378404391642814     0.04321442692877015
0.055553013001031805    0.0411298694822054
0.04771669873139507     0.03889827778769973
0.040295699953536       0.03650106782420958
0.033315120256501025    0.03391954888553873
0.02681706153865609     0.03110599775747542
0.020882453312240108    0.027970344440463354
0.015600943933431127    0.02446278648189642
0.011016834420472629    0.020651804929732447
0.007157692076594761    0.016622079997054257
0.004126611369147305    0.012408033024111398
0.0019006702830430234   0.008154022922303147
5.253458137394392e-4    0.0039684003667314425
0.000000000000000000    0.000000000000000000
```

```
f100-3mod lower side continued
0.6400210836697552      -0.029033996261393035
0.6537578704491023      -0.027470723892579558
0.667355555420417       -0.025851164324864388
0.6808049646722976      -0.024192983513297732
0.694095912170495       -0.022503531871198856
0.7072156423101548      -0.02076892025844615
0.7201581228382171      -0.0190254584089293
0.732916695549575       -0.01730189453442404
0.7454829989702407      -0.015612881064511282
0.7578452371544792      -0.013946408863548487
0.769997831259658       -0.012335666554772454
0.7819355762237501      -0.010817174586160884
0.7936523216662581      -0.009422886537661698
0.8051394629040913      -0.00816759835941887
0.81638592196081        -0.007043985478251118
0.8273808638247648      -0.0060433729467203505
0.8381139121786858      -0.005157740223667135
0.8485751165500343      -0.004379634004856855
0.858754946684461       -0.0037023953866889047
0.8686442411669043      -0.0031197033753532035
0.8782341736509689      -0.002625114874609564
0.8875162593876769      -0.002212106132419151
0.8964823605125316      -0.0018741213024133505
0.9051246320465252      -0.0016027033668078996
0.9134355050560761      -0.001385275023033334
0.9214078683501963      -0.0012102144602139063
0.929035043741256       -0.0010676262269881383
0.93631074157603        -9.492297303449203e-4
0.9432290287397316      -8.482399336553533e-4
0.9497843072225886      -7.592721512514551e-4
0.9559713191921552      -6.796774267124917e-4
0.9617851378810924      -6.094491185269413e-4
0.9672211322438047      -5.485093872717189e-4
0.9722749688842112      -4.965356418434268e-4
0.9769426167180463      -4.5300718538932966e-4
0.9812203512458078      -4.1725077797701216e-4
0.985104758383874       -3.884846192833354e-4
0.9885927378269728      -3.6586027693217925e-4
0.9916815059374967      -3.4850211289914906e-4
0.9943685981756192      -3.3554379130992085e-4
0.9966518710984307      -3.2616148556671574e-4
0.998529503966264       -3.1960344056450335e-4
```

Figure C.3: Airfoil coordinates upper and lower surface $\left(\frac{x}{c}, \frac{t}{c}\right)$ for airfoil f100-3mod - continued

```
f100-4mod uper side
0.9999992931110325     1.0164405948922806e-4
0.9985360834626775     3.8144012482461737e-4
0.9966675470010122     7.376340378546241e-4
0.9943950357044228     0.0011692319549949505
0.9917202079168008     0.0016750956881298224
0.9886450327759517     0.0022539724647041505
0.9851717932993149     0.0029045194974104773
0.9813030873351352     0.0036253190708910444
0.9770418256261534     0.004414879831271068
0.9723912263141363     0.005271620171261074
0.9673548053370866     0.006193830045683919
0.9619363623409163     0.00717960822855155
0.9561399619524927     0.008226772923819837
0.9499699105546925     0.00933274474914608
0.9434307290820569     0.010494402397022429
0.9365271228319416     0.011707912702125905
0.9292639498677583     0.012968538359661748
0.9216461902717179     0.01427042809134528
0.913678919258203      0.015606395583873625
0.9053672879343034     0.01696769497049414
0.8967165162117262     0.018343801936769488
0.8877319029271328     0.01972221066370278
0.8784188584853914     0.021088257741319928
0.8687832382954123     0.02242699821959964
0.8588366261624395     0.023762991191373175
0.8485876032242404     0.025098635082017675
0.8380439435711737     0.02642870822621408
0.8272171843286549     0.02777631450445848
0.8161191678811294     0.029166136552988175
0.8047571093213822     0.030584143166591905
0.7931399786904942     0.032028630738897945
0.7812770895051036     0.0334990035156396
0.7691779986043349     0.03499503799761136
0.7568525462497953     0.03651727102643013
0.7443109079954799     0.03806748054805743
0.7315636600626535     0.039649257823556834
0.718621765613406      0.0412679027184963
0.7054946423202799     0.04291504955164458
0.692191130518372      0.04457657340349035
0.678720654070517      0.046241753375018235
0.665092696812678      0.0478989726479331
0.6513163081627946     0.049531384642542114
0.6374006384601009     0.051120816591432375
0.6233560387082342     0.052657198986429704
0.6091935638281112     0.05413516717454417
0.5949247110429774     0.055552333231610455
0.5805609277796778     0.05690482119345825
0.5661136338177182     0.05818724942757875
0.5515942494595459     0.05939274581347872
0.5370143026929126     0.060513952755949445
0.5223856604844592     0.06154613920468266
0.5077203283710116     0.062485137017560234
0.49303039097361034    0.0633266586028273
0.47832800662645414    0.06406621056861564
0.46362540599878044    0.06469900899447029
0.4489349270209333     0.0652208435778896
```

```
f100-4mod lower side
6.686189777017703e-4    -0.0038732489013757537
0.002916067700975378    -0.007551011818769855
0.00658834113307048     -0.010508603620643814
0.01124579806859974     -0.012607473966232076
0.01652316855333412     -0.014127746983043787
0.022299018580917762    -0.015176736026001154
0.02851325173225946     -0.01577208775868466
0.035113649151216196    -0.01613171567704995
0.042081851462106565    -0.016350721709018287
0.049408499375696045    -0.01646138616577258
0.05708600531551087     -0.01648055629731301
0.06510735058841956     -0.016444114589403723
0.07346605157551317     -0.016381291320306295
0.08215567800758464     -0.01632911488354236
0.09116937143617564     -0.016307534556227642
0.10049985470569087     -0.016298400070623418
0.11013962058546461     -0.016264968342041435
0.12008094207967233     -0.01620520652241465
0.13031602985026655     -0.016145168213308282
0.1408368356968417      -0.0161077084787353
0.15163485231824161     -0.01614795900460927
0.16270024082359072     -0.01631826678228513
0.1740205667254208      -0.016690821970449573
0.1855839022838435      -0.017261596775198448
0.19738469835569947     -0.0179193531069301
0.20941531904945265     -0.018625683236424516
0.2216659502236021      -0.019382368638732
0.23412707048046605     -0.020183614369533927
0.24678929761810545     -0.021019615366554
0.25964371101788564     -0.021871927734813557
0.27268188134618376     -0.022712352124638912
0.2858944056849711      -0.02352393326424754
0.2992712643114585      -0.024295491988957727
0.31280172644608445     -0.02502473463409791
0.32647476622441995     -0.02571250153253822
0.34027947365605676     -0.026355186656036343
0.35420502514615776     -0.026944038477691216
0.36824051416836917     -0.027467366699300468
0.3823747876815034      -0.02791353232999411
0.3965964019018662      -0.028272120069228572
0.41089366395268806     -0.028532639411392124
0.42525461865539815     -0.0286848722232402
0.4396670251783864      -0.028726280466614348
0.4541185626768067      -0.028656958190034075
0.4685969008057582      -0.028477959347309147
0.4830897495983203      -0.028192162326266687
0.49758490647483483     -0.027803899026684755
0.512070265106982       -0.027317921459873367
0.5265337900299952      -0.026738423766069573
0.5409634990004439      -0.026068894405839108
0.555347503843638       -0.025313145111405498
0.569674089680907       -0.024476431862746704
0.5839317183483296      -0.023564973416097028
0.5981089258068976      -0.022584072186112303
0.612194332398236       -0.021538485112535404
0.6261765314810612      -0.02043108584022907
```

Figure C.4: Airfoil coordinates upper and lower surface $\left(\frac{x}{c}, \frac{t}{c}\right)$ for airfoil f100-4mod

```
f100-4mod uper side continued
0.4342690107728097      0.0656284681928556
0.4196401508282446      0.06591902057934121
0.4050609300967701      0.06609410293164689
0.3905438772322816      0.06615973168979744
0.3761013340670291      0.06612609476093076
0.36174535991826606     0.06600648656685064
0.3474877627719151      0.0658109476875325
0.3333401297567243      0.06554893964308199
0.31931384619836195     0.06522946767056982
0.3054201280012161      0.06486034039815762
0.29167004184382017     0.06444818164037279
0.27807450550401147     0.063998879735951
0.26464424629410643     0.06351894672331118
0.25139012411685197     0.06300683776153058
0.238322710903644       0.062465027890181865
0.22545289425531118     0.06188564350775202
0.21279179874657275     0.06125422911143337
0.2003493609341722      0.06057956018222373
0.18813780991960558     0.0598284948097786
0.17617157238382183     0.05894416808492789
0.16445999030025485     0.05795130479805592
0.1530107893397882      0.05688284887188692
0.14183165301751582     0.055762371158678506
0.1309331121392417      0.05458107226847339
0.12032822106864174     0.05330917861209821
0.11002670285820804     0.05194897033375519
0.10003798793021891     0.05050406222763133
0.09037459762464482     0.04895723998494999
0.081046853770008       0.047308599316734125
0.07206799780589801     0.045543376368185486
0.06344898206895737     0.043662783514260534
0.05520737849051413     0.04164135281205542
0.0473589644151896      0.03947064822197399
0.039934572911867555    0.03709950353700278
0.03296852299263254     0.03449250945480543
0.026527010110383893    0.03156291468360244
0.020668859988342354    0.02829457019322673
0.01547845689807908     0.02466027447055779
0.011003476452130007    0.02072739833029266
0.007256650663165811    0.01659668821538746
0.0042565778216761985   0.012362420803295212
0.002004786825056551    0.008124851923799225
5.843304327295582e-4    0.003956546825364609
0.000000000000000       0.000000000000000000
```

```
f100-4mod lower side continued
0.640044164576678       -0.019264107043987046
0.653786315392046       -0.018043620118561008
0.6673929611568171      -0.016783601938387998
0.6808546085437508      -0.015501034843513234
0.6941595958587984      -0.014188384589608749
0.7072969628976956      -0.012844348539553905
0.7202589360036753      -0.011497261962189148
0.7330371961884324      -0.010167571363417505
0.7456212430729223      -0.008853164218103605
0.7580013988768922      -0.0075582692276272255
0.7701735584822901      -0.006340195000768046
0.78213147318594        -0.005239318842480907
0.7938665736873505      -0.004277319949580641
0.8053686289045103      -0.0034595232591059554
0.8166265961649452      -0.002778401310624024
0.8276293385869062      -0.0022171798298899156
0.8383660807814065      -0.0017529015778910166
0.8488268037717669      -0.0013641306850499717
0.8590025744291386      -0.001044654861744389
0.8688846879523648      -7.850227251855267e-4
0.8784648479790055      -5.77985356377902e-4
0.8877350979219804      -4.1708016989516484e-4
0.8966877960371137      -2.958416248380076e-4
0.9053156143776304      -2.077424536598413e-4
0.9136115403601449      -1.4645869731558017e-4
0.9215688743686962      -1.0620347760378722e-4
0.9291812239701385      -8.199113222326816e-5
0.9364424974379073      -6.977540009011664e-5
0.9433468987848991      -6.645755581126673e-5
0.9498889252376325      -6.978953660041787e-5
0.9560633670554392      -7.820973649441771e-5
0.9618653091063927      -9.065062256686359e-5
0.9672901335454003      -1.0635178623933103e-4
0.9723335230711151      -1.247026792365915e-4
0.9769914643930486      -1.4512862334612687e-4
0.9812602516487501      -1.6702367270007073e-4
0.9851364895794007      -1.8972590033739808e-4
0.9886170963315487      -2.125254112021414e-4
0.9916993058207402      -2.3469299922590107e-4
0.9943806696641433      -2.555175387902382e-4
0.9966590587453796      -2.7434228842211893e-4
0.9985326644998671      -2.9059350097455645e-4
```

Figure C.4: Airfoil coordinates upper and lower surface $\left(\frac{x}{c}, \frac{t}{c}\right)$ for airfoil f100-4mod - continued

```
f100-5mod upper side
0.9999965143443549      2.055929350226943e-5
0.9985282461732526      2.7412566284540704e-4
0.9966534559160284      5.979034773918043e-4
0.9943736340313449      9.91628613215247e-4
0.9916905911493097      0.0014549692964585827
0.9886064558360617      0.0019875217609170793
0.9851236722038946      0.002588806526361557
0.9812449974764712      0.003258265920041125
0.9769734996282631      0.003995263519401146
0.9723125552244736      0.00479908623792079
0.96726584759167        0.0056689498047247195
0.9618373654493635      0.006604008396343466
0.9560314021275576      0.007603369157916593
0.9498525554843434      0.008666112293821032
0.9433057286211134      0.009791317311138005
0.9363961314736629      0.010978095871139473
0.9291292833412788      0.012225631570425407
0.9215110164142554      0.01353322688904211
0.9135474803910429      0.014900357600789869
0.9052451483665123      0.016326735283532935
0.8966108243624027      0.017812379403174095
0.8876517144440379      0.019358056911734308
0.8783747014156149      0.020961111434643912
0.8687862045228879      0.022614696266224404
0.8588926942043221      0.02431074520932748
0.8487006968495634      0.02603994157245488
0.8382170019638482      0.02779286593566081
0.8274488706416879      0.029561191895443557
0.8164024833334721      0.03132810435643355
0.8050854196263124      0.03308323626281412
0.7935060012776252      0.03481898854439083
0.7816727210485043      0.036526984769367284
0.7695941895099847      0.038197588191697954
0.757279452527476       0.03982208967158802
0.7447383837625473      0.041396033438959375
0.7319818269659893      0.042921346034478766
0.719021442013582       0.04440631064660193
0.7058695105681561      0.04586480531999095
0.692539016075578       0.04731737389297564
0.6790441970983979      0.04879590153739744
0.6653956783207401      0.05029818083429984
0.6516000117912405      0.05178346018693436
0.6376666170554526      0.053234989974835764
0.6236062002990406      0.054646213713579805
0.6094294036950664      0.05600828350869813
0.5951468019100506      0.057309628917407145
0.5807695407998531      0.058542726344429113
0.5663096837182423      0.05970939317074944
0.5517789880055957      0.060807057706909313
0.5371882964909899      0.061819267215647615
0.5225497798819275      0.062745419438677
0.5078753778350646      0.06358045038943391
0.4931771407480483      0.06431944613098904
0.4784672241475762      0.06495767965511183
0.46375788450008826     0.06549071978592853
0.4490614754686126      0.06591468944673083
```

```
f100-5mod lower side
5.806784546993617e-4     -0.0038889087568459973
0.0027488196304162045    -0.007604892201623986
0.00650254623565953      -0.010443039740468415
0.011290826614230294     -0.012209440273372073
0.016640641908290465     -0.013441220689459554
0.02243725186692616      -0.014350433560604408
0.028643048134971285     -0.014991750268610602
0.03523483957084992      -0.015416280246103782
0.04219833809209556      -0.015628267341377015
0.0495204221102776       -0.015693978481903927
0.05719218352990431      -0.015618296419130876
0.06520534199375577      -0.015412225515164846
0.07354965549466476      -0.015030397140093153
0.08222081763301252      -0.014562644128937544
0.0912180114674068       -0.014132754237941591
0.1005342536098997       -0.013752176167208524
0.11016178119110956      -0.013423541889737262
0.12009291503609842      -0.013161478331271684
0.13031946074334536      -0.012981248217766417
0.1408327934573463       -0.012915752560605332
0.15162321110538507      -0.012977441543230363
0.16268070936765838      -0.013164310937395568
0.17399547386956019      -0.01346524243565696
0.1855579516828397       -0.013866348188249193
0.19735732817017726      -0.014387675411258462
0.20938369185048777      -0.015020230233494282
0.22163015735710864      -0.015702963698214983
0.234087500077633        -0.01642428277952952
0.2467458354522912       -0.0171822672267987
0.2595965900088652       -0.017950881679272238
0.27263032038858775      -0.01871629411166276
0.2858377477927444       -0.019458441310398807
0.2992089117871643       -0.020164952107501924
0.31273317088915503      -0.02083240174333034
0.32639965614375965      -0.02145913471372757
0.3401974670000372       -0.022041428773322484
0.35411567822272244      -0.022572721285960287
0.36814328218647124      -0.023044076589949548
0.3822691209899585       -0.023444969510577725
0.39648181900130286      -0.023764450304560546
0.4107697360170813       -0.02399268428623312
0.42512101397739277      -0.024117228570150886
0.43952349532869306      -0.024131703683151196
0.45396488809292046      -0.02403751142584825
0.4684329119797246       -0.02383640075917486
0.48291532068744264      -0.023530847427549077
0.497399932890228        -0.023124270696707416
0.5118746532139997       -0.022620779328387245
0.526327475257454        -0.02202471337540925
0.5407464829888848       -0.021340471201057882
0.5551198706187319       -0.020572780755780073
0.5694359781182664       -0.01972710324076684
0.583683306931421        -0.018809570863333406
0.5978504690867311       -0.01782601315941751
0.6119255576677757       -0.016773588653680723
0.6258978363905633       -0.01566386310100335
```

Figure C.5: Airfoil coordinates upper and lower surface $\left(\frac{x}{c}, \frac{t}{c}\right)$ for airfoil f100-5mod

```
f100-5mod upper side continued
0.4343904352856829      0.06622656688035763
0.4197572583840175      0.06642421238503984
0.40517447097745984     0.06650816476885232
0.3906545374074936      0.06648716880755601
0.3762096568674877      0.06637499560630541
0.36185174280990123     0.0661837035369626
0.3475924987154425      0.06592257015109283
0.3334434466815149      0.06559973311896665
0.31941592773019706     0.06522311200699889
0.30552111626424666     0.06480012022048674
0.2917700398460756      0.06433730372824818
0.2781735333847928      0.0638418450853085
0.26474237643653736     0.06331792457011158
0.25148746007666634     0.06276319537766084
0.23841930065535652     0.06218120627119282
0.22554944691827875     0.06155070910058367
0.21288829459165498     0.060873943000561384
0.20044626051876432     0.06015022335372785
0.1882377451377542      0.05931691436082073
0.17627382632294386     0.05837211529438011
0.16456235952451953     0.05735178365843839
0.15311098508304724     0.056283078703258896
0.14192830178047025     0.05517694199345359
0.13103073991503705     0.05396797079098197
0.12042868220386946     0.052656153255396534
0.11013071077819499     0.051254732346571505
0.10014578393151866     0.04977076583829632
0.09048250393706433     0.04821151821514771
0.0811537415523022      0.04655822954239812
0.0721688362718032      0.0448147622346441
0.06353676815100287     0.04298663734664981
0.05527299782504712     0.04105042049241489
0.0473905636971214      0.039000065449196764
0.03991263733727579     0.03679785080597772
0.03288498102831041     0.0343578060102988
0.026378276915672755    0.03157291461681809
0.02047254216789749     0.028390079282158767
0.015247669317879084    0.024804283644618726
0.010774897412410854    0.020867558925034297
0.007055041594502977    0.01671244205092861
0.00414690960534268     0.01241365708580086
0.001967897553463259    0.008136396471122498
5.676078578621282e-4    0.003960068081521061
0.000000000000000       0.000000000000000000
```

```
f100-5mod lower side continued
0.6397576245506952      -0.014518630776633826
0.6535047448618208      -0.01347752898338683
0.6671375550707128      -0.012694985570075706
0.6806381822305462      -0.012112920118549262
0.6939908883100148      -0.011662075117245482
0.7071821307260714      -0.011279338857905618
0.7202003525464629      -0.01093557256382216
0.7330346644265853      -0.010613110971009322
0.7456744875352656      -0.010298061469346297
0.7581094729819717      -0.00997910474668069
0.770329537273474       -0.009649623840446892
0.782324813186718       -0.009305556978469838
0.7940856619167498      -0.008945254759722972
0.8056026904118577      -0.008569316040002226
0.8168667604783488      -0.008180143222782672
0.8278689918760341      -0.007781458850252865
0.8386007636000551      -0.007377949366999787
0.8490536902143901      -0.006974416762933534
0.8592195097892075      -0.0065728430443403926
0.8690901878312782      -0.0061750855151140585
0.8786579227413147      -0.005782876658270932
0.8879151505711493      -0.005397802882031235
0.8968545524187355      -0.005021350799067478
0.9054690598606701      -0.00465490727267475
0.9137518594645545      -0.004299741426679716
0.9216963970645917      -0.003956985328581311
0.9292963821747124      -0.0036276217279064783
0.9365457926787379      -0.003312481685580599
0.9434388797803837      -0.0030122516010492218
0.9499701731071803      -0.002727487418494085
0.956134485826022       -0.0024586331504438293
0.9619269196282937      -0.002206040910288065
0.9673428694655714      -0.0019699901206205843
0.9723780279514314      -0.0017507042598786256
0.9770283893821817      -0.0015483642670615827
0.9812902533628614      -0.0013631184190780472
0.9851602280506195      -0.0011950890394830888
0.9886352330437644      -0.001044376743754779
0.991712501951357       -9.110630677884333e-4
0.9943895846767759      -7.952122890021945e-4
0.9966643494413663      -6.968730809133989e-4
0.9985349845638525      -6.160803990499598e-4
```

Figure C.5: Airfoil coordinates upper and lower surface $\left(\frac{x}{c}, \frac{t}{c}\right)$ for airfoil f100-5mod - continued

```
f100-6mod upper side
0.9985248313636351     3.559347968852708e-4
0.9966412294235414     6.083460843428169e-4
0.9943506929943094     9.152921870817528e-4
0.9916550446601957     0.0012765306173394921
0.9885564293102155     0.0016917756711983584
0.9850573124193803     0.002160698564217937
0.9811604780797203     0.0026829276374953416
0.9768690267849526     0.0032580486511126737
0.9721863729726795     0.0038856051805511976
0.967116242327789      0.004565099128567253
0.9616626688502864     0.005295991360179063
0.9558299916901276     0.00607770246199958
0.9496228517508256     0.006909613619705255
0.9430461880627896     0.007791067599931006
0.9361052339267243     0.008721369816811896
0.9288055128272485     0.009699789460766462
0.9211528341175207     0.010725560670404428
0.9131532884775175     0.011797883740361722
0.9048132431520174     0.012915926381035654
0.8961393369794517     0.014078825082507728
0.8871384752003681     0.015285686469047939
0.8778178238707586     0.01653558731847102
0.8681848040401823     0.017827574398254973
0.8582470858904876     0.019160665535343867
0.8480125826909197     0.020533850819769984
0.8374894511939905     0.021946143254423598
0.8266857812234013     0.02339431361183265
0.8156097424562079     0.024874024040610794
0.8042697881872755     0.02638138437393162
0.7926745524270243     0.0279122219515742
0.7808327891365868     0.02946165301542281
0.7687533767599842     0.031024132930470794
0.756445378863588      0.03259393720787566
0.7439181052544589     0.03416567337768601
0.7311811099982771     0.03573432709161581
0.7182441230307023     0.03729477147898773
0.7051169889541178     0.03884129024601511
0.6918098335675016     0.04036902864916994
0.6783331060234494     0.04187449887030649
0.664697464231327      0.04335477081756453
0.650913548044061      0.04480543949560819
0.6369921554745355     0.04622226241338099
0.622944385496521      0.04760269476264652
0.6087814378413656     0.048944108124581456
0.5945145017226111     0.050242650734166554
0.5801548319352665     0.051494007455713975
0.5657138324751217     0.05269439773020746
0.5512027430428892     0.05383677211297116
0.5366331473596785     0.054917071902751136
0.5220166916449037     0.0559308328067708
0.5073647391038686     0.0568679423705416
0.4926889264997172     0.05772006907715534
0.4780012262333371     0.058482521213789496
0.4633137775220327     0.059152507235716995
0.4486387361644112     0.05972665616312044
0.4339882766546666     0.0602008304437059
```

```
f100-6mod lower side
3.03072091192433e-4      -0.0039427036213769105
0.0017366908691026845    -0.008025440730881805
0.004718868502814949     -0.011682698820964935
0.009033730208618309     -0.014415997352618462
0.014191330816733067     -0.01633242319507682
0.019940883798927195     -0.01757833370765089
0.026128170320963436     -0.018510344700728223
0.03271292520396428      -0.019238919748784014
0.03967587523311003      -0.019819635897433352
0.047005188700716946     -0.02028214844482664
0.05469074172334777      -0.020656733189199847
0.0627249255858132       -0.020944780424041198
0.07109958899764507      -0.021167171897855785
0.07980739907717496      -0.021323534536805418
0.08884068917263763      -0.02142693999785161
0.09819189714121049      -0.02148012033279367
0.10785328538906083      -0.02149357684743875
0.11781702354515444      -0.02147928260855724
0.12807517113786768      -0.021458065904318327
0.1386195824877715       -0.021468631172038486
0.14944154181011957      -0.021550564458506248
0.1605315052908711       -0.021735698081680317
0.17187893513972524      -0.02205473030245395
0.18347070220166414      -0.022569142504368846
0.19529350338334714      -0.02330207706773877
0.20734482335522816      -0.02410906068723947
0.2196217755806099       -0.024884969598517447
0.2321133699986022       -0.025646718218517977
0.24480961692474468      -0.02639351618723029
0.2577006498519868       -0.027119643733961737
0.2707759912545244       -0.027827140240408447
0.2840258430077017       -0.02850244905984027
0.2974399548302767       -0.02913628480358018
0.31100756370512006      -0.02972610539338506
0.324717786059555        -0.030268897325385787
0.3385597317098211       -0.030758007355318428
0.3525224196781879       -0.03118401811447141
0.36659467158973474      -0.031536753200906056
0.3807650644329611       -0.0318064489467838
0.39502192699013766      -0.03198418714763454
0.4093533448033915       -0.032064092649755314
0.42374723652627616      -0.03204328834190455
0.43819140140301194      -0.031916027507047466
0.45267372290972446      -0.03169169578604572
0.46718243654096947      -0.031389095187320255
0.48170591998577844      -0.031021775845661407
0.4962324379101758       -0.030593659752716707
0.5107501690346339       -0.030104787912677615
0.5252473471398669       -0.029556600327110442
0.539712347143163        -0.02895328824175101
0.5541336760060644       -0.028300512834844156
0.5684999578992395       -0.027604569263150223
0.582800014613699        -0.026873742024107136
0.597022943497565        -0.02611941257542664
0.6111578268471909       -0.025350458590024424
0.6251935267964881       -0.02456991704991269
```

Figure C.6: Airfoil coordinates upper and lower surface $\left(\frac{x}{c}, \frac{t}{c}\right)$ for airfoil f100-6mod

```
f100-6mod upper side continued
0.41937471168521506     0.06057420739201692
0.4048103457210041      0.06084615984413948
0.3903074668474641      0.061017266114179
0.375878319009299       0.061090323291086
0.36153503460995456     0.06107000725815144
0.3472895691334952      0.06096466854197358
0.33315362272764093     0.060785852460781234
0.3191386332804039      0.06054545164773587
0.3052558365090603      0.06025324993903533
0.2915162937425035      0.05991752178421536
0.27793104791697315     0.05954043151988911
0.2645111045397122      0.05912081173528225
0.25126705741749233     0.058666244119887447
0.23820931556779698     0.05818398117209003
0.22534800831941648     0.057683320844827024
0.21269318574548887     0.057170471327364275
0.20025532228071996     0.056637160337136665
0.1880446055423928      0.056078870103805495
0.17607149490014123     0.05548314042721558
0.16434621997390236     0.05484112196604286
0.1528788467759848      0.05414628785814405
0.14168042405345224     0.053376949142702176
0.13076315302220357     0.05250183483331584
0.12013960625295074     0.05149607250187019
0.10982203686581837     0.05034727049553413
0.09982257699056693     0.049049281010467495
0.09015249612809714     0.04760485917868456
0.08082265786695991     0.04601937407538288
0.07184278121183395     0.044303664610308276
0.06322129239126567     0.0424727465582192
0.054967103030732184    0.04053696062546799
0.04709670213156989     0.03847603832889549
0.039626262600887266    0.036279156157952124
0.0326040927120379      0.033847427582193834
0.026070984934768778    0.031145357494328507
0.0201229848209773      0.028056276589935192
0.014807763037986017    0.0246188456939621
0.010221722774785261    0.020823285315850305
0.006372437868685743    0.0167972764339351
0.0033312242673880985   0.012599403992612397
0.001272438797996338    0.008275757094105243
2.7204759393981474e-4   0.003994124096672676
0.0000000000000000      0.000000000000000000
```

```
f100-6mod lower side continued
0.6391187799870671      -0.023777080412750746
0.6529223758700496      -0.022970747576649703
0.6665934410742638      -0.02215387634026342
0.6801215174276366      -0.02133440596714222
0.6934962752392215      -0.02052023274809835
0.706707316766435       -0.019716012669089674
0.7197441080883977      -0.018922004678104717
0.7325962356929736      -0.018138161242676025
0.7452534376760133      -0.017364506335044612
0.7577055944759552      -0.016600852559753538
0.7699426674648175      -0.015845680019579363
0.7819548118463694      -0.015097867187364422
0.7937324127072225      -0.014357143528533975
0.8052660864844974      -0.013623966975936909
0.8165466801440131      -0.012899366266695784
0.8275652700062707      -0.012184786613850333
0.8383131596671276      -0.01148193319569286
0.8487818649079479      -0.010792429782583537
0.8589630519416848      -0.010116787473031554
0.8688487160140705      -0.009457012151958993
0.8784309598749841      -0.008813172378110794
0.8877021092030198      -0.008185062221309847
0.8966547973125525      -0.0075733639894530755
0.9052819831750505      -0.006979796933438355
0.913576935404231       -0.006406777371570108
0.9215332041613883      -0.005856932779383149
0.929144595017533       -0.005332666096190073
0.9364051523307984      -0.0048358601846383185
0.9433091544353177      -0.004367742477153792
0.9498511192374973      -0.003928888992620451
0.9560258168608696      -0.003519327293701886
0.9618282855481142      -0.003138692950126138
0.9672538476123673      -0.002786398504236041
0.972298123275158       -0.0024617837868548633
0.9769570413078436      -0.0021642285216903357
0.9812268462695262      -0.0018932199944880546
0.985104102730625       -0.0016483783600726829
0.9885856972046095      -0.001429448873109601
0.9916688386307488      -0.0012362736402973613
0.9943510582088193      -0.0010687556974494437
0.996630209227571       -9.268260329766116e-4
0.9985044672974919      -8.104205419431223e-4
0.999972331143331       -7.194697610637661e-4
```

Figure C.6: Airfoil coordinates upper and lower surface $\left(\frac{x}{c}, \frac{t}{c}\right)$ for airfoil f100-6mod - continued